# University of Southampton

Faculty of Engineering and Physical Sciences

Optoelectronics Research Centre

**Ultraviolet Generation in Silica Fibre and Microspheres**

by

**Yun Wang**

Thesis for the degree of Doctor of Philosophy

July 2019

# University of Southampton

# <u>ABSTRACT</u>

Faculty of Engineering and Physical Sciences

Optoelectronics Research Centre

<u>Thesis for the degree of Doctor of Philosophy</u>

**Ultraviolet Generation in Silica Fibre and Microspheres**

Yun Wang

Ultraviolet (UV) light sources have found numerous applications in medical science and engineering, such as disinfection, water purification, food production, UV curing and lithography, as short wavelengths have relatively high photon energy and provide high resolution. This thesis focuses on the UV light generation in silica glass. The UV spectral range is per se challenging both regarding material transparency and the availability of pump sources and optical devices. Two approaches are theoretically and experimentally demonstrated using submarine telecom silica fibres and Gd-doped silica and phosphosilicate fibres and microspheres.

The first approach relates to the sixth harmonic generation of deep UV from a 1550 nm laser source in a fully fiberised system by cascading second- and third- harmonic generation using a periodically poled silica fibre, and an optical sub-micron diameter optical fibre, respectively. Phase matching is achieved by harnessing intermodal phase matching in optical microfibres and a permanent $\chi^{(2)}$ induced via thermal poling. As a result, nonlinear processes can be observed despite the low third-order nonlinear susceptibility of silica glass.

The other approach presented in this thesis is based on the spectral properties of the rare earth ion $Gd^{3+}$, which has its first excited state located at a wavenumber of 32 000 $cm^{-1}$ above the ground level, corresponding to an UV emission at 312.5 nm. Relevant defects of the host material in the UV wavelength range are detrimental to lasing and are therefore investigated. Luminescence generated by the $^{6}P_{7/2} \rightarrow ^{8}S_{7/2}$ transition in the Gd-doped fibre is observed when pumped with various UV sources including a femtosecond laser, a UV LED and a lamp. A theoretical analysis of lasing is then carried out, including the estimation of the emission cross section and the related laser threshold and the selection of a suitable resonator, followed by experiment demonstration.

# Table of Contents

# Table of Tables

# Table of Figures

Table of Figures

Table of Figures

# Research Thesis: Declaration of Authorship

| Print name: | Yun Wang |
|---|---|

| Title of thesis: | Ultraviolet Generation in Silica Fibre and Microspheres |
|---|---|

I declare that this thesis and the work presented in it are my own and has been generated by me as the result of my own original research.

I confirm that:

1. This work was done wholly or mainly while in candidature for a research degree at this University;
2. Where any part of this thesis has previously been submitted for a degree or any other qualification at this University or any other institution, this has been clearly stated;
3. Where I have consulted the published work of others, this is always clearly attributed;
4. Where I have quoted from the work of others, the source is always given. With the exception of such quotations, this thesis is entirely my own work;
5. I have acknowledged all main sources of help;
6. Where the thesis is based on work done by myself jointly with others, I have made clear exactly what was done by others and what I have contributed myself;
7. Parts of this work have been published as:

   listed in Appendix A

| Signature: | | Date: | July 2019 |
|---|---|---|---|

# Acknowledgements

I would like to express my sincere thanks to my supervisor Prof Gilberto Brambilla for challenging my ability to finish the research. Without his kind assistance and endless effort, I could not have achieved this much. I am also grateful to my co-Supervisors, Prof Michalis N. Zervas and Dr Martynas Beresna for their valuable insights at different stages of my study.

I wish to express my gratitude to Prof Katia Gallo for her assistance on experiment conducted in KTH and for her valuable advice and encouragement.

My appreciation goes to M. Imran M. Abdul Khudus, Timothy Lee, Francesco De Lucia, Shahab Bakhtiari Gorajoobi, Pranabesh Barua, Vassili Savinov, Jun-Yu Ou and Jie Xu for their assistance on experiment and discussions around my research.

It is a great pleasure to thank everyone who has helped me and lent me equipment.

Thanks goes to Neil Sessions, Glenn Topley, Rob Standish and Trevor Austin for their technical support during my study.

I would like to acknowledge my sponsor, the Optoelectronics Research Centre at the University of Southampton, for sponsoring my study and providing me with financial stability.

Last but not least, my warm appreciation to my family for their endless love and for keeping me from sinking in research stress.

# Definitions and Abbreviations

## Abbreviations

| | |
|---|---|
| 4H | Fourth harmonic |
| 6H | Sixth harmonic |
| BBO | Beta barium borate |
| DUV | Deep ultraviolet |
| EDX | Energy-dispersive X-ray spectroscopy |
| FEM | Finite element method |
| FWHM | Full width at half maximum |
| GVM | Group velocity mismatch |
| IR | Infrared |
| LED | Light-emitting diode |
| MCVD | Modified chemical vapour deposition |
| MOPA | Master oscillator power amplifier |
| NA | Numerical aperture |
| NBOHC | Non-bridging oxygen hole centre |
| ODC | Oxygen deficient centre |
| OMF | Optical micro fibre |
| OPO | Optical parametric oscillator |
| PL | Photoluminescence |
| PLE | Photoluminescence excitation |
| PMD | Phase matching diameter |
| PPSF | Periodically poled silica fibre |
| SEM | Scanning electron microscope |
| SD | Standard deviation |
| SH | Second harmonic |
| SHG | Second harmonic generation |
| SMF | Single-mode fibre |
| SNR | Signal to noise ratio |
| SPM | Self-phase modulation |
| THG | Third harmonic generation |
| UV | Ultraviolet |
| WGM | Whispering gallery mode |
| XPM | Cross-phase modulation |

## Mathematical symbols

| | |
|---|---|
| $\mathbf{E}$ | Electric field vector |
| $\mathbf{H}$ | Magnetic field vector |
| $I$ | Optical intensity |
| $J_3$ | Modal overlap integral |
| $l$ | Laser cavity length |
| $n_{co}$ | Refractive index of fibre core |
| $n_{cl}$ | Refractive index of fibre cladding |
| $n_{eff}$ | Effective refractive index |
| $n^{(2)}$ | Nonlinear refractive index |
| $n_t$ | Total population density |
| $n_i$ | Population density of level i |
| $n_{i,th}$ | Population density in level i at laser threshold |
| $\Delta n$ | Refractive index contrast |
| $\mathbf{P_{NL}}$ | Nonlinear polarization vector |
| $R_{1,2}$ | Reflection at cavity ends |

# Definitions and Abbreviations

| | |
|---|---|
| $\boldsymbol{S}$ | Time-averaged Poynting vector |
| $V_p$ | Mode volume |
| $\alpha$ | Absorption coefficient |
| $\alpha_c,$ | Total cavity loss with the dimension of (length)$^{-1}$ |
| $\alpha_m$ | Internal loss due to material absorption at the laser wavelength |
| $\alpha_p'$ | Absorption coefficient in three-level laser |
| $\beta$ | Mode propagation constant |
| $\eta_p$ | Pump efficiency |
| $\eta_q$ | Quantum efficiency |
| $\eta_f$ | Pump efficiency in the frequency domain |
| $\eta_s$ | Pump efficiency in the spatial domain |
| $\eta_l$ | Pump efficiency determined by material loss |
| $\eta_{abs}$ | Efficiency of pump absorption by active ions |
| $\lambda$ | Wavelength |
| $v$ | Radiation frequency |
| $\sigma$ | Absorption cross section |
| $\sigma_a$ | Absorption cross sections at the laser wavelength |
| $\sigma_e$ | Emission cross sections at the laser wavelength |
| $\sigma_p$ | Absorption cross-section at the pump wavelength |
| $\tau_c$ | Cavity lifetime |
| $\tau_i$ | Decay lifetime of level i |
| $\emptyset$ | Photon flux |

# Chapter 1    Introduction

## 1.1    Motivation and aims

Ultraviolet (UV) light sources have found numerous applications in medical science and engineering [1–4], as short wavelengths have higher photon energy and provide higher resolution than visible light. UV-induced fluorescence is utilised to detect bacteria in water and toxic compounds produced by certain moulds that contaminate stored food, for example, aflatoxins on grains and nuts. The absorption of UV, particularly at 250–260 nm, by genetic nucleic acids is exploited for disinfection. The use of UV light instead of chemical substances for disinfection in water purification and food production avoids harmful by-products and is environmentally friendly. UV photochemical reactions are applied in light curing processes such as the high-resolution photolithography in microfabrication and the UV drying process in the printing industry. Replacement of infrared radiation and hot air with UV for drying minimises thermal distortion of the printed substrate. The invisible UV also benefits confidential communications.

At present, the generation of UV is mostly achieved with gas lasers [5] or diodes [1], or relies on nonlinear processes that enable frequency conversion from long wavelengths [6,7]. Cascaded frequency conversion into the deep UV at wavelengths below 300 nm generally exploits nonlinear crystals, such as beta barium borate (BBO), or a hybrid of bulk and fibre systems [8,9]. Broadband supercontinuum generation covering the UV has been reported using photonic crystal fibres through mechanisms such as self-phase modulation, soliton generation and four-wave mixing [10,11]. Despite these remarkable success so far, fiberised light sources could be an attractive alternative to conventional UV sources because of their excellent beam quality, extraordinary brightness, low detrimental thermal effects and high temporal stability.

Most optical fibres, notably silica fibres applied in this report, are robust and non-toxic, as distinct from conventional fragile UV lamps and dye lasers containing chemicals such as mercury vapour and solutions that are hazardous to human health and the environment, which therefore require careful handling and proper disposal. Although compact light emitting diodes (LEDs) compete actively with and are rapidly replacing light bulbs in both commercial and residential applications, UV LEDs have low efficiency, particularly at wavelengths below 315 nm with wall-plug efficiency of less than 5% [12,13], and are expensive, with wavelength- and power-dependent prices up to hundreds of British pounds, which is over a thousand-fold more expensive than their counterparts in the visible region. Meanwhile, although reduced cost and improved efficiency are expected with sophisticated manufacturing techniques in the future, a high-power output is generally achieved

with separate or on-chip LED arrays and therefore features large divergence angles, which is another drawback for applications demanding high beam quality and which makes fiberised sources an attractive alternative. Fiberisation can also avoid electric connections within working areas and hence ensure the safety of practical applications, for example, in an aquatic environment or with explosive chemicals. Besides, various spot sizes and radiation patterns can be achieved by, for instance, selecting specific optical modes inside fibres, tailoring numeric apertures at fibre ends or exploiting evanescent fields from lateral sides. Moreover, while the operating lifetime is a continuing concern with LEDs, the durability, high mechanical stability and low cost of silica fibres have been proved by the worldwide deployment of millions of kilometres of optical cables already in operation for more than 20 years. Optical fibre lasers have been widely applied in various research and industry areas, with explosive growth in terms of both performance and market share since 2000 [14,15].

Distinct from conventional lasers, especially bulky and energy-hungry UV gas lasers such as argon ion lasers comprising gas tubes and additional cooling systems, optical fibres have small diameters and long interaction lengths which, on the one hand, improves the interaction between light and gain media as well as the overlap between the pump and the signal light confined in the small core areas, leading to high energy efficiency compared with conventional lasers and facilitating nonlinear processes (e.g. harmonic generation), in terms of high-intensity-dependent efficiency and large nonlinear phase shift accumulated over long lengths. On the other hand, the high surface-area-to-volume ratios avoid excessive heating and hence the detrimental thermal effects, notably thermal lensing, which are critical issues in bulk crystals such as BBO [16]. Another advantage fiberised sources have over crystal-based lasers and harmonic generators is that they are alignment-free, without routine maintenance and adjustment of mirrors, lenses as well as focused light beams inside crystals, because the spatial coherence can be optimised by tailoring fibre refractive index profiles to select specific modes.

With the rapid development of accurate and sophisticated manufacturing techniques, optical fibres with different dopants and cross-sectional shapes have been developed for diverse applications. Meanwhile, various fiberised components such as fibre Bragg gratings, polarisation controllers, couplers and splitters have become available. These, together with the light-guiding property of optical fibres, not only facilitate the construction of complex systems but also minimise unnecessary UV light in free space, which is desirable considering its double-edged effects on human health.

The research in this report was conducted for a project that aims to demonstrate solid silica fibre-based UV light sources at wavelengths shorter than 350 nm with two approaches: (i) intermodal nonlinear processes (e.g. third harmonic generation) in an all-fiberised system and (ii) a new fibre

laser system using UV transparent fibres doped with rare earth ions and a two-photon pumping scheme with a visible/near-IR laser. The latter addresses manufacture of special silica fibres doped with the novel lasing element gadolinium (Gd), the design of fiberised laser pumps and their combination in suitable systems. Silica has various advantages, including its mechanical strength and high melting temperature, compatibility with existing silica-based components. As it is transparent in the UV down to $\lambda \sim 200$nm [17,18], ideally, defect-related issues are expected to be avoided by employing continuous-wave pump sources with low peak power.

The intermodal process exploited in this report refers to power conversion between pump fundamental mode and a harmonic higher-order mode in a single fibre, where the phase-matching condition is achieved by tailoring fibre diameter, without the necessity of additional components (e.g. nonlinear crystals) and free-space alignment. High conversion efficiency is possible by taking advantage of the high intensity of light well confined and controlled in fibres. In previous studies, researches have applied this technique for conversion from the near-infrared to the visible and the near UV [19,20]. In this report, the generation of deep UV is investigated.

Regarding the other approach, optical fibre lasers operating in the near-infrared and visible spectral regions have been achieved by taking advantage of the spectroscopic properties of rare-earth ions [21], such as $Yb^{3+}$, $Er^{3+}$, $Tm^{3+}$, $Nd^{3+}$ and $Sm^{3+}$ [22]. High-power $Yb^{3+}$-doped fibre lasers have found extensive applications in metal processing like welding, milling and marking [23,24]. Short wavelengths have been generated through upconversion processes, such as $LiYF_4$:Er operating at 551 nm [25], $Ho^{3+}$ fluorozirconate fibre laser emitting between 540 and 553 nm [26], $Pr^{3+}/Yb^{3+}$ co-doped ZBLAN fibre lasers tunable in the red, orange, green and blue wavelength ranges [27], and $LiYF_4$:Tm fluorescing near 350 nm and 450 nm with weak features at wavelengths down to 288 nm under avalanche pumping [28]. Extension to the UV would benefit applications such as precise micromachining and cutting of insulators, which are usually energy inefficient when carried out with near-IR lasers and would benefit from an improved optical absorption, relatively higher resolution as well as minimised thermal damage. Moreover, conventional lasers with high beam quality provide limited coverage with discrete lasing wavelengths in the UV, while dye lasers with a wide spectral bandwidth require additional modules for nonlinear harmonic generation of mid and deep UV. Far too little attention has been paid to the application of Gd in lasing since stimulated UV emission from Gd-doped glass was reported in the 1960s [29]. Trivalent gadolinium ions ($Gd^{3+}$) has its first excited state located at a wavenumber of 32 000 $cm^{-1}$ above the ground level, corresponding to an UV emission at 312.5 nm. Enhanced application flexibility is expected with this mid-UV emission from prevailing optical fibres. Furthermore, besides potential laser applications, the luminescence of Gd can be directly employed to, for example, remotely monitor X-ray dose which has been demonstrated using Gd-doped sol-gel silica glass in [30].

The research in this report, on the one hand, theoretically and experimentally demonstrates the all-fibre sixth-harmonic generation of deep UV based on previous researches on nonlinear processes in silica fibres. On the other hand, this research characterised the first Gd-doped silica fibres, which, by considering the work distribution and the time required by collaborators to design and set up a suitable pump source, is followed by manufacture of Gd-doped silica microspheres and setting up a low-power but straightforward pump source for UV micro-laser experiment. The term microsphere here refers to spherical optical micro-resonators, in which the mechanism of resonance can be traced back to the whispering-gallery waves discovered in St Paul's Cathedral, London, over a century ago. Whispering-gallery waves exploit total internal reflections, instead of a set of mirrors in a conventional FP resonator, to confine the optical field in a small volume, giving rise to localised high-intensity field with minimal reflection losses. This, together with potentially low unwanted losses such as material absorption and scattering of high-quality microcavities, leads to a long cavity phonon lifetime and reduced laser threshold power. A high quality factor of nearly 10 billion [31] and finesse higher than that obtained with conventional Fabry–Pérot cavities [32] have been reported using fused-silica microspheres. Laser threshold as low as 200 nW has been achieved with neodymium-doped silica microspheres [33]. Moreover, the resultant localised high-intensity optical field and evanescent tails outside make microspheres extremely sensitive sensors for particles, from bio-particles down to single molecules [34]. This study exploits microspheres as lasing cavities, not only for the low pump power requirement but also for the convenience of fabrication using existing doped fibre samples. The results pave the way towards applications based on the luminescence signal from Gd-doped optical fibres and construction as well as practical applications of silica-based UV sources with excellent beam quality and high power or high spatial localisation.

## 1.2      Report layout

This report includes sixth-harmonic generation of deep UV, characterisation of spectroscopic properties of trivalent gadolinium ions $Gd^{3+}$ doped in silica fibres and generation of mid-UV in microspheres fabricated from Gd-doped fibres.

As a range of techniques are explored, Chapter 2 provides a brief background of the present study, with emphasis given to the theory of harmonic generation in Chapter 3, for the theoretical work as well as mathematical modelling required.

Chapter 3 begins with a brief outline of phase-matching conditions in sub-micron diameter optical fibre, with emphasis on theoretical prediction of the microfibre diameter required. This is followed by microfibre fabrication and characterisations of the periodically poled silica fibre (PPSF) and the

pump laser source employed, before the sixth-harmonic generation of deep UV at λ = 258.5 nm from 1550 nm is experimentally demonstrated in this fully fiberised system. Finally, an investigation is carried out on possible explanations of the weak signal intensity compared with the theoretical expectation.

Chapters 4–7 focus on the generation of mid-UV at λ ≈ 314 nm based on Gd. The optical properties of Gd-doped in silica glass samples, especially in silica fibres, are investigated. Chapter 4 begins with an introduction to laser operation based on rare-earth elements and Gd-doped fibre samples fabricated by collaborators, followed by basic characterisations, including measurement of dopant concentrations and fibre propagation losses as well as $Gd^{3+}$-induced absorption. Then, in Chapter 5, luminescence from both $Gd^{3+}$ and the defects in the samples are recorded and analysed, together with a brief investigation on UV femtosecond laser-induced defects in silica host.

Based on the results reported in Chapters 4 and 5, Chapter 6 investigates the essential requirements for laser action and theoretically predicts lasing behaviour of Gd with emphasis on an estimation of the laser threshold power, according to which a pump source is set up based on second harmonic generation (SHG) in BBO crystal and the laser cavity design is discussed. Chapter 7 begins with an introduction to whispering gallery modes (WGMs). Microspheres are then fabricated from Gd-doped fibres, followed by a demonstration of the generation of UV light and observation of laser threshold.

Finally, the results achieved in this thesis is summarised in Chapter 8. Possible improvements in the experimental work together with an outlook for future work are discussed.

# Chapter 2    Background

This chapter introduces basic concepts, theories and models related to the present study, beginning with the properties of the optical modes in optical microfibres as well as the principles of harmonic generation. Emphasis is given to the theory of harmonic generation in Chapter 3 for the required mathematical modelling. Equations related to the mode profiles in microspheres are collectively presented. The pump source for harmonic generation is briefly described, followed by the introduction of sample characterisation techniques for measuring sample propagation losses, refractive live index profiles and dopant concentrations.

## 2.1    Optical mode property

### 2.1.1    Modes in microfibres

It is known that in a step-index fibre, where the refractive indexes of the core $n_{co}$ and the cladding $n_{cl}$ are uniform and satisfy the relation $n_{co} < n_{cl}$, light is confined and guided in the core via total internal reflection (a special case of Snell's Law) at the core-cladding interface. The transverse modes are discrete solutions of Maxwell's equation based on continuity at the interface [35–37]. The refractive index contrast $\Delta n = n_{cl}\text{-}n_{co}$ of standard single-mode fibres (SMFs) are usually minimal and of the order of $\Delta n \approx 10^{-3}$, hence weakly guiding approximation can be applied to solve the equations. However, this does not hold for the microfibres manufactured for the present study due to their large index contrast ($\Delta n > 1.4$).

### 2.1.1.1    Tapered fibre

The microfibres applied in the present study were fabricated by tapering single-mode fibres with 125µm in cladding diameter using a ceramic heater-based brushing technique [38,39]. Each optical microfibre (OMF) consists of a uniform waist region connected to the fibre pigtails via transition regions at both ends, as illustrated in Figure 2.1. In a down-taper transition region, with the decreased fibre diameter, the optical mode in the fibre core is pushed into the cladding.

The profile of the taper transition region determines the internal mode evolution. In an ideal adiabatic taper, the core mode in fibre pigtail evolves unperturbedly into the same mode in the cladding, which is desirable for the third harmonic generation (THG) in the following chapter, as the process requires the fundamental mode from the pump source to be maintained and transmitted into tapered fibre waist. The length-scale adiabaticity criterion is given by [40,41]:

$$\Omega \leq \frac{\rho(\beta_1 - \beta_2)}{2\pi}$$

(2.1)

where $\Omega$ is the tapering angle, as illustrated in Figure 2.1; $\rho$ and $\beta_i$ are the fibre radius and the mode propagation constants, respectively. Physically, the criterion stipulates that the local taper length-scale $z \approx \rho/\Omega$ (where approximation $\Omega \equiv \tan^{-1}(d\rho/dz) \ll 1$ is applied) should be larger than the beat length $z_b \equiv 2\pi/(\beta_1 - \beta_2)$ between these two modes to avoid core modes coupling to dominant higher-order cladding modes of the same symmetry, which otherwise occurs when the transition is sharp.
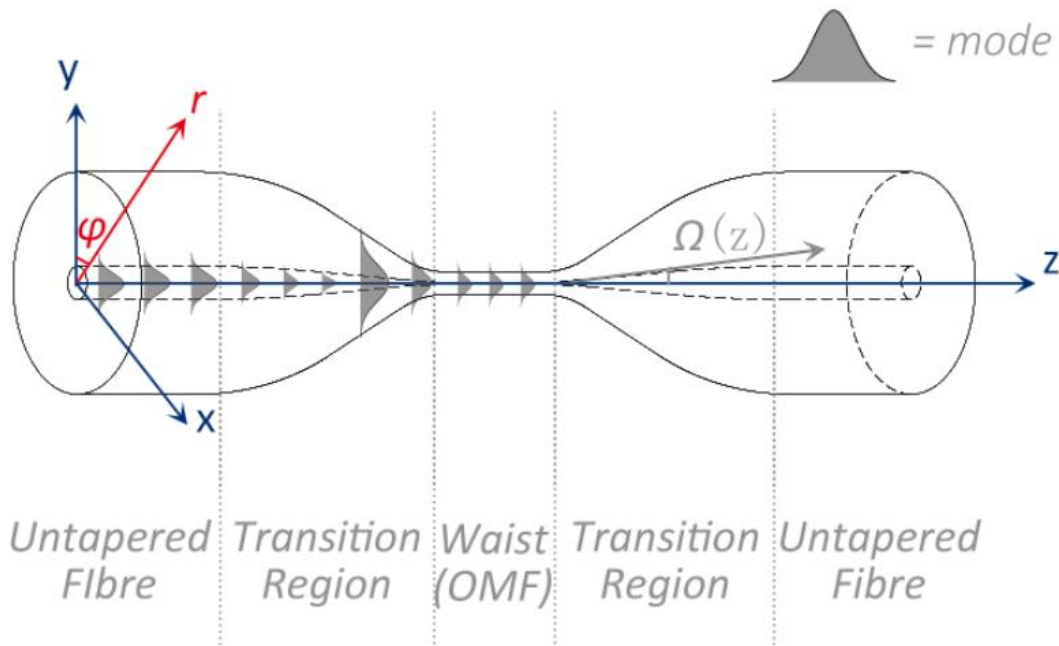


Figure 2.1 The profile of a tapered fibre with the mode evolution inside.

In the taper waist region, the original fibre core is negligible and light is guided by the interface between the fibre cladding and the outside environment, i.e. the silica-air interface of the OMF in the present study, with its evanescent field extending to the outside of the microfibre. The resultant large refractive index contrast leads to an enhanced and confined optical field that improves light-material interaction as well as the efficiency of nonlinear processes.

### 2.1.1.2 Eigenvalue equations and mode field distribution

In a longitudinally invariant fibre, the profile of a mode is maintained in the transverse plane with the phase oscillating in time and space. Therefore, the solutions to Maxwell's equations are sought in cylindrical coordinates in the form of:

$$\boldsymbol{E}(r, \varphi, z, t) = \boldsymbol{E}(r, \varphi)e^{i(\omega t - \beta z)}$$

(2.2a)

$$\boldsymbol{H}(r, \varphi, z, t) = \boldsymbol{H}(r, \varphi)e^{i(\omega t - \beta z)} \tag{2.2b}$$

where ω is the angular frequency, and β is the mode propagation constant. $\boldsymbol{E}$ and $\boldsymbol{H}$ are transverse electric and magnetic field distributions, respectively, and can be decomposed into $\hat{r}$, $\hat{\varphi}$ and $\hat{z}$ directions. Notably, the external charge density and current density are zero in step-index silica fibres, while the refractive index as well as the relative permittivity ($\varepsilon_r$) is uniform. Thus, combining Equation (2.2) with Maxwell's equations in cylindrical coordinates yields:

$$\left( \frac{\partial^2}{\partial r^2} + \frac{1}{r}\frac{\partial}{\partial r} + \frac{1}{r^2}\frac{\partial^2}{\partial \varphi^2} + k^2 n^2 - \beta^2 \right) \Psi(r, \varphi) = 0 \tag{2.3a}$$

where $\Psi(r, \varphi)$ denotes either electric or magnetic field component; k = 2π/λ is the wavenumber; and λ denotes the wavelength. Since the propagation constant (β) of guided modes always lies between $n_{co}k$ and $n_{cl}k$, normalised transverse wavenumbers U and W in the core and cladding, respectively, are then defined as:

$$\mathrm{U}^2 = (k^2 n_{co}^2 - \beta^2)a^2 \quad \text{(in the core)} \tag{2.4a}$$

$$\mathrm{W}^2 = \left(\beta^2 - k^2 n_{cl}^2\right)a^2 \quad \text{(in the cladding)} \tag{2.4b}$$

$$\mathrm{V}^2 = U^2 + W^2 \tag{2.4c}$$

where $a$ denotes fibre core radius, and V-parameter depends only on waveguide geometry. Due to the cylindrical symmetry of the fibre, the field oscillates as standing waves in the azimuthal ($\hat{\varphi}$) direction. Then, Equation (2.3) combined with Equation (2.4) can be solved as Bessel differential equations for the radial component $\Psi(r)$, leading to solutions in the form of linear combinations of Bessel functions. By considering the fact that the field oscillates in the core and evanesces in the cladding, physical solutions should take the form of Bessel functions of the first kind (J) when r < a and modified Bessel functions of the second kind (K) when r > a.

Taken together with the boundary condition, which addresses the continuity of tangential field components at the core-cladding interface, the eigenvalue equations for guided modes are given by [35]:

$$\left[ \frac{J_v'(U)}{UJ_v(U)} + \frac{K_v'(W)}{WK_v(W)} \right]\left[ \frac{J_v'(U)}{UJ_v(U)} + \frac{n_{cl}^2}{n_{co}^2}\frac{K_v'(W)}{WK_v(W)} \right] = \left( \frac{v\beta}{kn_{co}} \right)^2 \left( \frac{V}{UW} \right)^4 \quad \text{(Hybrid modes)} \tag{2.5a}$$

$$\frac{J_1(U)}{UJ_0(U)} + \frac{K_1(W)}{WK_0(W)} = 0 \quad \text{(TE\textsubscript{0m} modes)} \tag{2.5b}$$

$$\frac{n_{co}^2 J_1(U)}{UJ_0(U)} + \frac{n_{cl}^2 K_1(W)}{WK_0(W)} = 0 \quad \text{(TM\textsubscript{0m} modes)} \tag{2.5c}$$

Hybrid $HE_{vm}$ and $EH_{vm}$ modes are those with non-zero field vectors in all three ($\hat{r}$, $\hat{\varphi}$ and $\hat{z}$) directions, while modes with electric magnetic (or electric) vectors being perpendicular to the propagation direction are $TE_{0m}$ (or $TM_{0m}$) modes. The subscripts v and m denote mode orders in $\hat{\varphi}$ and $\hat{r}$ directions, respectively. The cut-off condition for single-mode operation is usually judged by the V-parameter. It can be found that the lowest order TE/TM mode is pushed out of the core with $\beta \rightarrow kn_{cl}$, which suggests $W \rightarrow 0$ and $V \rightarrow U$ in Equation (2.4). Taken together with Equation (2.5) when $J_0(U) = 0$, the critical V number can be found to be 2.405. Therefore, OMFs with $V < 2.405$ only support the fundamental $HE_{11}$ mode.

The electric field distribution of hybrid modes in $\hat{r}$, $\hat{\varphi}$ and $\hat{z}$ directions takes the form [35]:

$$E_r = \begin{cases} \dfrac{-a_1 J_{v-1}(UR) + a_2 J_{v+1}(UR)}{J_v(U)} f_v(\varphi) & r \leq a \\ -\dfrac{U}{W} \dfrac{-a_1 K_{v-1}(WR) - a_2 K_{v+1}(WR)}{K_v(W)} f_v(\varphi) & r > a \end{cases} \tag{2.6a}$$

$$E_\varphi = \begin{cases} \dfrac{-a_1 J_{v-1}(UR) - a_2 J_{v+1}(UR)}{J_v(U)} g_v(\varphi) & r \leq a \\ -\dfrac{U}{W} \dfrac{-a_1 K_{v-1}(WR) + a_2 K_{v+1}(WR)}{K_v(W)} g_v(\varphi) & r > a \end{cases} \tag{2.6b}$$

$$E_z = \begin{cases} -\dfrac{iU}{a\beta} \dfrac{J_v(UR)}{J_v(U)} f_v(\varphi) & r \leq a \\ -\dfrac{iU}{a\beta} \dfrac{K_v(WR)}{K_v(W)} f_v(\varphi) & r > a \end{cases} \tag{2.6c}$$

where

$$f_v(\varphi) = \begin{cases} cos(v\varphi) \\ sin(v\varphi) \end{cases}; \ g_v(\varphi) = \begin{cases} -sin(v\varphi) \\ cos(v\varphi) \end{cases} \quad \begin{matrix} even\ modes \\ odd\ modes \end{matrix} \tag{2.7a}$$

$$R = \frac{r}{a}; \ a_1 = \frac{F-1}{2}; \ a_2 = \frac{F+1}{2}; \ F = \left(\frac{V}{UW}\right)^2 \frac{v}{b_1 + b_2} \tag{2.7b}$$

$$b_1 = \frac{1}{2U}\left[\frac{J_{v-1}(U)}{J_v(U)} - \frac{J_{v+1}(U)}{J_v(U)}\right]; \ b_1 = -\frac{1}{2W}\left[\frac{K_{v-1}(W)}{K_v(W)} + \frac{K_{v+1}(W)}{K_v(W)}\right] \tag{2.7c}$$

Equations for TE and TM modes are not quoted here, as they will not be considered for the harmonic generation in this work, for lacking overlap with the pump $HE_{11}$ modes due to mode symmetry [19]. The integrated mode overlap for harmonic generation will be discussed in Section 2.2.

In addition, the modes can also be solved using the finite element method (FEM), which is suitable for solving partial differential equation under boundary conditions—especially for problems that cannot be solved using analytical methods. In FEM, a large system is divided into small finite elements. The discretisation approximates the partial differential equations with numerical models and algebraic equations, which are then assembled for modelling the entire system.

### 2.1.1.3    Mode profiles and confinement

Figure 2.2 and Figure 2.3 illustrate the fundamental mode profiles of the pump at λ=775 nm (for THG in Chapter 3) in OMFs of different diameters, and the power-weighted effective mode area $A_{eff}$ as a function of OMF diameter. $A_{eff}$ is defined as:

$$A_{eff} = \frac{\left| \iint_{-\infty}^{+\infty} S_z dA \right|^2}{\iint_{-\infty}^{+\infty} |S_z|^2 dA} \tag{2.8}$$

where $S_z$ is the z-component of the time-averaged Poynting vector given by:

$$\boldsymbol{S}_z = \frac{1}{2}(\boldsymbol{E} \times \boldsymbol{H}^*) \cdot \hat{z} \tag{2.9}$$
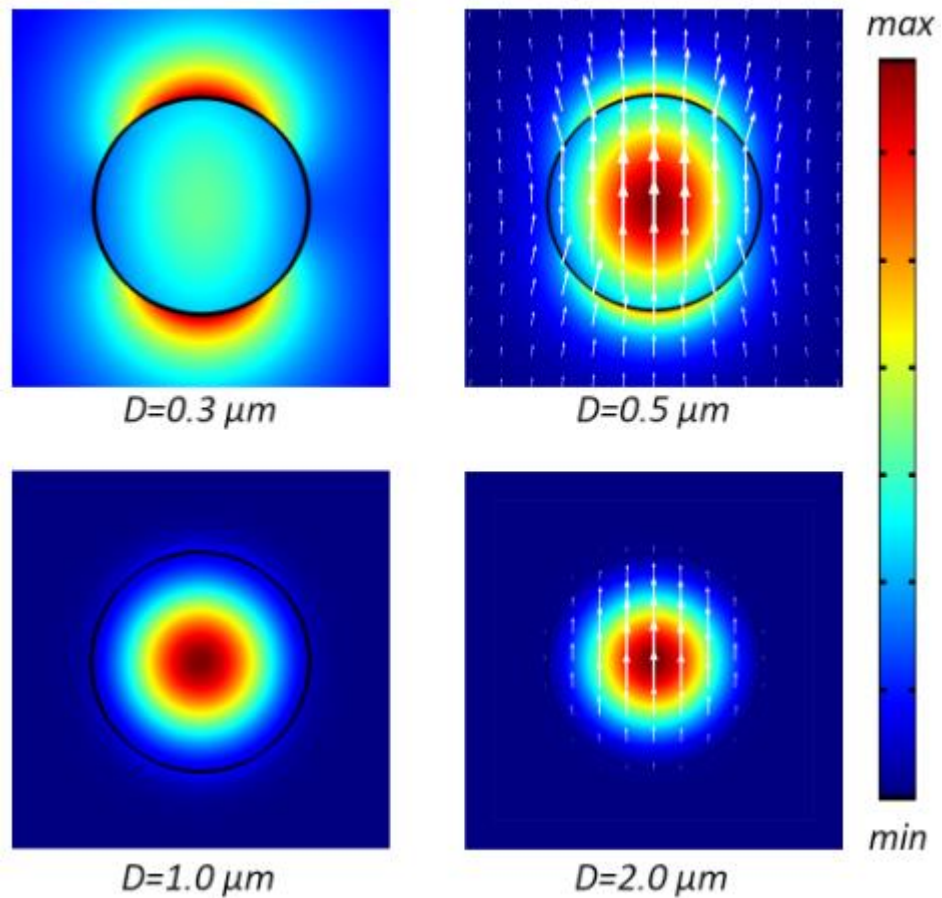


Figure 2.2 Transverse mode intensity $|\boldsymbol{E}|^2$ (background in colour) of the fundamental HE11 mode in microfibres of different diameters (D) in air, with λ = 775 nm, $n_{co}$ = 1.4538, and $n_{cl}$ = 1. The white arrows in the plots D = 0.5 μm and 2 μm denote electric field vector $\boldsymbol{E}(r, \varphi)$ and indicate quasi-linear polarised fields at small diameters.

At large diameters (e.g. D = 2 μm), the mode distribution with the most power confined in the core is similar to that of the fundamental mode in a standard single-mode fibre. As the diameter decreases, the field is pushed out of the core, similar to that in a taper transition region. The effective mode area reaches its minimum at D = 0.51 μm ~ λ/$n_{co}$, corresponding to the Abbe

diffraction limit with the highest confinement. At small diameters, following Gauss' Law, the large $\Delta n$ of OMFs results in evident discontinuity of electric field $E_r$ at the glass-air interface. On the other hand, the intensity at the interface increases, which benefits surface effects (e.g. SHG at the glass-air interface) but also enlarges the losses induced by surface roughness and possible contamination. Meanwhile, the evanescent field is enhanced, which facilitates sensing applications. Nevertheless, it is worth noting that since the evanescent field does not overlap with the nonlinear substance, power-weighted nonlinear refractive index $n^{(2)}$ should be exploited instead of the $n^{(2)}$ of silica for evaluating effective nonlinearity in harmonic generation. Moreover, the electric field vector plots suggest that the mode is not perfectly linearly polarised at small diameters but rather with the polarisation component perpendicular to the dominant one, which should be considered for analysing mode coupling in THG.
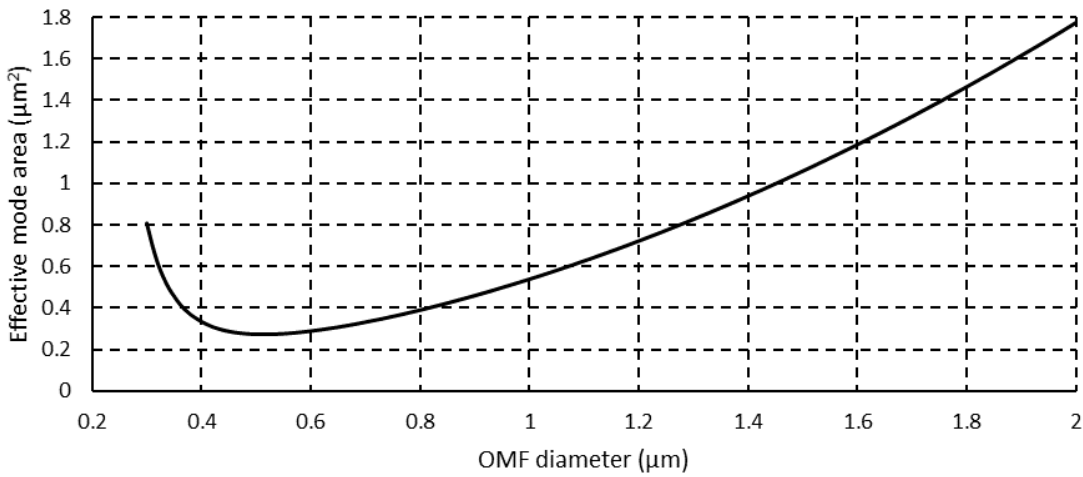


Figure 2.3 Power-averaged effective mode area $A_{eff}$ as a function of OMF diameter, with $\lambda = 775$ nm, $n_{co} = 1.4538$, and $n_{cl} = 1$.

### 2.1.2    Whispering gallery modes in microspheres

The theory of the well-known whispering gallery modes in microsphere resonators can be traced back over a century, when Lord Rayleigh discovered that a whisper uttered and heard at two opposite ends of the St. Paul's Cathedral actually crept along the wall, the concave surface of which limited the expanding of the acoustic beam cross-section and the decrease of intensity. Later, a similar phenomenon was found for electromagnetic waves in dielectric spheres [42], where waves circle inside the sphere and, at resonant frequencies, constructively interfere with themselves after one round-trip.

Figure 2.4 schematically presents the propagation of light confined in a sphere. The solution to the Helmholtz equation in spherical coordinates can be found in [42,43]. Similar to the fibres discussed in the previous section, and assuming constant polarisation in homogeneous spheres, the

approximation of the scalar wave equation leads to separated eigenfunctions in azimuthal ($\varphi$), polar ($\theta$) and radial (r) directions, i.e. $\psi_{lmn} \propto \psi_r \psi_\theta \psi_\varphi$, associated with three integer mode number $l$, $m$ and $q$, and the solutions fall into two cases, i.e. TE and TM subgroups. The characteristic equation, which links resonant frequencies to mode orders (l and q) as well as sphere parameters, i.e., refractive index and sphere radius R$_s$, is determined by the field continuity condition at the dielectric-air boundary and is given by [43]:

$$\left(\eta_s \alpha_s + \frac{l}{R_s}\right) j_l(k n_s R_s) = k n_s j_{l+1}(k n_s R_s) \tag{2.10a}$$

$$\eta_s = \begin{cases} 1 & TE\ modes \\ \dfrac{n_s^2}{n_0^2} & TM\ modes \end{cases} \tag{2.10b}$$

$$\alpha_s = \sqrt{\beta_l^2 - k^2 n_0^2}; \quad \beta_l = \frac{\sqrt{l(l+1)}}{R_s} \tag{2.10c}$$

where $j_l$ is spherical Bessel function of order $l$; $\beta_l$ indicates the propagation constant parallel to the surface of the sphere (illustrated in Figure 2.5); $\alpha_s$ indicates the decay constant away from the sphere in the radial direction; and n$_s$ and n$_0$ are the refractive indexes of the sphere and the surrounding medium, respectively. In the present study, n$_0$ = 1 for the surrounding air and the n$_s$ of silica is given by the Sellmeier equation in Section 2.2.2.
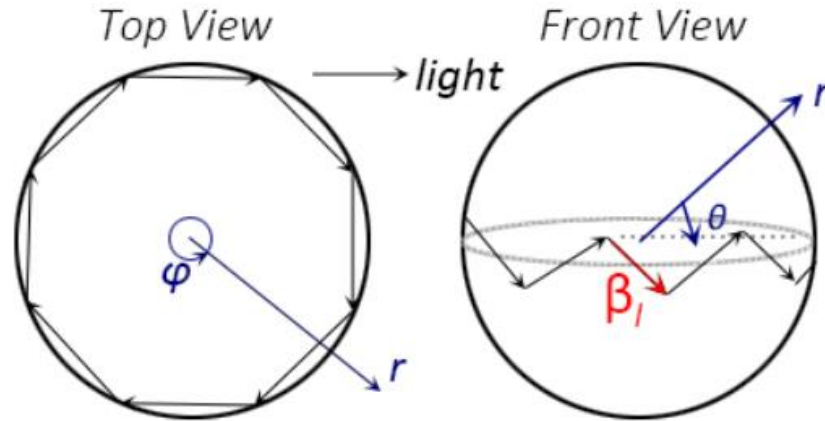


Figure 2.4 Schematic diagrams of light propagation inside a sphere via total internal reflection.

The mode field distribution takes the form [43]:

$$\psi_r = \begin{cases} j_l(k n_s r), & r \leq R_0 \\ j_l(k n_s R_s) e^{-\alpha_s(r-R_s)}, & r > R_0 \end{cases} \tag{2.11a}$$

$$\psi_\theta = e^{-\frac{m}{2}\theta^2} H_{l-m}(\sqrt{m}\theta), \quad m \gg 1 \gg \theta \tag{2.11b}$$

$$\psi_\varphi = e^{\pm im\varphi} \tag{2.11c}$$

which demonstrates that the field oscillates in the radial direction and is described by the Bessel function $j_l$, with an additional exponential decay term for the decay away from the sphere. In the azimuthal direction, it oscillates periodically as described by Euler's formula. In the polar direction, the associated Legendre polynomials for exact solutions are approximated to Hermite-Gauss functions $H_{l-m}$ in the case of large l and m orders with θ ≈ 0, corresponding to the modes confined around the equatorial plane of a sphere much larger than the wavelength. An example of these field distributions is plotted in Chapter 7.

Coupling light in and out of WGMs can be achieved through evanescently coupled tapered fibres [43,44], prisms [33], gratings [45] or deformed cavities [46,47]. The coupling efficiency depends on phase matching and overlap between WGMs and the external modes, for example, in waveguides or free-space. However, due to the issue of UV-induced photodarkening in silica fibres, free-space input coupling is briefly introduced and exploited in Chapter 7.

## 2.2    Third harmonic generation in silica

THG in tapered fibres was first demonstrated in 2003. With a 2.6-μm-diameter and 9-cm-long OMF tapered from a 9-μm-core-diameter SMF and pumped by a 30-fs-pulsed Cr:forsterite laser operating at 1.25 μm wavelength with an average output power of 450 mW. The THG efficiency was approximately 0.05% [48]. Later, instead of using a conventional scalar model for infinite plane waves in bulk material, a rigorous theory based on vector mode field for predicting THG behaviour in waveguides of high refractive index contrast—including the differential equations for power exchange and the overlap integrals between pump and harmonic modes—was proposed by Grubsky and Savchenko in 2005 [49]. Efficiency higher than 90% is achievable using a 5-cm-long microfibre of a diameter comparable to half of the fundamental wavelength. The theory was then experimentally proved via the THG of 355 nm in a sub-micro glass fibre pumped by a ns-pulsed laser in 2007 [50], with the conversion efficiency being limited by a short effective fibre length of 0.1 mm and being $2 \times 10^{-6}$ at a pump power of 250 W. A ~100x greater third harmonic signal (0.7 μW) in the UV was reported in a 3-cm-long sub-microfibre pumped by a 25-ps-pulsed laser, with an efficiency of $4.4 \times 10^{-6}$ which is possibly diminished by a walk-off issue, fabrication tolerance and material absorption [51]. In both cases, the authors also observed weak second harmonic (SH) signals, which were explained by surface nonlinearity at silica-air interfaces. In 2012, relatively high efficiency close to $10^{-3}$ was reported using a long OMF with a uniform taper waist length of 4.5cm, pumped by a 4-ns pulsed laser at a repetition rate of 100 kHz and pump peak power of 1.25kW [52]. The diminution of efficiency caused by fibre surface roughness at micro-scale diameters was then investigated in  [53], which will be discussed for the sixth harmonic generation of deep UV in the next chapter.

## 2.2.1    Third-order nonlinear susceptibility

In conventional linear optics, the effect of incident electromagnetic waves on the electron motion in media can be treated in a similar manner to the harmonic oscillation of a string under external and restoring forces. The parabolic potential well of an electron in the Lorentz model yields linear susceptibility $\chi^{(1)}$. Its dependence on the frequency of the external electromagnetic field gives rise to a frequency- and wavelength-dependent relative permittivity and refractive index, which further leads to phenomena such as chromatic dispersion and material absorption. However, this fails to explain nonlinear power-dependent phenomena such as four-wave mixing, sum-frequency generation and high-harmonic generation. The interpretation is then visualised by assuming nonlinear restoring force terms, which corresponds to a potential energy function illustrated in Figure 2.5 [54].
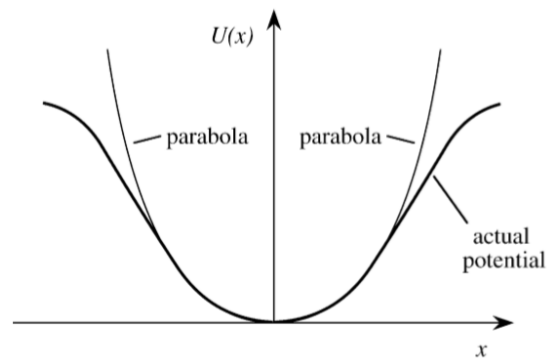


Figure 2.5 Potential energy function for a centrosymmetric medium with the lowest non-zero order of the nonlinear susceptibility being $\chi^{(3)}$ [54].

The resultant anharmonic oscillation model yields the third-order nonlinear susceptibility $\chi^{(3)}$, which induces a nonlinear polarisation $P_{NL}$ in media exposed to an external electromagnetic field [55]:

$$\boldsymbol{P}_{NL} = \chi^{(3)} \vdots \boldsymbol{EEE} \tag{2.12}$$

The product symbol '$\vdots$' is used because $\chi^{(3)}$ is a fourth-rank tensor. Note that media with inversion symmetry (e.g. silica) suggest $\boldsymbol{P}_{NL}(\boldsymbol{E}) = -\boldsymbol{P}_{NL}(-\boldsymbol{E})$, which calls for the second-order nonlinear susceptibility $\chi^{(2)}$ to be zero. Since lower order terms with higher coefficients tend to be dominant and higher-order terms are outside the scope of the present study, only $\chi^{(3)}$ is presented here. Nevertheless, in reality, the magnetic dipole and electric quadrupole in silica as well as the anisotropy structure near its surface result in minimal $\chi^{(2)}$ and contribute to second-order nonlinear phenomenon such as the SHG reported in the literature [51] and observed in Chapter 3.

A quasi-monochromatic field, with its polarisation maintained in a longitudinally invariant fibre, can be expressed as:

$$E(z,t) \sim \hat{x}\left[E(z)e^{-i\omega_1 t} + c.c.\right] \tag{2.13}$$

in which the field is $\hat{x}$ polarised. By treating $P_{NL}$ as a small perturbation, the application of this expression into Equation (2.12) leads to output at two frequency components, i.e. $\omega_1$ and $\omega_3 = 3\omega_1$, respectively. The generation of the latter is the so-called THG process illustrated in Figure 2.6 [54]:



Figure 2.6 The third harmonic generation process (left), with its energy-level description (right): three photons are absorbed to generate a new photon with triple frequency.

## 2.2.2 Chromatic dispersion and phase-matching conditions

The THG process is generally negligible in silica fibres due to phase mismatch caused by chromatic dispersion, a phenomenon in which the effective refractive index ($n_{eff}$) of a mode as well as its phase velocity varies with its frequency. Due to the resultant different propagation constant at the fundamental $\beta(\omega_1)$ and the harmonic $\beta(\omega_3)$ frequencies, the momentum is not conserved, $\Delta(n_{eff}k) \neq 0$, although the progress obeys the law of energy conservation ($3\omega_1 = \omega_3$). This prevents the power from growing with the propagation distance because the phases of the harmonic signals generated at different z positions are not inconsistent with each other, which results in destructive interference. Therefore, instead of continuously growing along z-direction, the power at $\omega_3$ component transfers back to the pump periodically.

Chromatic dispersion can originate from material dispersion and waveguide dispersion. The former is an intrinsic property of the medium and originates from the frequency-dependent response at the microscopic level, as described in Section 2.2.1, and is usually described by the Sellmeier equation. In the present study, the equation applied for silica within the spectral range of the present study is given by [56]:

$$n^2 - 1 = \frac{0.6961663\lambda^2}{\lambda^2 - 0.0684043^2} + \frac{0.4079426\lambda^2}{\lambda^2 - 0.1162414^2} + \frac{0.8974794\lambda^2}{\lambda^2 - 9.896161^2} \tag{2.14}$$

The waveguide dispersion is related to the effective refraction indexes of certain modes, which are governed by the refractive index profile of the waveguide, as the latter determines the mode field distributions and overlaps with the core and cladding materials of different refractive indexes.

Therefore, even at the same frequency, various modes possess different effective refractive indexes, which correspond to the discrete solutions to the eigenvalue equations in Section 2.1.1.2. The phase mismatching issue thus can be circumvented by tailoring the OMF diameter to meet $\Delta(n_{eff}k) = 0$, without altering the frequency or energy conservation. In the next chapter, this plays an important role for the THG in realising phase matching between the pump fundamental and the third-harmonic higher-order modes.

Higher-order modes of third harmonic rather than the fundamental one are considered for power coupling from the pump fundamental mode. This is because, within the spectral range of the present study, the refractive index of silica increases as the wavelength decreases; meanwhile, the short-wavelength harmonics tend to be more confined in the high-index silica than the fundamental, leading to larger $n_{eff}$ for the former than the latter. Therefore, in OMFs with high confinement factors, despite the large overlap between them for potential efficient power coupling, the fundamental mode of the harmonic's $n_{eff}$ is always higher than that of the pump, thereby suggesting that the phase-matching condition cannot be satisfied by tuning OMF diameters. Nevertheless, with the OMF diameter approaching the cut-off diameter of a third-harmonic higher-order mode, as the fraction of power in its evanescent field in air increases, the mode effective refractive index decreases rapidly ($n_{eff} \rightarrow 1$) and cuts off before the pump mode. Yet, at large OMF diameters, where the mode is well confined in the silica core, the material dispersion is dominant and the $n_{eff}$ of the third-harmonic higher-order mode is larger than that of the pump. Therefore, between these two extremes, at a certain OMF diameter, it is phase-matched with pump fundamental mode. This intermodal phase-matching technique has been applied in four-wave mixing [57], second harmonic generation [58] and broadband THG [19]. The phase-matching diameter (PMD) can be found by plotting $n_{eff}$ as a function of OMF diameter for various modes using the modal eigenvalue Equations (2.5) or FEM method. The results for specific cases in the UV and air-clad silica OMFs are illustrated in the next chapter.

### 2.2.3    Conversion efficiency

Besides the phase relationship, THG conversion efficiency is also influenced by the field distributions of the pump and the harmonic modes. The coupled mode differential equations derived by Grubsky and Savchenko based on the Lorentz reciprocity theorem with additional loss terms are given by [49]:

$$\frac{\partial A_1}{\partial z} = -\alpha_1 A_1 + in^{(2)}k_1\left[(J_1|A_1|^2 + 2J_2|A_3|^2)A_1 + J_3 A_1^{*2}A_3 e^{i\delta\beta z}\right] \qquad (2.15a)$$

$$\frac{\partial A_3}{\partial z} = -\alpha_3 A_3 + in^{(2)}k_1\left[(6J_2|A_1|^2 + 3J_5|A_3|^2)A_3 + J_3^* A_1^3 e^{-i\delta\beta z}\right] \qquad (2.15b)$$

where $A_i$ is the complex field amplitude; the subscripts 1 and 3 denote the pump and harmonic modes, respectively; $\alpha_i$ is the loss coefficient, which is included for the UV absorption in silica, and therefore $\alpha_1$ is set to zero in this study; $n^{(2)}$ is the nonlinear refractive index of silica; $\delta\beta = \beta(\omega_3) - 3\beta(\omega_1)$ is the detuning, i.e. propagation constant mismatch between the pump and the harmonic waves. The nonlinear overlaps $J_i$ integrated over the nonlinear silica core are given by:

$$J_1 = \frac{1}{3} \iint_{core} \left( 2|\boldsymbol{E}_1|^4 + \left|\boldsymbol{E}_1^2\right|^2 \right) dS \tag{2.16a}$$

$$J_2 = \frac{1}{3} \iint_{core} (|\boldsymbol{E}_1|^2|\boldsymbol{E}_3|^2 + |\boldsymbol{E}_1 \cdot \boldsymbol{E}_3|^2 + |\boldsymbol{E}_1 \cdot \boldsymbol{E}_3^*|^2) dS \tag{2.16b}$$

$$J_3 = \iint_{core} ((\boldsymbol{E}_1^* \cdot \boldsymbol{E}_3)(\boldsymbol{E}_1^* \cdot \boldsymbol{E}_1^*)) dS \tag{2.16c}$$

$$J_5 = \frac{1}{3} \iint_{core} \left( 2|\boldsymbol{E}_3|^4 + \left|\boldsymbol{E}_3^2\right|^2 \right) dS \tag{2.16d}$$

The unit of $J_i$ is $m^{-2}$. $J_1$ and $J_5$ are related to self-phase modulation (SPM) at the pump and harmonic wavelengths, respectively, while $J_2$ governs the cross-phase modulation (XPM) between them. SPM and XPM involve a phase shift caused by the intensity of the mode itself and the other mode, respectively. The resultant additional phase shift leads to phase mismatch, reduced conversion efficiency as well as frequent power exchange between the pump and the harmonic waves. In order to find the maximum conversion efficiency in simulation, this shift can be compensated by adjusting the detuning term, the optimal value of which is thus given by [49]:

$$\delta\beta_{opt} \approx -\frac{3}{2}(J_5 - J_1)k_1 n^{(2)} P_0 \tag{2.17}$$

where $P_0$ is the initial pump power.

In the experiment, OMF diameter is indirectly controlled by monitoring the output signal at the third harmonic wavelength; therefore, in theory, this issue related to SPM and XPM is presented as a difference between the experimental and simulated PMDs, which thus can be compensated by fine-tuning the OMF diameter or the pump wavelength. In reality, the efficiency and measured OMF diameters in this study are also affected by OMF surface roughness and the thermal-optic effect of silica, which will be discussed in the next chapter.

$J_3$ is the overlap between the pump and the harmonic modes and determines the power exchange efficiency. Mode field distributions at the studied wavelengths will be presented in the next chapter for a visualised interpretation. It is expectable that harmonic modes with fields similar to the pump fundamental field lead to high $J_3$ overlaps and thus high conversion efficiency. By considering the modal field of the pump with its azimuthal mode order $v = 1$, only hybrid modes with $v = 1$ or $3$ that have non-zero $J_3$ overlapped with the pump were analysed for the harmonic generation; TE, TM and other hybrid harmonic modes are not considered here due to modal field symmetry [19].

Notably, as $A_1$ decreases and $A_3$ increases, pump power depletion accompanied with losses modifies the effects of XPM and SPM as well as the detuning term, thus slowly alters the conversion rate and power flow direction along the OMF, though not as frequently as the situation where OMF diameter deviates far from the PMD. Therefore, the conversion efficiency reaches its maximum after a certain distance before the direction of power flow alters, which determines the optimum length of the OMFs required to be fabricated. Equations (2.15) and (2.16) are applicable to quasi-continuous-wave pump sources and justified for pulses longer than ~1 ns. The use of a quasi-continuous-wave source in this study minimises the impacts of walk-off and spectral broadening issues, which otherwise require introducing addition terms.

## 2.3 Second harmonic generation in periodically poled silica fibres

Second harmonic generation, which is also called frequency doubling, as illustrated in Figure 2.7 [54], is a nonlinear optical process in which two photons at the same frequency ($\omega_1$) interact with material with non-negligible second-order susceptibility $\chi^{(2)}$, leading to the generation of a new photon at twice the frequency of the initial photons, i.e. $\omega_2 = 2\omega_1$.
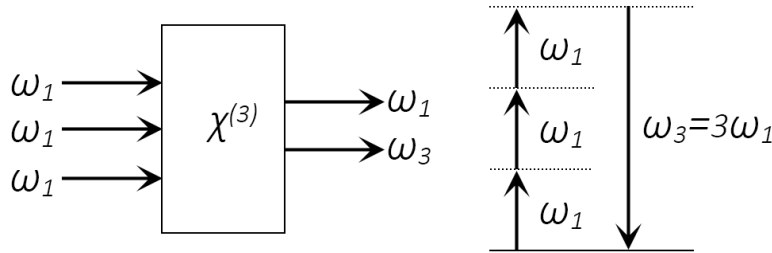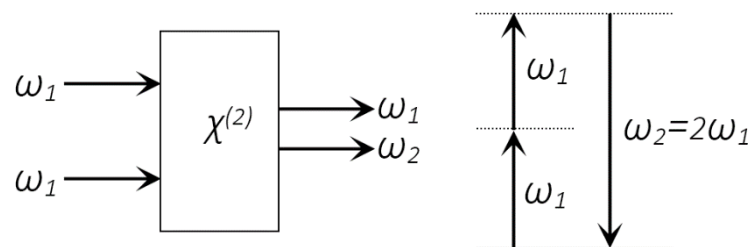


Figure 2.7 Second harmonic generation process (left) with its energy-level description (right): two photons are absorbed to generate a new one with double frequency [54].

### 2.3.1 Second-order susceptibility in silica

Although SHG in crystals have been proved efficient, they have drawbacks that can be resolved by employing silica fibres. For example, the periodically poled lithium niobate does not withstand very high power (e.g. ns-pulse with energy density of 2 J/cm$^2$ [59]) that can instead be endured by pure silica for nanosecond pulse laser at $\lambda$~1μm (e.g. 16 J/cm$^2$ [60]). BBO with a bandgap (~6.6 eV) smaller than that of silica (~9 eV) is less transparent in the UV and is thus more likely to face two-photon-absorption-induced thermal issues which must be handled carefully [16]. Moreover, the free-space coupling is sensitive to mechanical disturbance and requires regular re-alignment.

A permanent $\chi^{(2)}$ ~1 pm/V in bulk fused silica was first demonstrated via a thermal (250 °C~325 °C) and electric field (E ~ 5x10$^4$ V/cm) poling process, where a heated glass immersed in electric field experienced a redistribution of the impurity charge carriers, resulting in the formation of a space-

charge region located near the anode. After cooling the glass in the presence of the electric field, a permanent $\chi^{(2)} \sim 3\chi^{(3)}E_{rec}$ was created as a consequence of a third-order nonlinear optical rectification process, where $E_{rec}$ refers to the recorded electric field permanently frozen inside the space-charge region of the poled glass [61]. Since then, various configurations have been used to apply electric field in silica fibre samples; for example, electrodes applied on the flat face of a D-shaped fibre [62] and high anodic potential connected to wires set longitudinally inside holes in fibres exposed to ArF excimer lasers [63] or molten metal filled into twin-hole structures [64]. The PPSF (fabricated by Francesco De Lucia at the ORC) used in the present study exploits a twin-hole fused silica Ge-doped core optical fibre. Liquid electrodes were used for facile removal, low loss and enhanced sample length [65]. In order to fulfil the phase velocity matching condition between the pump and the second harmonic, the thermal poling process was followed by a periodic erasure of the frozen-in electric field using UV light to achieve quasi-phase matching (QPM) [66,67]. With this method, the highest effective $\chi^{(2)}$ reported in PPSF is 0.12pm/V [65]. Although this is not comparable to the magnitude achieved in bulk silica samples, it can be improved by employing long fibre length. A 26.3-cm-long device with internal efficiency up to 45% and multi-watt output at second harmonic frequency has been reported in [68].

### 2.3.2　　　Second harmonic generation and quasi-phase matching

$\chi^{(2)}$ is a third-rank tensor containing 27 components. However, by exploiting its symmetry, neglecting zero or minimal elements, and carefully selecting the directions of propagation and polarisation of the mode, $\chi^{(2)}$ can be treated as a scalar ($d_{eff}$). In this study using an x-polarised E field, the $\mathbf{P}_{NL}$ of the second harmonic wave can be given by [54]:

$$\boldsymbol{P}_{NL}(\omega_2) = \varepsilon_0 \chi^{(2)} \boldsymbol{E}_1^2 = 2\varepsilon_0 d_{eff} \boldsymbol{E}_1^2 \tag{2.18}$$

where the subscripts 1 and 2 indicate the pump and the second harmonic, respectively. By substituting the electric field expression and Equation (2.18) into the well-known nonlinear wave equation, the evolution of the amplitude of the second harmonic wave is given by:

$$\frac{dA_2}{dz} = \frac{i\omega_2^2 d_{eff}}{c^2 \beta_2} A_1^2 e^{i\Delta\beta z} \tag{2.19}$$

where $A_i$ and $\beta_i$, again, are the amplitude and propagation constant of the pump (i = 1) or the second harmonic (i = 2) wave, respectively; $\Delta\beta = 2\beta_1 - \beta_2$ is the phase mismatch, i.e. the momentum mismatch between the fundamental and the second harmonic modes corresponding to the $\delta\beta$ in THG. In the undepleted pump approximation and slowly varying envelope approximation, where the amplitude of the $E_i(z) \sim A_i^2 e^{ik_i z}$ in Equation (2.13) is assumed to be slowly varying or constant with low conversion efficiency, by integrating Equation (2.19) along z

direction and according to the relationship between intensity and field amplitude, the intensity of the second harmonic I₂(L) after propagation length L takes the following form:

$$I_2(L) \propto A_2^2 = \left(\frac{\omega_2^2 d_{eff} A_1^2}{c^2 \beta_2}\right)^2 L^2 \operatorname{sinc}^2\left(\frac{\Delta\beta L}{2}\right) \tag{2.20}$$

It is evident that the second harmonic intensity is proportional to the square of the input intensity. Nevertheless, the $L^2 \operatorname{sinc}^2(\Delta\beta L/2)$ portion implies that power flows back and forth between the pump and the harmonic at a period twice the coherence length $L_c$, which is defined as: $L_c = \pi/\Delta\beta$. Similar to the THG, high conversion efficiency is suppressed by phase mismatch issue ($\Delta\beta \neq 0$), due to the chromatic dispersion property of the media. To allow the second harmonic to grow with propagation distance, in crystals QPM is generally achieved by periodically flipping the material as well as the polarisation orientation [69], leading to a multilayer structure with the modulation of the polarisation along the propagation direction in the order of '↑↓↑↓↑↓', as illustrated in Figure 2.8.

Since χ⁽²⁾ is induced via thermal/electric field poling process in silica fibres, instead of flipping the material or fabricating OMFs at high temperature afterwards which would cause depoling, the frozen-in electric field is periodically erased to circumvent destructive interference, which results in the polarisation modulation in the order of '↑-↑-↑-', where '-' denotes the null section that does not contribute to SHG due to the lack of χ⁽²⁾. This null section allows periodic rephrasing without power exchange between the pump and the harmonic. The evolution of the amplitude of the second harmonic A₂ along propagation direction is illustrated in Figure 2.8 for comparison.
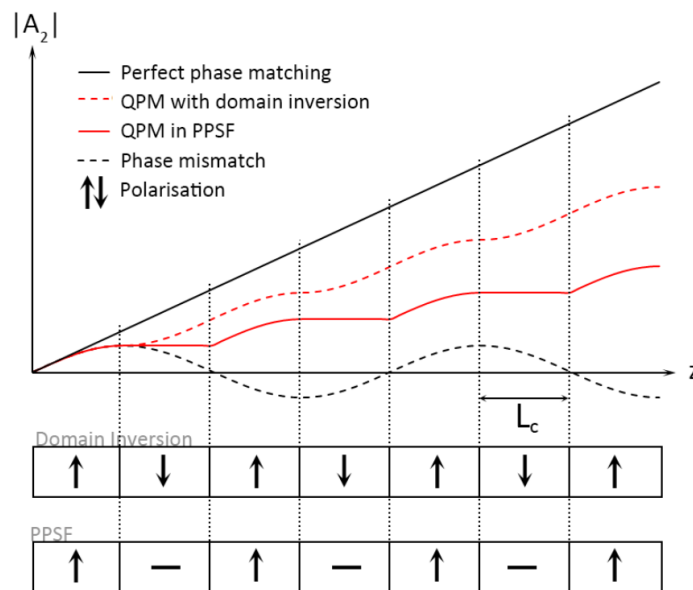


Figure 2.8 Schematic diagrams of QPM techniques with SH amplitude plotted as a function of propagation distance, compared with non-phase-matched and perfect-phase-matching cases (plotted according to [54,70]).

Distinct from the solution to the phase mismatch in THG, neither of the two QPM methods achieves $\Delta\beta = 0$. The second harmonic waves generated at different z positions within each period are still not perfectly in phase. Therefore, the slopes of the curves vary along the waveguide with the conversion being less efficient than the case of perfect phase matching in which the second harmonic amplitude grows linearly. Since $\chi^{(2)}$ is periodically erased in PPSFs, half of each $2L_c$-long section does not contribute to SHG, which makes it less efficient than the conventional QPM technique with domain inversion employed in crystals. Despite this, high efficiency is achievable in fibres with long lengths, as reviewed in Section 2.3.1.

## 2.4    Master oscillator power amplifier

A narrow-linewidth pump with high peak power is a decisive factor in harmonic generation processes to achieve high conversion efficiency. Nanosecond pulses for harmonic generation in this study were generated from a fibre master oscillator power amplifier (MOPA) system. A schematic diagram of the experimental setup is illustrated in Figure 2.9.
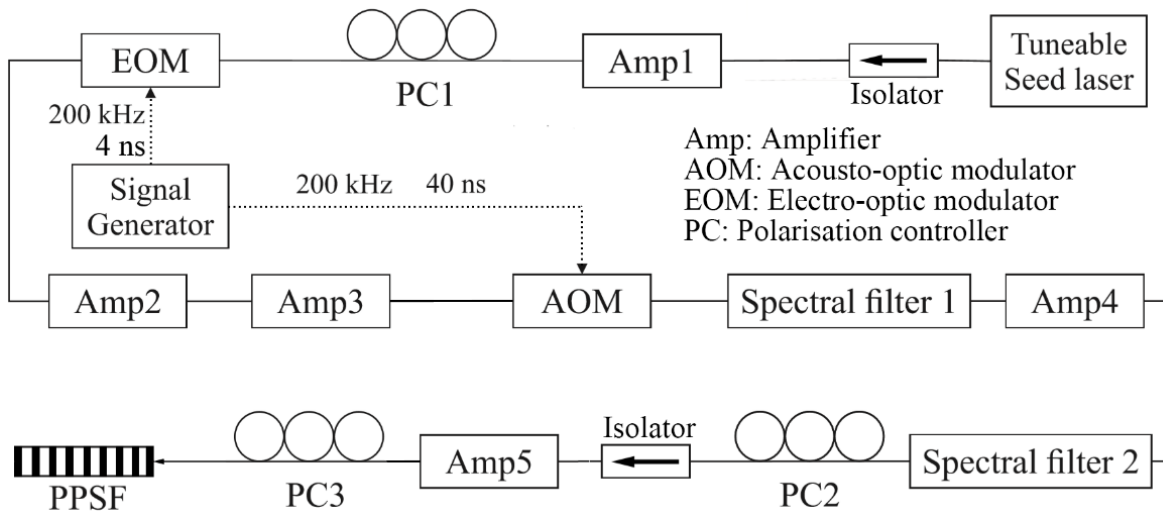


Figure 2.9 A schematic diagram of the fibre MOPA system (adapted from [20]), which is employed as the pump of the harmonic generation in Chapter 3.

The system was seeded by a narrowband tuneable continuous-wave laser source (Photonetics Tunics BT) with its output set to 3mW, in the present study, and its wavelength adjusted to the central wavelength of the PPSF employed. The current of the first erbium-doped fibre amplifier, Amp1, was set to obtain an output of approximately 30mW. This was then decreased to ~21uW after an electro-optic modulator (EOM) that generated 4-ns-pulses at a repetition rate of 200 kHz. The low output was due to the mechanism of EOM, which scattered out inter-pulse energy, and its insertion loss higher than 3dB. Since the response of EOM depends on polarisation, a polarisation controller was set beforehand to maximise the output. This was followed by the use of two

amplifiers to increase average power to ~150mW, and an acousto-optic modulator (AOM) that was synchronised to the EOM via the signal generator with a delay set to compensate the propagation delay between two modulators. The AOM and two spectral filters were set in between amplifiers to remove undesired background in both time and frequency domains by filtering out inter-pulse and out-of-band components induced by factors such as amplified spontaneous emission from the amplifiers. Before the last amplifier, which generated an output of ~300mW, an isolator was set to protect devices in the previous stages from being damaged or disturbed by undesired feedback.

## 2.5 Characterisation techniques

In the present study, the Gd-doped fibres were characterised in terms of refractive index profiles, dopant concentrations and fibre propagation loss. This section briefly explains the mechanism behind these measurement methods, with several details that were carefully handled in the loss and concentration measurement to minimise measurement errors.

### 2.5.1 Propagation loss

The fibre propagation loss was characterised using the so-called cut-back method [71], which requires the measurement of output power from fibres of different lengths. According to the Beer-Lambert law, the output power P(L) after a propagation distance of L is related to the input power P(0) via:

$$\mathrm{P(L)} = P(0)e^{-\alpha_f L} \tag{2.21}$$

where $\alpha_f$ is the attenuation coefficient given in per unit length. Unit conversion to dB per unit length can be achieved by multiplying the result by 10log(e) (≈ 4.343). Fibre propagation loss originates from scattering, absorption and bending but does not include external losses (e.g. input and output coupling losses). Therefore, in each group of measurement, the input end should always be fixed. After each single measurement, a certain length of fibre is removed from its end in order to collect results at different L values. Regarding the output coupling, in the present study, a spectrometer was employed for its higher sensitivity than that of the power meters available in the laboratory. With its 25-μm-slit being wider than the samples' core diameters, the measurement error induced by possible variation in the output coupling efficiency was minimised by carefully setting the fibre adaptors and repeating cleaving to maximise the collected output power for each data point.

Data processing with results from multiple sample lengths minimises the random error of a data set. In each data set, the output from the shortest fibre length is employed as a reference, i.e. P(0) in Equation (2.21). Then, L becomes sample length relative to the shortest value, and together with

P(L) gives $\alpha_f L$. The random error is then minimised by plotting $\alpha_f L$ as a function of the relative length $L$, the slope of a linear fitting of which gives the attenuation coefficient $\alpha_f$.

## 2.5.2 Dopant concentration

The concentrations of $Gd^{3+}$ ions doped in the silica fibre samples were measured using an energy-dispersive X-ray spectroscopy (EDX) system integrated on a scanning electron microscopy (SEM) system [72,73].

Electron microscopes exploit the wave-like characteristics of electrons, a remarkable theory first proposed by Louis de Broglie in 1924. The wavelength as well as the resolution of EDX is thus governed by the acceleration voltage applied on electrons. When such an electron beam is focused on a sample, various interactions (see Figure 2.10) result in backscattered electrons from the sample nucleus and the emission of secondary electrons, X-rays and Auger electrons, providing information on the morphology, topography and composition of the sample.
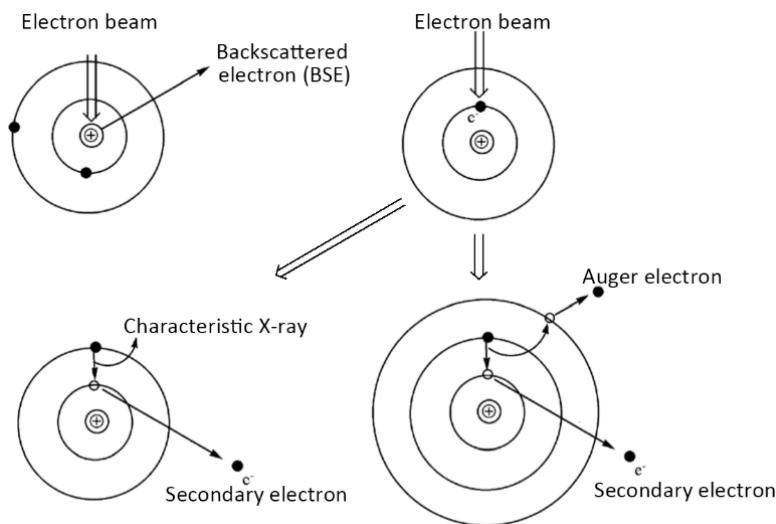


Figure 2.10 Types of possible interactions between the incident electron beam and the nucleus and electrons of surface atoms [72].

Among these, the X-ray is generated by the electron transition from a higher-energy shell to a lower-energy one, the energy gap of which is a unique characteristic of each element. Therefore, it can be exploited as a fingerprint for composition identification. Using this method, hydrogen with only one shell cannot be identified, and quantitative analyses of light elements with atomic numbers of less than 11 and elements of low concentrations are limited by their weak signals and detector sensitivity. Besides, it should be noted that in high vacuum, electrons accumulating on the surface of a non-conductive sample results in a distortion of the incident beam, which can be avoided by either coating the sample with a thin layer of conductive material (e.g. gold and carbon), or by taking measurements under a variable pressure mode to dissipate the charge of electrons.

The resolution of EDS varies with SEM accelerating voltage and sample density which determines the interaction volume. The signal-to-noise ratio can be improved by adjusting the probe current to optimise the collection rate. The concentration can be evaluated according to signal intensity. In the present study, quantitative analyses were realised based on calibration performed with a standard Cobalt sample and by employing Oxford INCA EDS software for data processing. The errors in EDX measurements are also governed by sample homogeneity, flatness and cleanliness. By carefully handling and pre-processing the samples, which is reported in Chapter 4, all of the expected elements were identified with the concentration ratios following chemical formulas.

### 2.5.3    Refractive index profile

In the present study, the refractive index profiles of fibre samples were taken by collaborators using an S14 fibre refractive index profiler in the Silica Fibre Fabrication group at the ORC. This equipment measures the refractive index fibre point-by-point at the fibre end face based on refracted near field technique [74], the mechanism of which is illustrated in Figure 2.11.
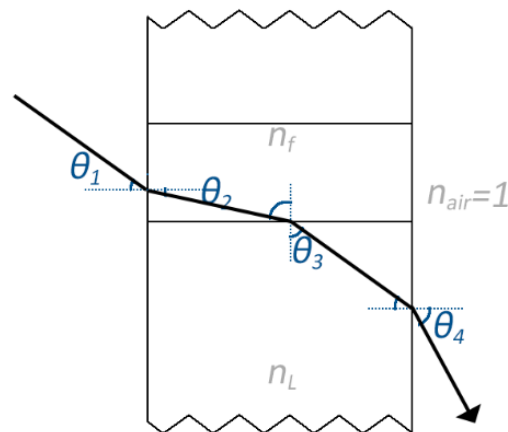


Figure 2.11 Refracted near field technique for characterising fibre refractive index profile.

The fibre is set in an index liquid cell. The relation between incident angle $\theta_1$, $n_L$, and exit angle $\theta_4$ can be derived according to Snell's Law:

$$n_f^2(r) = n_L^2 + \sin^2(\theta_1) - \sin^2(\theta_4) \qquad (2.22)$$

In the measurement, $\theta_4$ can be fixed by the location of the detector afterwards, which collects power at an exit angle larger than $\theta_4$. This amount of power is equivalent to that of the incident at an incident angle larger than a corresponding $\theta_1$ in Equation (2.22). Therefore, by comparing the collected power with the total incident power and taking the exact measurement configuration—which may be companied with addition losses—into consideration, the relationship between these angles as well as the refractive index of fibre at a measured radial position $n_f(r)$ can be obtained.

## 2.6    Summary

The theories behind the optical guidance mechanisms in OMFs have been reviewed in this chapter. The solutions of Maxwell's equations based on certain boundary conditions in fibres and for WGMs in a spherical structure have been collectively presented, based on which the field distributions of modes studied in this research will be given in the following chapters. Theoretical prediction of THG conversion efficiency requires careful consideration of the mode properties in OMFs, which differ from those in standard SMFs. Both SHG and THG require phase matching conditions to be achieved with the respective methods presented in Chapter 3.

# Chapter 3    All-fibre Sixth Harmonic Generation of DUV

In this chapter, all-fibre sixth harmonic (6H) generation of deep UV (DUV) light is demonstrated by cascading the second harmonic and third harmonic generation, beginning with a theoretical prediction of the phase-matching diameter of OMFs required, followed by OMFs fabrication. Then, a PPSF is characterised and employed to generate the second harmonic from a 1550 nm laser source at a peak power of around 300 W. This frequency-doubled output is employed as a pump source for the THG in a sub-micron diameter optical fibre to generate a DUV signal. This work was conducted in collaboration with Timothy Lee and Francesco De Lucia at the ORC.

## 3.1    Theoretical analysis of THG in OMFs

Given the optical mode properties in Chapter 2, the use of OMFs benefits nonlinear phase-matched parametric processes such as THG [19] and four-wave-mixing [20], not only because the diffraction-limited confinement in OMFs leads to high pump intensities and thus results in high conversion efficiency, but also because the dispersion can be tailored by optimising the fibre diameter to meet the phase-matching condition between the pump fundamental mode and a harmonic higher-order mode, which experience a large modal overlap with each other. To find the theoretical OMF diameters for phase matching the pump (i.e. the SH output from the PPSF) with its third harmonic in the DUV, the demonstration of all-fibre 6H generation begins with the theoretical analysis of the THG in air-clad silica OMFs, based on the solutions to the rigorous modal eigenvalue equations [35] as introduced in Chapter 2.

The effective index dependence on the diameter of an air-clad silica OMF is plotted in Figure 3.1a, with each intersection point corresponding to a phase-matching diameter. The harmonic $HE_{11}$ mode, with a similar field distribution to that of the pump and thus potential high-efficient power coupling, does not intersect with the pump in this plot, due to the dispersion explained in the previous chapter. Consequently, third-harmonic high-order modes should be considered candidates for THG. To select the most efficient one, the modal overlap integral $J_3$ between the pump and the harmonic is evaluated at each PMD using Equation (2.16). Only results with non-zero $J_3$ overlap are considered, which are hybrid modes with $v = 1$ or 3. The TE, TM, and other harmonic hybrid modes are not included due to modal field symmetry [19].

Figure 3.1b visually interprets the physical meaning of $J_3$. Inside the silica core, the pump $HE_{11}$ mode features a peak at the centre and is linearly polarised with an azimuthal mode order of $v = 1$. In the results for the harmonic modes, besides the $HE_{11}$ mode, the $HE_{12}$ mode shows the most similar distribution, whereas the field of the rest oscillate relatively more frequently at the azimuthal

direction with 'holes' at the centre. As expected from these modal field distributions, the harmonic $HE_{12}$ mode with the best overlap with the pump gives the highest $J_3$ value.
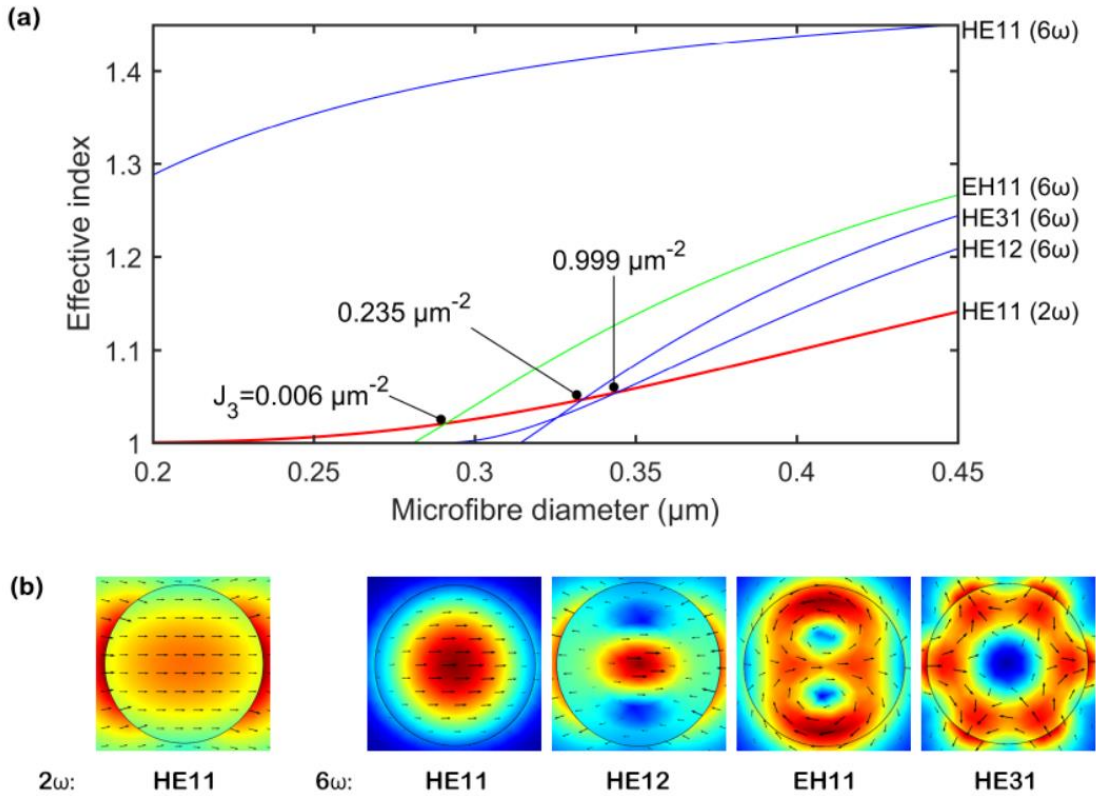


Figure 3.1 (a) Dependence of the effective index on the air-clad OMF diameter for the SH fundamental mode at $\lambda$ = 775 nm and 6H high-order modes at $\lambda$ = 258 nm. The values of the modal overlap integral $J_3$ for each PMD are labelled for reference. (b) Modal field |E| distribution for SH fundamental and 6H higher-order modes.

The conversion efficiency is simulated using the equations derived by Grubsky and Savchenko [49] and presented in Chapter 2. As most silica-related defects exhibit absorption in the UV [75], the attenuation of the fibre used in the OMF fabrication was characterised via the cut-back method, resulting in a loss of $\alpha$ = 0.09 dB/cm at $\lambda$ = 258 nm. It should be noted that in the cut-back measurement, power was mostly confined in the fibre core; whereas the loss of F-doped fibre cladding is not accessible, 0.09 dB/cm is adopted as an estimation. The phase mismatches associated with the cross and self-phase modulation are compensated by optimising the detuning term, which is physically achieved by detuning the optimised diameter. The results in Figure 3.2 suggest that, in theory, at a pump peak power of 200 W, the harmonic UV power grows quadratically at a short propagation distance. Then, the pump depletes, and the total power reduces due to the absorption loss, leading to slow modification of the effects of XPM and SPM as well as the detuning term, which implies a phase mismatch. Before the power flow direction alters, the conversion efficiency reaches a plateau with conversion efficiency higher than 50% at L ≈ 3.5 cm, which hints an optimal length of the OMF required to be fabricated. Yet, it should be noted that the

assumption of a uniform taper waist region in the simulation is not guaranteed in reality, in particular, at small OMF diameters, which will be discussed in Section 3.5 with an updated model.
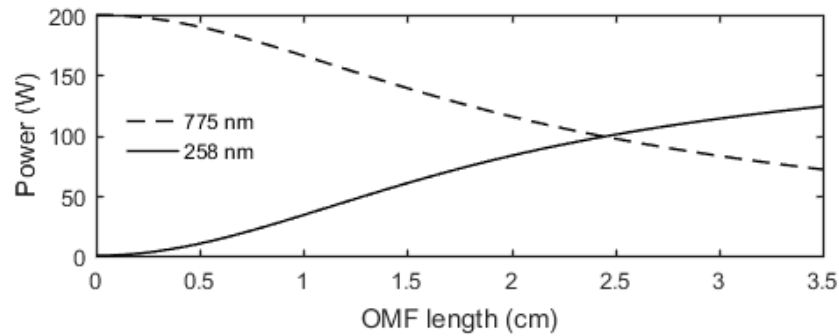


Figure 3.2 Simulated conversion for 6H generation (i.e. the THG from λ = 775 nm) as a function of the OMF length.

## 3.2 OMF fabrication

According to the simulated results, a microfibre with a diameter close to the PMD of 344 nm for phase matching is required to be fabricated for 6H generation (i.e. the third harmonic of the second harmonic at $\lambda_{SH} \approx 775$ nm from the PPSF). Because the commonly used telecom fibre SMF-28 is not transparent in the UV due to the absorption induced by its Ge dopant, the microfibres in this work were fabricated from a submarine fibre (Z fibre, Sumitomo Electric) with a fluorine-doped-silica cladding and a pure-silica core (Figure 3.3a). With the ceramic heater-based brushing technique [39], the fibre section without coating is initially set straight and horizontally with both ends fixed on two computer-controlled transition stages.
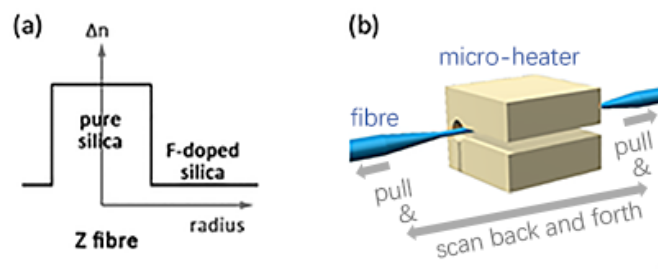


Figure 3.3 (a) Refractive index profile of the Z fibre used for fabrication of microfibres and (b) schematic diagram of the tapering process.

During fabrication, the middle section is placed inside a ceramic heater (Figure 3.3b). Compared with a torch flame, ceramic micro heater provides a more stable, uniform, and repeatable heating. The temperature at the centre of the heater is above the glass transition temperature (~1200°C for silica glass) to sufficiently soften the material. The two stages move synchronously to translate the fibre back and forth through the heater. Meanwhile, the gap between them increases with time so that the fibre is tapered. The tapered fibre has a uniform waist region with two transition regions

29

at both ends. The shape of the transition region can be tuned by programming the brush speed and length. In this study, the taper transition was engineered by setting the profile parameter to zero, leading to a slowly varying exponential transition profile [76].

## 3.3    PPSF characterisation

The fundamental frequency signal for the experiment was generated from a fibre MOPA system [20] operating at λ ≈ 1550 nm, which is introduced in Section 2.4. The pulse duration and repetition rate were set to 4 ns and 200 kHz, respectively.

The generation of periodical $\chi^{(2)}$ in silica fibre, which initially lacks any significant second-order nonlinearity $\chi^{(2)}$ has been introduced in Chapter 2. Before being spliced to the system, the PPSF was characterised using the seed source of the MOPA, a tunable ~ 1.55 μm continuous-wave laser (Tunics BT, Photonetics) with a polarisation controller which was adjusted to maximise the output at SH. The PPSF spectral response was checked by sweeping the wavelength of the source while monitoring the PPSF output using a power meter (S130VC, Thorlabs). The results indicated a PPSF working bandwidth of 1.25 nm. Then, the output SH power was recorded at a different input power. The corresponding conversion efficiency is plotted in Figure 3.4a as a function of the input pump power, which confirms the theoretical linear relationship between them as well as a square dependence of the output power on the input power. With a linear fitting, the results suggest a conversion efficiency of $1.56 \times 10^{-2}$ %/W for this 30-cm-long PPSF.

The effective $\chi^{(2)}$ of the PPSF was then evaluated by recording the input and output pump power as well as the output harmonic power. Because the PPSF has a different refractive index profile from that of the standard step-index fibres used by the pump, splicing loss is not negligible. Assuming a harmonic splicing loss close to the 0.85 dB loss recorded at the pump wavelength, characterisation using the low-power continuous-wave seed source and the pulsed MOPA both suggested a $\chi^{(2)}$ of 0.04 pm/V for the PPSF used here. Although $\chi^{(2)}$ is somewhat smaller than the previously published values [65], the relatively large operational bandwidth allows the system to operate without a temperature controller, which is otherwise recommended. The output spectrum at high pump power was monitored using a spectrum analyser (AQ6370, Yokogawa) for the infrared and visible regions and a coupler with attenuation of around -20 dB and -10 dB at the fundamental and harmonic wavelengths, respectively. The SH signal-to-noise ratio and linewidth were estimated to be larger than 40 dB and ~0.03 nm, respectively (Figure 3.4b). No nonlinear broadening or output in different spectral regions was observed. A single-mode fibre with a cut-off wavelength below 750 nm (SM750, Fibercore) was spliced to the PPSF output before the tap coupler to reduce the 1550nm pump, which could otherwise saturate or damage the spectrometer employed later.
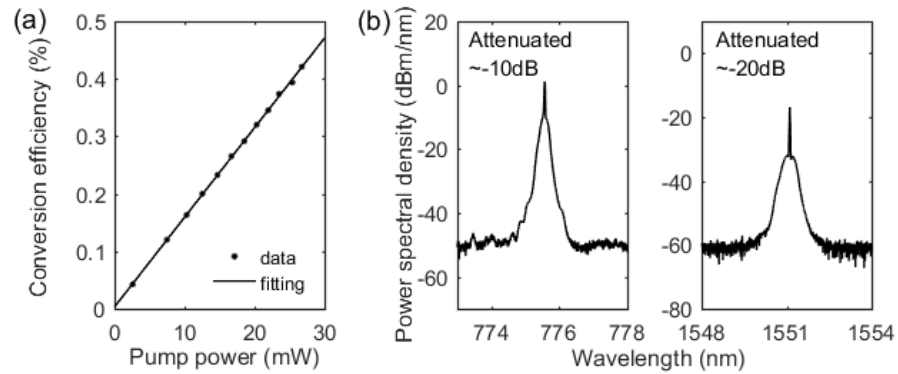
Figure 3.4 (a) Conversion efficiency for the 30-cm-long PPSF, and (b) attenuated SH and pump spectra.

## 3.4 Sixth harmonic generation

Figure 3.5 shows a schematic diagram of the setup for the 6H generation, with the output of the MOPA system characterised using an oscilloscope (DSA8200, Tektronix). At the beginning of each experiment, the PPSF was again connected to the seed source through a polarisation controller. The pump wavelength was optimised by maximising its output power at SH. Then, the PPSF was spliced to the MOPA output end, which avoids the use of fibre adaptors and connector-induced coupling losses. The SM750 fibre was bent to minimise the pump residue. The tap coupler was replaced with one with attenuation of around -20 dB at 775 nm, which delivered 1% of SH power to a detector, to optimise PPSF efficiency before each measurement and to monitor the relative SH power during 6H generation in real time.
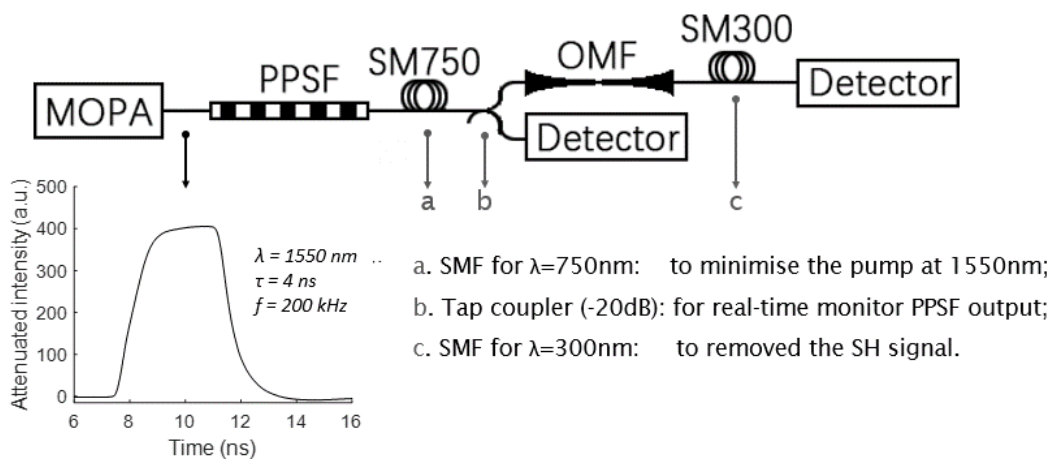


Figure 3.5 Schematic diagram of the setup for sixth harmonic generation and detection, with the output of the MOPA system characterised in the time domain.

The SH signal was then delivered as a pump of the following THG process to a Z fibre required to be tapered. A short piece of single-mode UV-transparent fibre with a cut-off wavelength below 310 nm (SM300, Thorlabs) was spliced to the Z fibre output as a power-delivery fibre. This fibre was

employed to remove the SH signal at λ ≈ 775 nm to avoid saturating the spectrometer with background noise. It is also relatively transparent in the DUV without obvious material defect-induced absorption at around 250 nm, which might otherwise be detrimental for the observation of the generated 6H. To eliminate light scattered in the cladding at the splicing point, part of the SM300, with its polymer coating being replaced with graphite-based adhesive, was bent. The same method was also used to remove cladding modes for fibre-loss characterisation, a photograph of which is presented in Chapter 4.

The Z fibre was then tapered, during which the output after the SM300 fibre was monitored in real time using a UV spectrometer (USB Series, Ocean Optics), and a DUV signal at λ ≈ 258.5 nm was observed. The spectral intensity at this wavelength was extracted from the recorded spectra and plotted with time in Figure 3.6 (red curves). As the tapering continued, the phase-matching region shifted to different positions along the transition region, leading to a long tail at the vanishing side of the peak in the time domain. Before and after the emergence of the 6H, signals at λ ≈ 387.5 nm were also observed. This is believed to be the fourth harmonic (4H), which is based on bulk multipole nonlinearities and surface dipoles [75,77]. The theoretical PMDs for SH generation from a λ = 775 nm pump are D = 329 nm and 373 nm for power conversions into the harmonic $TM_{01}$ and $HE_{21}$ modes, respectively.
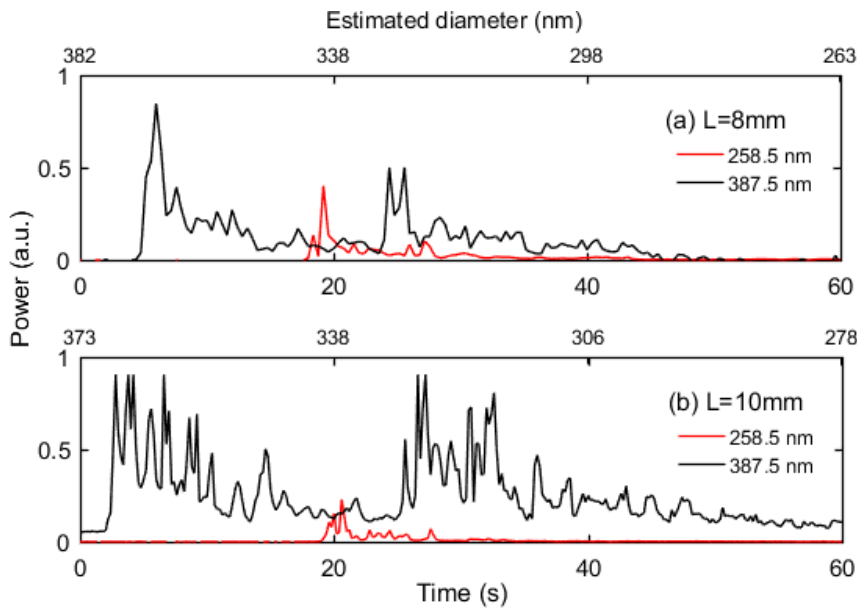


Figure 3.6 Power at the 6H (258.5 nm) and 4H (387.5 nm) extracted from spectra recorded with time during fibre tapering from (a) an 8-mm-long and (b) a 10-mm-long microfibre. Note that the starting point of the time axis is arbitrary.

While short tapers have low conversion efficiency, tapers with long transition regions are likely to have poor signal-to-noise ratios (Figure 3.6b, for instance) due to the tail of the first 4H generated

in the taper transition region and the movement of the holder during fibre tapering. Therefore, most microfibres were fabricated to have a waist length of 8 mm.

To compare the PMD to the theoretical predictions, fibre tapering was terminated at the onset of the 6H for SEM imaging. Due to the high tapering temperature and thermal-optic effect (dn/dT $=1.1\times10^{-5}$/°C for silica), the OMF diameter was found to be ~ 5 nm smaller than the PMD simulated for room temperature (Figure 3.7a). To measure the maximum 6H power, the tapering process should be terminated when the fibre diameter reaches exactly the PMD; yet, this is challenging due to the limited tuneable SH wavelength range, which implies that a diameter control precision smaller than 0.7 nm is required (Figure 3.7b).
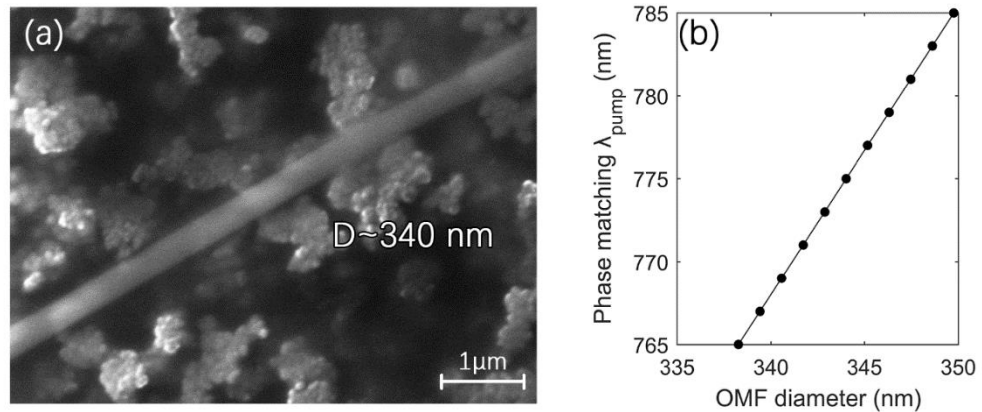


Figure 3.7 (a) SEM image of the taper waist and (b) the theoretical phase-matched SH wavelength against the OMF diameter for 6H generation.

Because of the thermally induced shift mentioned above, the 6H power dependence on the SH power was examined by terminating the fibre tapering at the onset of the DUV signal and varying a polarisation controller before the PPSF to change its efficiency as well as the power at SH while monitoring a fraction of the output from the tap coupler, when the OMF was kept inside the micro-heater. Figure 3.8a shows the output spectra in the DUV recorded at different SH power. The relative total power obtained by integrating the area under each curve is plotted in Figure 3.8b as a function of the attenuated SH power, which suggests a 6H power dependence on the SH power close to the theoretical cubic trend.

The output spectrometer was then replaced with a high-sensitivity power meter (PD300R-UV, Ophir). The presence of the 6H was confirmed by monitoring the estimated diameter and the three-peak profile given by both the 4Hs and 6H. Sweeping the OMF diameter and detuning in the simulation suggests that, around the point where efficiency is most sensitive to the diameter, a change of 0.013 nm in diameter can cause a detuning of 300 m$^{-1}$, which can halve the 6H power. The speed at which the OMF diameter decreased during tapering was estimated to be about 1.7 nm/s around the PMD, which suggests that the peak power generated in the taper region lasted
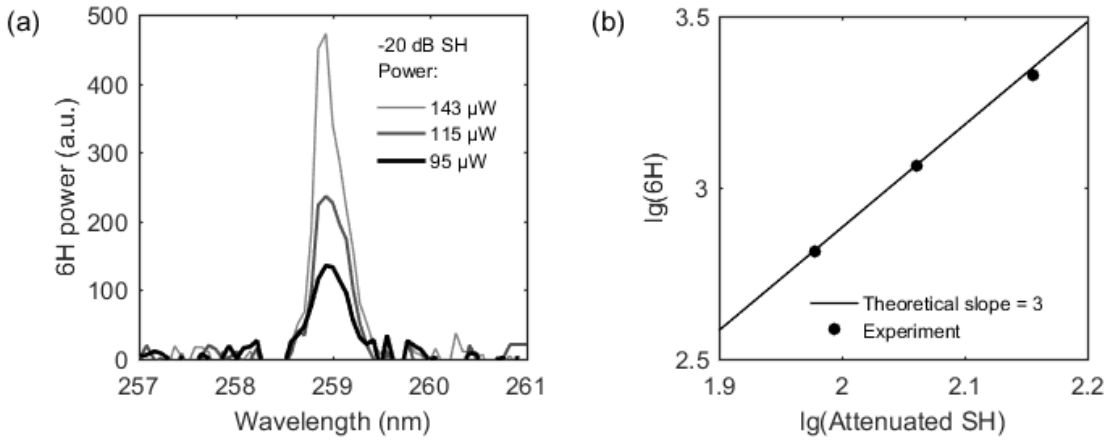
Figure 3.8 (a) 6H spectra for different attenuated (-20 dB) SH average power, and (b) data processed from (a) showing the 6H power dependence on the SH power.

~ 8 ms during fibre tapering. As the power meter response time is 0.2 s, the power reading is averaged over this period and therefore over an order of magnitude less than the exact experimental maximum value.

When the peak power at $\lambda \approx 775$ nm was 13 W, which, according to the conversion efficiency of the PPSF, corresponds to a fundamental peak power of nearly 300 W at $\lambda \approx 1550$ nm, the average 6H power in the DUV recorded during fibre tapering for an OMF length of 8 mm was 0.15 nW, corresponding to a peak power of 0.18 µW, after subtracting the background noise level of 0.15 nW induced by 775 nm residue (see Figure 3.9).
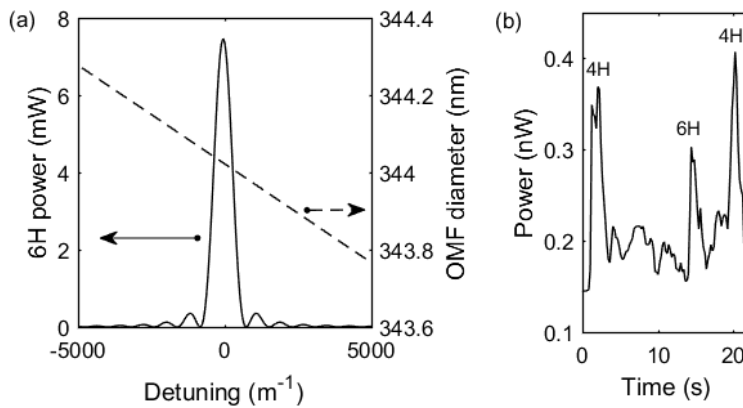


Figure 3.9 (a) Simulated relationship among the OMF diameter, 6H power, and detuning. (b) Power recorded during fibre tapering. The power meter was calibrated for the 6H wavelength only.

For comparison, by repeating the simulation in Figure 3.2 using the experimental SH power, the theoretical prediction of the 6H power is 7 mW. During fibre tapering, the background power level arising from the SH residue at $\lambda \approx 775$ nm was checked from the beginning to ensure that the fibre was straight. Besides the reduction in measured power related to the slow power meter response

time, a difference of approximately two orders of magnitude in the conversion efficiency is attributable to microfibre surface roughness.

## 3.5    Discussion

First, as the OMF is manufactured with a continuous molten glass reflow, the surface roughness is mostly associated with surface waves arising from fluctuations present at high temperatures during fibre fabrication [78,79]. This is modelled and confirmed by approximating the OMF radius r(z) as a sinusoidal variation for the 6H generation from the SH. As illustrated in Figure 3.10, when both the fibre radius deviation ($\Delta a$) and the fluctuation amplitude ($\Delta b$) are 0.5 nm and the period ($\Lambda$) is 1 µm, the theoretical 6H peak power reduces from 7 mW to below 30 µW, which is consistent with previous results [53]. Moreover, depending on the exact scale of the fluctuation that varied sample by sample, light random scattering at the boundary might also result in additional losses. However, this fluctuation in OMF radius can be compensated by post-processing the OMF. For example, the approach for surface nanoscale axial photonics in [80] with $CO_2$ lasers can provide sub-angstrom precision in the fibre radius uniformity. With a uniform OMF, the results can be improved by two orders of magnitude or even higher if a longer OMF is used.
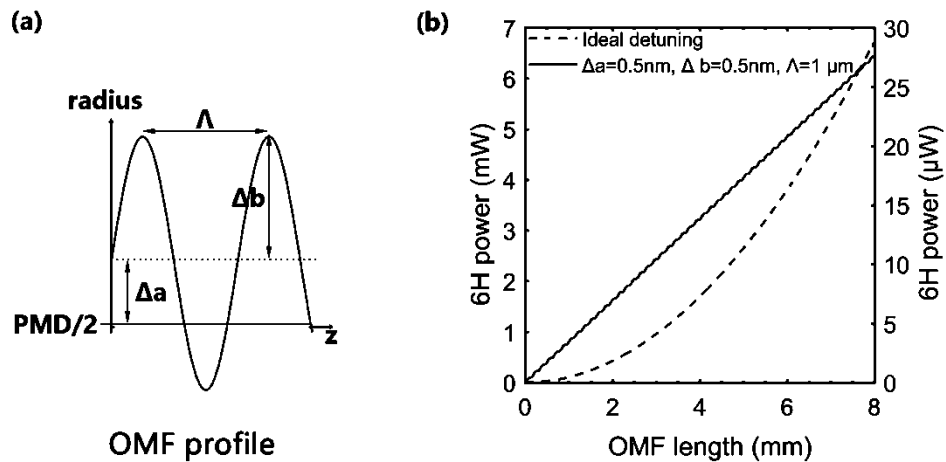


Figure 3.10 (a) Radius profile of the OMF with a surface wave, and (b) its impact on 6H conversion.

Second, as mentioned above, compared with the response time of the power meter, the 6H signal is fleeting in each tapering process. Because of this, the recorded 6H power is over an order of magnitude less than the exact experimental maximum value. One of the possible solutions is to improve the tapering process. The fabrication of each OMF with such a small diameter took 10 to 20 minutes, depending on the OMF length. Reducing the tapering speed, which is constant, facilitates diameter control but would increase the entire fabrication time and the risk of contamination or sample damage during fabrication. This could be solved by improving the program to tune the tapering speed or to pause and continue the process during a single fabrication. Another

solution is to apply a force to or change the temperature of the PPSF, to tune its central wavelength as well as corresponding PMD in Figure 3.7b to match the exact OMF diameter.

Third, optimising PPSF efficiency or increasing its length can also improve the overall efficiency. The PPSF was fabricated using an up-to-date method. From previous publications, a high $\chi^{(2)}$ value of 0.12 pm/V is achievable. With an efficiency of 0.08 %/W, the second harmonic peak power can be 72 W, or much higher than this if a powerful pump source at 1550 nm is used. Therefore, under the best-case scenario, with efficiencies of 24% (or > 30% with a powerful source) for the PPSF and 60% for the THG in the OMF, respectively, a total efficiency higher than that achieved with nonlinear optical crystals can be expected.

Moreover, in silica, defect-related absorption results in additional losses in the UV, which is discussed in the following chapters. A cut-back measurement performed on an untapered Z fibre suggests a propagation loss of 0.2 dB/cm at $\lambda \approx 250$ nm, the central wavelength of oxygen deficient centre absorption band. The light in the untapered fibre propagates in the pure silica core, while in the OMF, it mostly overlaps with the F-doped silica cladding. The diffusion of F [81] at high temperatures may lead to an inhomogeneous refractive index distribution, which further results in scattering losses [82] and coupling losses in the taper transition region. Its influence depending on fibre tapering temperature and time requires further investigation.

## 3.6 Summary

In conclusion, the 6H generation of DUV light from a $\lambda$ = 1550 nm pump has been simulated and experimentally demonstrated in a fully-fiberised system by cascading the second and third harmonic generation using a periodically poled silica fibre and an optical sub-micron diameter fibre. The temporal walk-off was minimised by using a nanosecond pulse laser as the pump. A power of 0.15 nW was recorded at a wavelength of 259 nm. As discussed above, the low reported efficiency is primarily because of the surface capillary waves that dramatically reduce the effective OMF length and partly because of the ephemeral 6H signal. Therefore, under the best-case scenario, with well-controlled diameters or a wavelength-tunable pump source and a uniform OMF, which can be obtained by, for example, post-processing the OMF, an improvement by orders of magnitude with respect to the present result can still be expected for applications in the future.

# Chapter 4    Absorption in Gd-doped Silica Fibres

In chapters 4–7, Gd doped in silica/phosphosilicate glass, especially in glass fibres, is investigated as a possible candidate for the development of coherent solid-state sources in the UV region, followed by a laser demonstration using doped silica microspheres in Chapters 6 and 7. Chapter 4 begins with a brief background on lasing operation and rare-earth elements with emphasis on Gd in Section 4.1. Then, an introduction of the doped samples fabricated by the collaborators for this project is provided in Section 4.2. The measurement of the Gd concentration using energy-dispersive X-ray spectroscopy, followed by fibre propagation loss characterisation is presented in Section 4.3.

## 4.1    Rare-earth ions

In 1900, when solving the problem of blackbody radiation, Planck proposed that the emission of electromagnetic energy is quantised and distributed into different modes of charged oscillators [83]. The energy levels of the oscillators are discrete and can only be integer multiples of a fundamental unit of energy E = hυ, where h and υ are the Planck constant and radiation frequency, respectively.

In 1913, to interpret the emission lines of the hydrogen atom, Bohr introduced a model in which the electrons travel around the nucleus and are limited within a discrete set of orbits with definite energies. A transition between two states is accompanied by a change (i.e. gain or loss) in energy given by $\Delta E \equiv |E_1 - E_2| = h\upsilon$, where $E_1$ and $E_2$ are the energy of the initial and final states, respectively [84]. The population at these states obeys the Boltzmann distribution at thermal equilibrium. Absorption is dominant in the absence of a pump.

After being excited to higher energy levels by absorbing energy, the electrons will generally decay via radiative and non-radiative processes. Radiatively, the transitions of excited ions from the upper levels to lower levels give rise to spontaneous emission and stimulated emission. The latter requires positive population inversion and incidence photons. Because the photon generated via the stimulated emission process is in phase with the incidence photon with the same propagation direction, the laser (i.e. light amplification by stimulated emission of radiation) features excellent temporal coherence. Non-radiatively, the released energy may also be dissipated as phonons or absorbed by other ions via, for example, collisions and light reabsorption, which facilitates processes such as excited state absorption [85], photon avalanche [86], and co-doped fibre lasers.

To preserve excited ions in the upper state for laser transitions, a relatively long upper-level lifetime is desirable. The decay lifetimes for fully allowed transitions are around $10^{-8}$ s [21], whereas, for

rare-earth ions doped in glass, the upper-level lifetimes are in the order of microseconds or milliseconds, as the electric-dipole transitions within 4f levels are parity forbidden in the free ion and become weakly allowed in solids due to a mixture of wave functions with opposite parities [21,87]. The weakness is due to the screening effect of 5s and 5p levels on the inner 4f level electrons, which also leads to sharp transition lines.

Another advantage of rare-earth ions is their abundant energy levels. In 1963, G. H. Dieke and H. M. Crosswhite reported a remarkable energy level graph for triply ionised rare-earth ions [88]. In 2000, this diagram was extended from 40,000 cm$^{-1}$ to 70,000 cm$^{-1}$ by Wegh et al [89]. To date, numerous optical fibre lasers operating in the infrared IR and visible have been demonstrated based on the spectroscopic properties of rare-earth ions [21], such as Nd (1.36 μm, 1.06–1.09 μm, 0.90–0.94 μm), Er (1.53–1.62 μm), Yb (0.98 μm, 1.02–1.14 μm), Tm (1.9–2.1 μm), and Ho (2 μm).

Though larger energy gaps in the energy level graph indicate shorter wavelengths, the intermediate levels between two far-apart levels cause radiative decay at relatively longer wavelengths and non-radiative decay. However, in the case of Gd$^{3+}$, the first excited state $^6P_{7/2}$ is located at a wavenumber of $\tilde{v} \approx 32000$ cm$^{-1}$ above the ground state $^8S_{7/2}$ (see Figure 4.1), corresponding to the emission in the UV at λ ≈ 312.5 nm.



Figure 4.1 Energy levels of Gd$^{3+}$ (adapted from [7,8]).

Previous studies of Gd-doped samples in film, bulk, and powder form under electron-beam, VUV, and X-ray excitation [90–92] have suggested that the emission given by this $^6P_{7/2} \rightarrow {}^8S_{7/2}$ transition would be a promising candidate for the generation of light in the UV. Photon cascade emission of orange/red, near-IR, and UV light from Gd$^{3+}$ $^6G_J \rightarrow {}^6P_J$, $^6G_J \rightarrow$ $^6I_J$, and $^6P_J \rightarrow {}^8S_J$ transitions, respectively, under $^8S_{7/2} \rightarrow {}^6G_J$ excitation have been reported in Na(Y, Gd)FPO$_4$ [92], where non-radiative multi-phonon relaxation dominated the transitions among $^6D_J$, $^6I_J$, and $^6P_J$ due to their small energy gaps. Similar results have also been reported in other hosts, such as GdBaB$_9$O$_{16}$ crystal [91] and LiGdP$_4$O$_{12}$ powder phosphor [93]. The lifetime of the $^6P_{7/2}$ level has been found to be 5 ms in a sol-gel sample containing ~3 mol% of Gd [94]. Rapid thermal treatment on a Gd-doped sol-gel silica bulk sample resulted in the enhancement of Gd$^{3+}$ luminescence [95].

In chapters 4–7, Gd doped in silica fibres is investigated. Silica glass, the host material, has various advantages, including transparency in the UV spectrum down to λ ≈ 200 nm [17,18], extraordinary mechanical strength, strong chemical resistance, and compatibility with existing silica-based components. Moreover, the silica network has high phonon energy ($\tilde{v} \approx 1100$ cm$^{-1}$ [96]). Since the non-radiative decay rate $W_{nr}$ is exponentially dependent on the energy gap between the two states:

$W_{nr} = A \exp(-B\Delta E/h\nu)$, where A and B are constants depending on the host materials [87], transitions with smaller energy gaps that require fewer phonons are more likely to occur. Multi-phonon relaxation is supposed to be dominant in the transitions among the $^6D_J$, $^6I_J$, and $^6P_J$ energy levels in $Gd^{3+}$.

## 4.2    Gd-doped silica samples

Two types of Gd-doped fibre samples with doped phosphosilicate (sample A and C) and doped silica (sample B) cores were made for this project. The germanium silicate glass that is commonly used for telecom fibres is not considered a host material here due to its three absorption bands in the UV wavelength region at λ = 185 nm, 242 nm, and 325 nm [97].

### 4.2.1    Refractive index profiles

This section introduces Gd-doped fibre samples fabricated with refractive index profiles measured by collaborators for this project.

### 4.2.1.1    Doped phosphosilicate fibre sample A

The phosphosilicate fibre sample (sample A) was fabricated by the silica fibre fabrication group at the ORC using the modified chemical vapour deposition (MCVD) and solution doping techniques [98]. The core layer formed by un-sintered porous soot was deposited inside a silica tube (F-300, Heraeus) at a temperature of T ≈ 1530°C by oxidising the vapour-phase precursors $SiCl_4$ and $POCl_3$. The tube was subsequently soaked for about one hour in a solution containing $GdCl_3 \cdot 6H_2O$ dissolved in methanol. The core layer was then sintered, and the tube was collapsed into a preform with silica cladding and a Gd-doped phosphosilicate core. The preform was subsequently pulled into an optical fibre at T ≈ 2040°C. Figure 4.2 shows its refractive index profile, in which the Δn denotes the refractive index contrast.

The fibre has the core and cladding diameters of $d_{co}$ = 5.8 μm and $d_{cl}$ = 125 μm, respectively, and a numerical aperture (NA) of 0.13. The UV curable polymer coating has a lower refractive index than the cladding; hence, it supports cladding modes, which may facilitate a two-photon cladding pump in the visible.

Note that the refractive index is related to dopant concentrations [99], the distributions of which lead to the dip at the centre. This dip is commonly observed in MCVD fibres and preforms and is attributed to the evaporation of $P_2O_5$ during consolidation, which also removes Gd ions. Therefore, similar features can also be found in the dopant concentration characterisation results in Section 4.2.2.
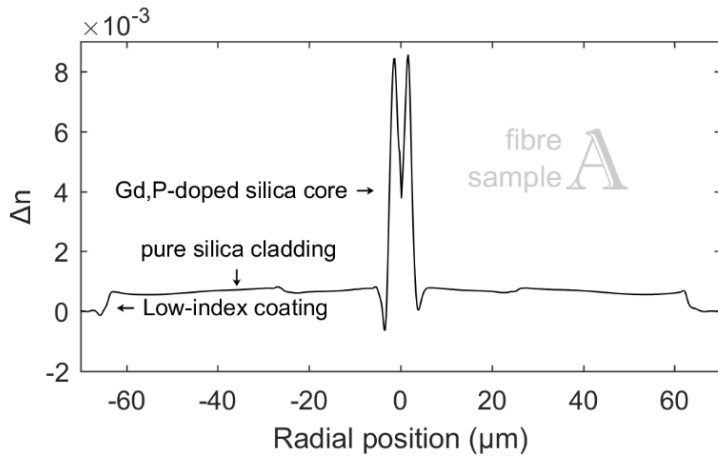
Figure 4.2 Refractive index profile of the Gd-doped phosphosilicate fibre sample A. (Data were collected by Pranabesh Barua at the ORC.)

### 4.2.1.2    Doped silica fibre sample B

Sample B has a Gd-doped silica core fabricated by Norberto Chiodini at the University of Milano-Bicocca via the sol-gel method [100], which is then drawn into a fibre at the ORC using the rod-in-tube technique with fluorosilicate cladding. Tetramethoxysilane and $Gd^{3+}$ nitrate were put under sol-gel reaction in a 4:1 methanol to water solution. After gelation at T ≈ 45°C, the alcogel was subsequently slowly dried to a xerogel in a thermostatic chamber at the same temperature and finally densified under a controlled atmosphere in an oven at T ≈ 1250°C. Further densification was achieved during the fibre drawing process at a temperature above T ≈ 2000°C. This silica rod made via the sol-gel method contained $Gd^{3+}$ ions in a concentration of 1000 ppm. It was pulled into a 500-μm-diameter cane and then set inside a cladding tube to be pulled into a fibre with the core and cladding diameters of 10 μm and 125 μm, respectively. The depressed silica cladding was doped with fluorine to decrease the refractive index, resulting in NA of ~ 0.05. Figure 4.3 shows its refractive index profile.
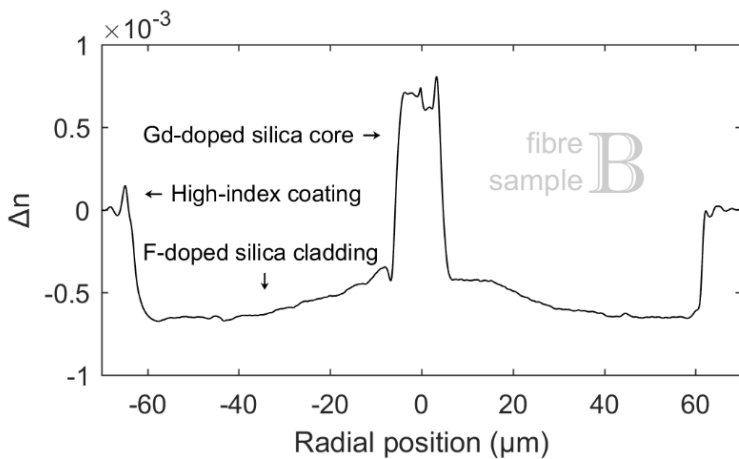


Figure 4.3 Refractive index profile of doped silica fibre sample B measured at 622.8 nm using the S14 refractive index profiler. (Data were collected by Pranabesh Barua at the ORC.)

### 4.2.1.3      Doped phosphosilicate fibre sample C

Later, another phosphosilicate sample (sample C) was made using the same technique as that for sample A but with a fluorine-doped silica tube for its cladding and a high-index polymer coating. The refractive index profile is shown in Figure 4.4, suggesting a core diameter of 6.3 mm and a NA of 0.135. Depending on the fabrication parameters and also due to the nature of the MCVD technique, sample A and C have different dopant concentrations and optical properties. Measurement of the preform was taken at different longitudinal positions, z = 60 mm and 80 mm. The latter position is close to the fibre-pulling endpoints, where a disk sample was collected for measurement of the dopant concentrations.
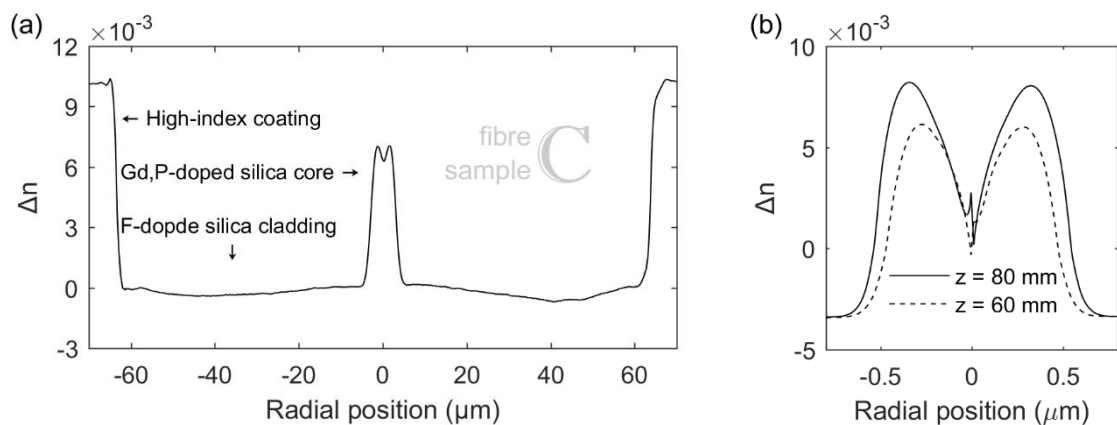


Figure 4.4 Refractive index profiles of the doped phosphosilicate (a) fibre and (b) fibre preform sample C. (Data were collected by Robert J. Standish and Pranabesh Barua at the ORC.)

### 4.2.2      Gd concentrations

As refractive indexes are modified depending on dopant types and concentrations [99], the results above imply non-uniform dopant distributions because of the nature of the MCVD techniques. The EDX technique was then employed for dopant concentration characterisation.

Given the precautions in Section 2.5, in this study, before EDX measurement, the disks were polished using LP50/PM5 equipment with alumina slurry and colloidal silica slurry, followed by coating with a ~30-nm-thick carbon layer on each sample to avoid the charging effect caused by the electrons accumulating on the insulator sample surfaces and thus avoid distorting the incident beam. The resolution—which varies with the sample density and equipment settings, in particular the SEM accelerating voltage—was nearly ten micrometres. A few attempts were made to measure the concentration of Gd in sample A at the fibre cross-section. Gd can be identified at several points in the core area of the fibre samples, whereas recording its distribution along the radial direction is not available. This is also because the diffracted X-ray is collected at an angle with respect to the

incident electron beam, which hereby assumes a homogenous distribution within the whole scan volume. The weak signal from the small core area of the fibre sample did not provide reliable information on the dopant distribution. Therefore, the dopant concentrations were taken at different radial positions of disks cut from fibre preforms with relatively large core diameters of 0.7-0.8 mm.

The preform samples, with diameters in the order of millimetres and the slow variation in Gd concentration along the radial direction, can be treated as homogeneous. The EDX system was calibrated using a standard cobalt sample before the measurement and about every two to three hours during the measurement. The accuracy and reliability of the measurement were ensured by (i) checking the un-normalised total weight per cent, which was within an acceptable range of 100% ± 3% and by (ii) the ratio among elements that followed the chemical formulas (i.e. $P_2O_5$, $SIO_2$, and $Gd_2O_3$). The error (wt.% σ) directly provided by the software is also considered.

In the preform disk of the phosphosilicate sample (ample A), as shown in Figure 4.5, the concentration of Gd reaches its maximum, greater than 1.6 weight%, at a position 200 μm away from the preform centre. The decreased concentration level at the centre was attributed to the evaporation of $P_2O_5$ during the consolidation process, which also took Gd. The precision improved by increasing the sampling periods was limited by the low dopant concentrations. The errors worked out by Oxford INCA EDS software for P and Gd are 1.7% and 7.6%, respectively, at high concentrations. Although data at low concentrations are usually treated as unreliable information, both curves represent the refractive index profile of the fibre sample. With the help of relative atomic masses, the average atomic percentages of Gd and P across the preform core cross-section—which are required for evaluating the absorption cross section in the following chapters—turn out to be 0.117 atomic% and 2.33 atomic%, respectively.
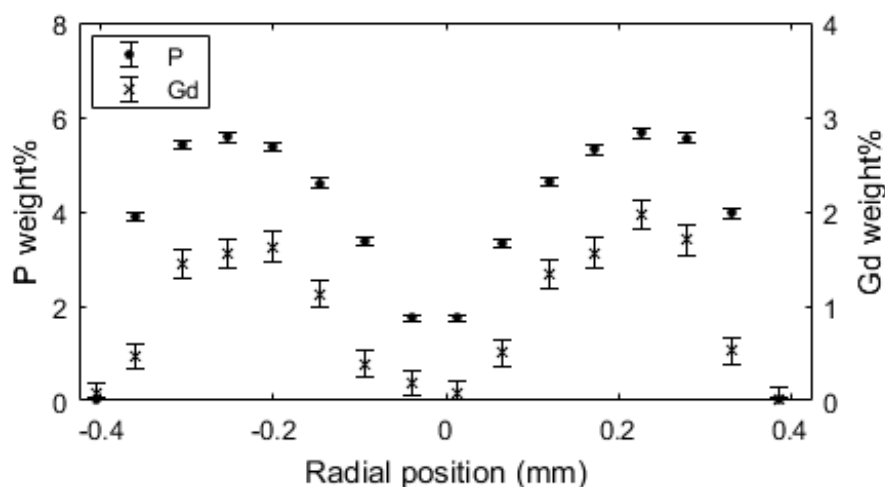


Figure 4.5 EDX results showing the concentrations of Gd and P at different radial positions within the core area of doped phosphosilicate sample A preform disk.

In the phosphosilicate preform disk sample C, as shown in Figure 4.6, the errors in the results of Gd are larger than that in sample A, due to the low concentration. The errors worked out by Oxford INCA EDS software for P and Gd are 1.5% and 12.0%, respectively, at high concentrations. The average atomic percentages of P and Gd across the preform core cross-section turn out to be 0.266 atomic% and 0.052 atomic%. Neither F in the cladding nor its diffusion into the core was detected due to its low weight percentage.
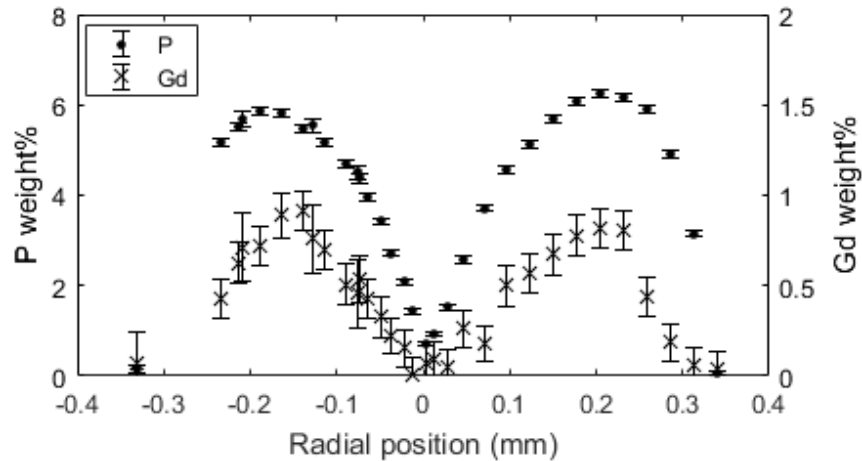


Figure 4.6 EDX results showing the concentrations of Gd and P at different radial positions within the core area of doped phosphosilicate preform disk sample C.

### 4.2.3 Analysis

The linear dopant-concentration-dependent refractive index changes of silica reported in the literature are $8.5 \times 10^{-4}$ per mol% and $67 \times 10^{-4}$ per mol% for $P_2O_5$ and rare-earth oxides, respectively [99]. However, the refractive index also varies with other factors, such as impurities and defects. Therefore, silica fibre cores and claddings fabricated using different methods may not match this rule. In particular, some elements (e.g. F) tend to diffuse [81,101,102] at high temperatures, which further changes the refractive index profile. For example, in sample B, with the help of the coefficients in the chemical formulas of silica and gadolinium oxide, the Gd concentration of 1000 ppm corresponds to $SiO_2$ and $Gd_2O_3$ concentrations of 99.85 mol% and 0.15 mol%, respectively, which suggests a Gd-induced increase in the refractive index of 0.001 in theory, while the total refractive index contrast of ~0.0013 in Figure 4.3 is attributed to both the Gd in the core and the F in the cladding tube. The latter is also claimed to depress the refractive index by around 0.001 [103].

Similarly, in sample C, the Δn arises from not only the Gd and P in the core but also the F in the cladding. The refractive index of the preform and the dopant distribution in the disk show the same profile, while the Δn in the fibre is smaller than that in the preform, as the diffusion could occur during both the preform fabrication and fibre-pulling processes. The Δn worked out from the

average Gd and P concentrations is 0.0041; with the effect of F, the exact value in the fibre is around 0.007 in Figure 4.4. Note that the disk is smaller than that indicated by Figure 4.4b, as it was cut from the fibre-pulling end. Because the disk and fibre are from the same region of the preform, the Gd concentrations in them are assumed to be the same for the following theoretical work in this report. Additionally, although the results in Figure 4.4b imply variations in the dopant concentration and Δn along the preform sample length, the variation in fibre samples is slow; multi-kilometres-long fibre can be pulled from a short preform with small variations, following the law of mass conservation. The slow variation was checked by measuring the cut-off wavelength of the fibre samples. According to the relationship between the V parameter and the NA of a fibre, the Δn ~ 0.001 results in an evident change in the cut-off wavelength. In the experiment, the results within samples several tens of metres long employed in this study were consistent with each other.

In sample A, the average concentrations of Gd and P correspond to $Gd_2O_3$ and $P_2O_5$ concentrations of 0.19 atomic% and 3.67 atomic%, respectively, in the silica host, which then result in a refractive index modification of 0.0044. This is comparable with the average refractive index modification in Figure 4.2. The cladding tube was made using the CVD method but was purchased from a different producer. Unlike the sample C, the difference between sample A preform and fibre could also because the disk sample A was cut after the fibre fabrication and from a different position on the preform with respect to where the fibre had been pulled. During the deposition of the porous core layer using the MCVD technique, the layer thickness, pore sizes, and porosity depend on the temperature and gas phases. Uneven tube heating changes these parameters along the length of the preform, which also leads to non-uniform dopant concentrations in the subsequent solution doping process [104] and consequently the refractive index. If the rule of concentration-dependent Δn in the literature applies, based on the ratio of the theoretical to the real Δn, the Gd concentration in the fibre could be above 0.14 atomic%, provided that the ratio of P to Gd is maintained within this region, which may not be the case.

## 4.3 Absorption characterisation

### 4.3.1 Experiment setup

The absorption characterisation was first carried out using a broadband lamp (BDS130, BWTEK). The output power in the UV measured with a high sensitivity thermal sensor (3A, Ophir) set after the output port (SMA 905) was 2.03±0.02 mW. It should be noted that the SMA 905 port features a diameter of 3.2 mm, which is far larger than the core diameters of the fibre samples, and the output from the lamp is divergent. Due to the modal mismatch between the fibre and output light, the exact amount of power coupled into the fibre was not accessible, as the output power was too

weak to be detected by wavelength-insensitive thermal detectors. Moreover, the power spectral density is low. This light source cannot give rise to population inversion; it was primarily applicable for loss measurement.

The output from the fibre samples was collected using a spectrometer (USB4000, Ocean Optics) equipped with a 25 μm slit, and the software for data acquisition was set to record the averaged result to reduce the noise level. Most of the results presented here were averaged over five to ten samplings. A dark spectrum was taken at the beginning of each characterisation and was subtracted from the results automatically by the software. As indicated on its datasheet, the sensitivities of the USB4000 series at 400 and 600 nm are up to 130 and 60 photons/count, respectively, which helps to conceptualise the power levels. The resolution (full width at half maximum (FWHM)) calculated from its slit size and spectral range is 0.37 nm. The integration time for each sampling was decided by the intensity of the signal and the measuring range of the device, so comparisons in terms of intensity among different groups of results are not recommended.

### 4.3.2     Absorption in fibre samples

In sample A, because of its refractive index profile and relatively low NA of 0.13 in comparison to that of the light source NA of 0.22, most of the input power was coupled into and propagated in the cladding. Although the UV curing polymer coating to some extent enhanced the losses of cladding modes, the absorptions in the core, especially by Gd ions, could not be observed clearly in the output spectra, even when the integration time was increased and when the signal from the cladding saturated the spectrometer. Therefore, fibres that did not support cladding modes were then considered power delivery fibres to couple the light through their cores into the core of sample A. Because the commonly used telecom fibre SMF-28 is not transparent in the UV due to its Ge dopant, a submarine fibre (Z fibre, Sumitomo Electric) and a solarisation-resistant fibre (UV 10/125 A, CeramOptec) with pure silica cores, fluorine-doped claddings, and high-index coating were obtained. Figure 4.7 shows the output spectral profiles of the UV fibre and the Z fibre.

It has been noticed that the UV fibre has an outer pure silica cladding outside the first F-doped cladding; however, the latter has a diameter of 20 μm, which is enough to confine the light in the core. The output from this fibre suggests excellent transmission in the UV, as the output spectrum (Figure 4.7, red curve) collected by a spectrometer has the same profile as that of a signal free-space collected without a fibre. Regarding the Z fibre, the result (Figure 4.7, black curve) suggests that it has narrow absorption band at λ ~ 250 nm, which is associated with oxygen deficient centres (ODCs) in the silica host [105]. Therefore, the UV fibre is preferred for power delivery in the sample propagation loss characterisation.
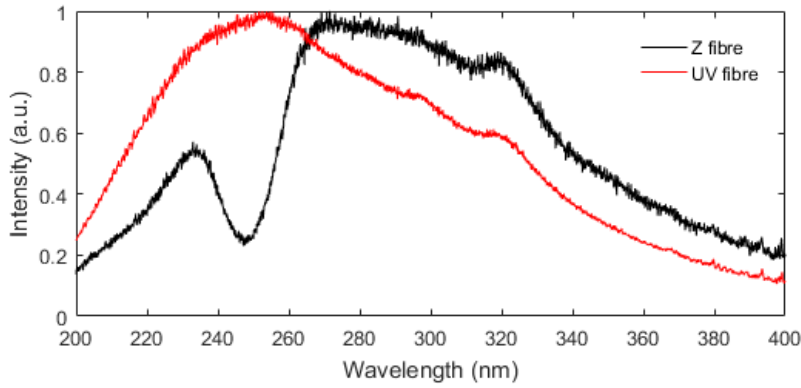
Figure 4.7 Output spectra profiles of UV fibre and Z fibre, normalised with their respective peak values.

Figure 4.8 shows the experimental setup for the sample absorption characterisations. Because of a mismatch in the core diameters of the power delivery fibres and the samples, to completely remove the power coupled into the cladding, a graphite-coated loop was made at the beginning of the sample close to the splicing point. This was performed by replacing a ~10 cm-long polymer coating with a graphite adhesive (Alfa Aesar), which has a high loss within a broad spectral band. Then, this section was bent to improve the overlap between cladding modes and the graphite coating. The loop radius was reduced until the intensity of the real-time output spectrum no longer changed with the radius, and then the loop was fixed with tape. The lengths of the power delivery fibre (UV fibre), the Gd-doped fibre sample including the graphite part, and the graphite-coated section were 10 cm, 17 cm, and 8 cm, respectively.
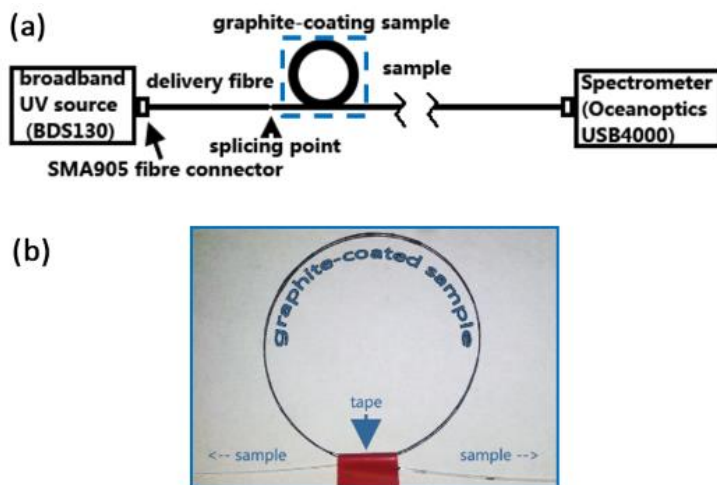


Figure 4.8: (a) The experimental setup for the Gd absorption wavelength and fibre propagation loss characterisations. Light from a broadband source was delivered to the Gd-doped core using a power delivery fibre. A spectrometer was used for light collection and analysis. (b) A photograph of the graphite-coated fibre loop made to remove the light in the cladding.

Figure 4.9 shows the output spectrum from the sample normalised to that from the UV fibre and the maximum value. The dips at $\lambda \approx$ 244.8 nm, 247.1 nm, 253.2 nm, 273.4-274.6 nm, 276.4 nm,

279.4 nm, 301.4 nm, 306.3 nm and 311.9 nm are all attributed to $Gd^{3+}$ ions and associated with transitions from the ground level $^8S_{7/2}$ to $^6D_J$, $^6I_J$, and $^6P_J$ levels. They are in agreement with the energy levels that are reported in the literature [88,89] and summarised in Table 4.1. Besides the spectrometer resolution, the tiny differences can also be related to the local environment of $Gd^{3+}$. It is well known that, in rare-earth ions, the 4f electronic states are screened by the outer $5s^2$ and $5p^6$ electron shells; hence, the positions of the absorption and emission spectral lines are weakly affected by the host environment.
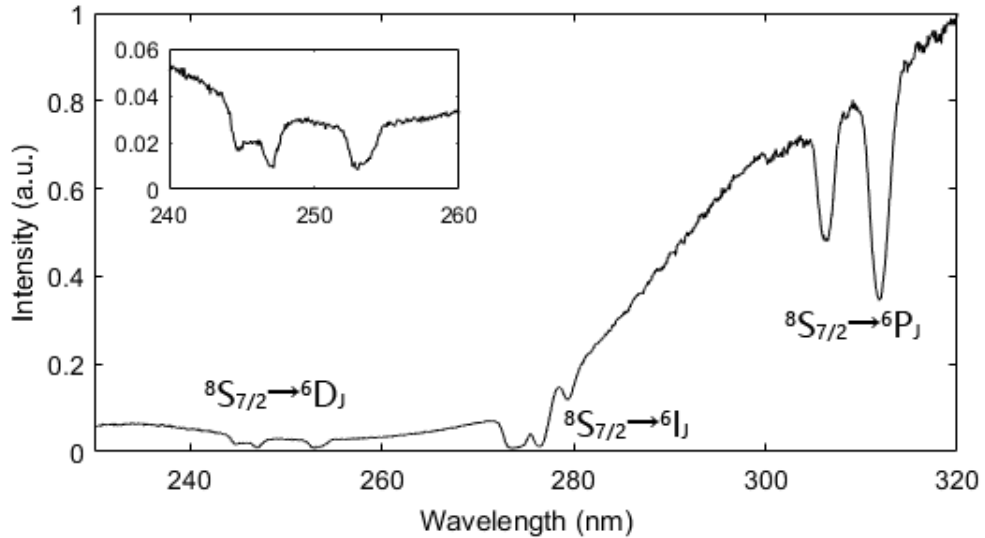


Figure 4.9: The output spectrum of fibre sample A.

Table 4.1 The $Gd^{3+}$ absorption lines compared to the data extracted from the literature [88,89].

| Energy level | Wavelength (nm) | |
| --- | --- | --- |
| | Literature | Experiment |
| $^6D_J$ | 245.4 ~ 246.0 | 244.8 |
| | | 247.1 |
| | 252.2 | 253.2 |
| $^6I_J$ | 272.4 | 273.4 ~ 274.6 |
| | 273.7 | |
| | 275.5 | 276.4 |
| | 278.4 | 279.4 |
| $^6P_J$ | 300.2 | 301.4 |
| | 304.6 | 306.3 |
| | 310.5 | 311.9 |

The transmission decreases rapidly with wavelengths at $\lambda < 300$ nm. Besides the broad absorption band centred at $\lambda \approx 250$ nm, which is attributed to ODCs in the silica, this decrease could be attributed to the absorption associated with other defects [106] and the bandgap of the phosphosilicate glass [107].

A similar result can also be obtained from the phosphosilicate fibre sample C. On the contrary, with silica sample B manufactured from the sol-gel bulk, no output was observed within the spectral range of the spectrometer using the same settings. Considering that (i) when the integration time was increased to above 10 s, only a weak signal at $\lambda > 350$ nm output was observed, that (ii) there was output when the polymer coating was removed to check the transmitted light from the cladding, and that (iii) a step-index profile has been confirmed in Section 4.2.1, the huge loss could be related to unidentified impurities or scattering from the core. A brief investigation on the sol-gel samples is provided in Section 4.3.4.

### 4.3.3 Propagation loss

#### 4.3.3.1 Cut-back measurement using a lamp

The propagation loss of the fibre was then measured using the cut-back method introduced in Section 2.5.1. Figure 4.10 shows the result from sample A. This measurement helps to estimate the length of the fibre needed to make the fibre laser under specific pump power regarding gain saturation and reabsorption at the lasing wavelength in future work. Nevertheless, the $Gd^{3+}$ absorption peaks at wavelengths below 280 nm in sample A could be observed only in short fibres. In samples longer than ~20 cm, as indicated in Figure 4.9, the background absorption took almost all the power, and the absorption at Gd-related wavelengths was saturated. However, the minimal sample length was limited by the length of the fibre adaptor at the output end and by the graphite-coated loop. Therefore, characterisation of the propagation loss in sample A at short wavelengths was not available with this setup.
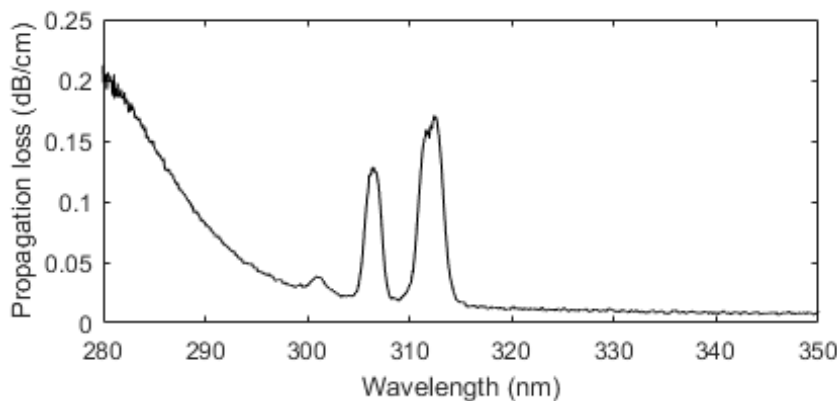


Figure 4.10 Propagation loss in phosphosilicate fibre sample A.

Moreover, Section 4.2 has introduced the relationship between dopant concentrations and refractive index modifications. They are also related to the well-known Rayleigh scattering that occurs for a particle size (or in media the local density fluctuation scale) smaller than the

wavelength. It results in non-zero imaginary components of the refractive indexes (i.e. losses) in inhomogeneous media. Rayleigh scattering in doped silica glass varies with dopant types and concentrations. In F-doped silica glass prepared by vapour-phase axial deposition, at $\lambda$ = 488 nm, the Rayleigh scattering coefficient increases linearly with the dopant concentration, as the concentration fluctuation increases [82]. In silica glass co-doped with low levels of F and $GeO_2$, the Rayleigh scattering coefficients increase linearly and parabolically with the index changes induced by the concentration of $GeO_2$ and F, respectively [108]. Rayleigh scattering can also be modified by thermal treatment, which modifies dopant distributions and the order of the silica glass network [109]. In $P_2O_5$ and F co-doped silica glass, the Rayleigh scattering in the IR can be less than it is in the pure silica at certain dopant concentrations [110]. The intensity of scattered light is inversely proportional to $\lambda^4$ [111], implying a higher loss at shorter wavelengths in the UV.

The absorption at $\lambda$ = 312.5 nm is 0.0355 $cm^{-1}$, which, with the concentration of 2.2 $g/cm^3$ measured before and the density of fused silica, leads to an absorption cross section of 1.07 x $10^{-21}$ $cm^2$. However, this result is not precise for three reasons. First, the output at the longest Gd-related wavelength consists of both the input residue and photoluminescence emission. Second, as mentioned in Section 4.2.3, the Gd concentration in the fibre sample used here is different from that in the disk. Third, the error in this cut-back measurement result is larger than that of Z fibre.

During the measurement, the UV fibre and the graphite-coated sample loop were taped down on the experiment bench to ensure a constant input power, and at the output end the fibre connector was optimised for each measurement to maximise the signal and thus minimise the measurement error induced by possible misalignment between the fibre core and the narrow spectrometer slit. Nevertheless, when the results at Gd-related wavelengths were investigated, as shown in Figure 4.11a, the results do not show linear tendencies, with some data points deviating from the fitting curve by unacceptable amounts. In particular, the fitting for $\lambda$ = 312 nm does not pass through the origin. The fittings suggest that the losses at $\lambda$ = 312 nm, 306.5 nm and 301 nm are 0.162 ± 0.044 dB/cm, 0.128 ± 0.024 dB/cm and 0.037 ± 0.008 dB/cm, respectively. The errors are given by 95% confidence bounds. Therefore, to confirm the stability and reliability of the setup, the propagation loss in the Z fibre was characterised as a reference. The result at $\lambda$ = 250 nm is given in Figure 4.11b. This wavelength was chosen because of the high loss induced by the ODC defect, which reduces the amount of fibre required. The loss given by a linear fitting is 0.205±0.009 dB/cm. The error is much smaller than that in the phosphosilicate fibre sample. Then, a second measurement was performed on sample A, which provided the following results: 0.150 ± 0.043 dB/cm, 0.101 ± 0.017 dB/cm and 0.027 ± 0.004 dB/cm at $\lambda$ = 312 nm, 306.5 nm and 301 nm, respectively. The large error implies that the transmission might be inconspicuously changing with time during the measurement.
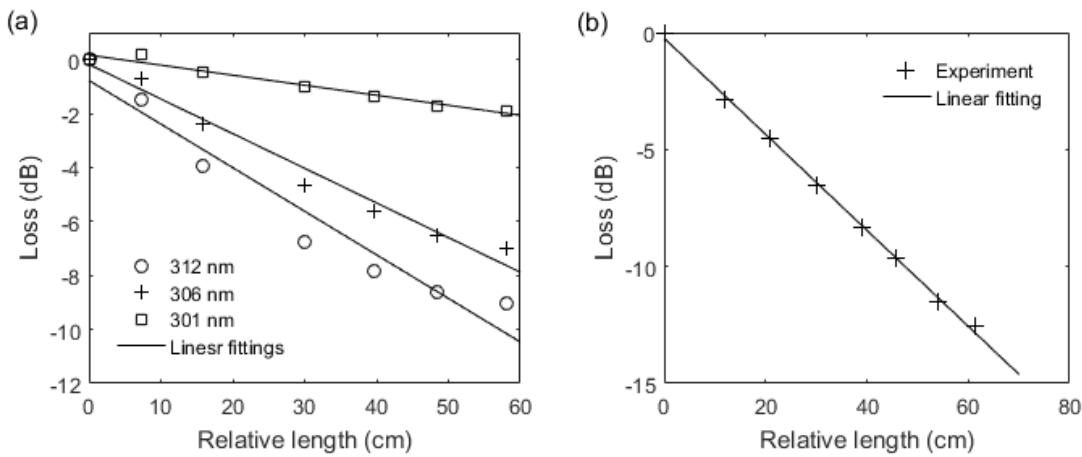
Figure 4.11: Propagation losses (a) at three different absorption wavelengths of $Gd^{3+}$ ions in phosphosilicate fibre sample A and (b) at 250 nm in the Z fibre, characterised via the cut-back method.

### 4.3.3.2    Photodarkening

Further investigation into the measurement error confirms the photodarkening phenomenon. Figure 4.12 shows the transmission spectra from a 60-cm-long fibre sample A after different exposure times. The output decreased by half after one hour. The same phenomenon was also observed in sample C, where it was more severe and evident and hindered the cut-back measurement.
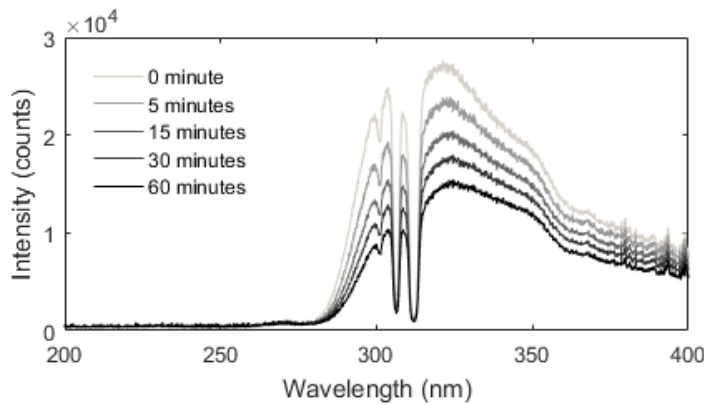


Figure 4.12: Photodarkening phenomenon in the Gd-doped phosphosilicate fibre sample A.

Characterisations of this time-dependent effect were then carried out on a 60-cm-long Z fibre, UV fibre, and Gd-doped samples. The measurements of Gd-doped samples were performed without a power delivery fibre and, in the case of sample A, with a graphite-coated loop. The photodarkening depends on intensity. Although the UV and Z fibres have relatively large cores, it is reasonable to assume that the light source intensity within the micro-core area is constant. The NAs of the Z fibre and the samples are around 0.13 to 0.135, whereas the NA of the UV fibre is ~0.155, which implies a relatively high intensity in the latter. However, this does not affect the results because no obvious photodarkening was observed in this UV fibre and Z fibre, as illustrated in Figure 4.13, which

explains the difference in the errors of the cut-back measurement results between the Z fibre and the samples.
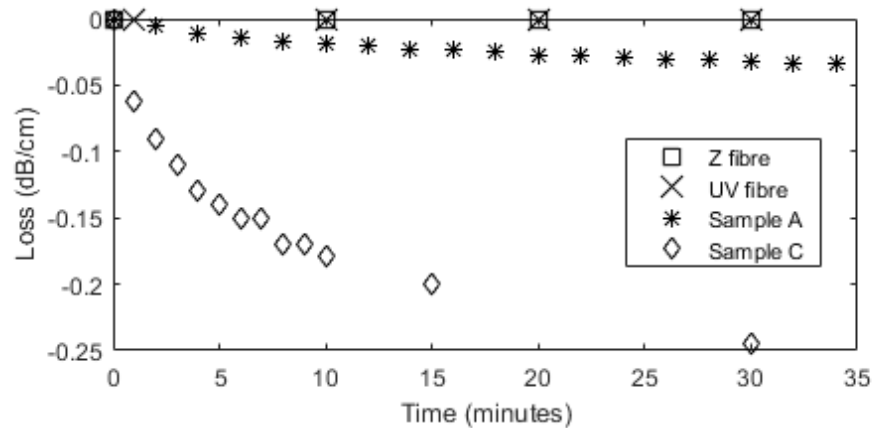


Figure 4.13: Characterisations of photodarkening effect in the Z fibre, UV fibre, and Gd samples.

The photodarkening effect is mostly related to defects [112] that absorb light within a certain spectral range. Silica-related defects are further investigated in Section 5.2. The photodarkening phenomenon varies with optical parameters, such as incident wavelengths and light intensity, and with the local structures of host materials and dopants. In fluorine-doped silica fibres at an excitation wavelength of 193 nm, this effect can be suppressed with hydrogen impregnation [113]. In germanium doped silica fibre at 480 nm, two-photon absorption can lead to this effect by breaking Si-Ge and Ge-Ge bonds [114]. The absorption increases with time (in Figure 4.13) implies the formation of new defects in the samples exposed to UV light. This could be caused by a bandgap shift induced by dopants, the short-wavelength components of the excitation light source (down to $\lambda \sim 190$ nm), and/or light interaction with pre-existing defects, which results in local structure modification and forming new defects [75]. Theoretical analyses on the exact reasons for this deterioration would require material study and information on the Gd-O-Si bond, for instance, and could be considered in the future.

### 4.3.3.3    Cut-back measurement using a light-emitting diode

Because the output from the lamp source contains short-wavelength components below the phosphosilicate bandgap, which can deteriorate the photodarkening issue, a narrow-band light-emitting diode (LED) with the emission band centred at 274 nm and a linewidth of ~5 nm is worth being investigated for the characterisation of the absorption associated with the $^8S_{7/2} \rightarrow {}^6I_J$ transition. The most powerful deep-UV LED commercially available at $\lambda \approx 275$ nm has been claimed to provide an output of up to 30 mW (SS35DF227513, SETi) (by February 2016). As shown in Figure 4.14a, the LED was mounted at the centre of a black 'star' pad which was thermal-conductively pasted to a metallic holder as a heat sink for power dissipation of 3.2 W, and two wires were

51

soldered to the contacts (by Trevor Austin at the ORC). The output spectra (Figure 4.14b) of the LED suggests that the central wavelength in practice was 282 nm with a linewidth of 12.5 nm when the temperature had been stabilised after warming up.
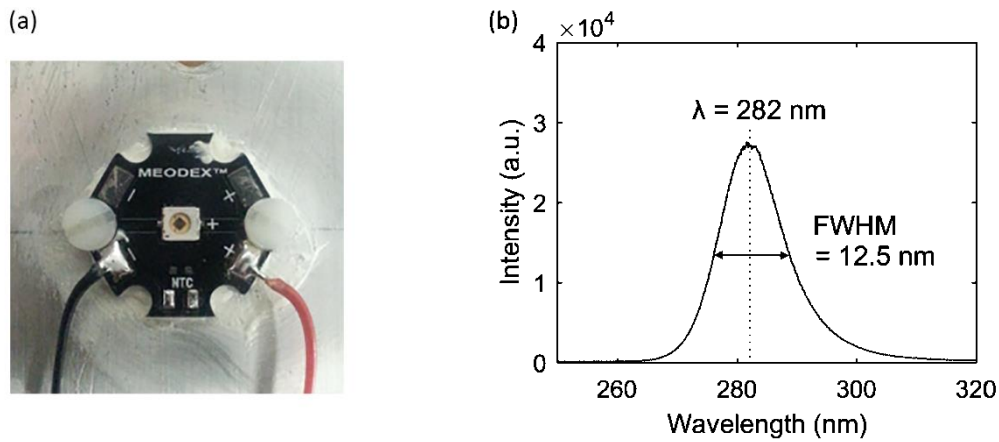


Figure 4.14 (a) A photograph of the LED mounted on a black 'star pad', which is thermal-conductively pasted to a metallic holder, and (b) its output spectrum.

A typical radiant diagram of this product indicates a half-angle of divergence of approximately 60°, corresponding to a NA of 0.87. Due to the large mismatch in the NAs between the LED and the fibre samples, coupling most of the power into the fibre is extremely challenging. Butt-coupling by setting a cleaved Z fibre sample directly on the surface of the LED leads to an output power around 30 nW with an input power of 15 mW. However, in the case of the lamp, although the exact power in the wideband is not detectable using a thermal detector, the geometrical loss caused by the mismatch in the area of the fibre core and the source output port has suggested an input coupling lower than 20 nW; yet, this has not considered the mismatch in NAs. Therefore, both the spectral density and the total input power from the LED are higher than that in the previous experiment.

With a relatively more severe photodarkening issue, sample C was then examined with the output spectra recorded at different times. The results in Figure 4.15 suggest that the effect of the UV radiation from the LED on the fibre transmission is negligible. This also confirms that the photodarkening induced by the lamp in the previous section was affected more by short-wavelength components related to the defects and the host material bandgap than by the Gd-related wavelength above 270 nm.

Since the concentration measured in this sample is more reliable than that in sample A, the cut-back measurement was then performed using the same setup to estimate the absorption cross section at this potential pump wavelength. The propagation loss at $\lambda$ = 274.3 nm, as plotted in Figure 4.16, is 0.310 ± 0.020 dB/cm, and the Gd-induced loss is around 0.22 dB/cm.
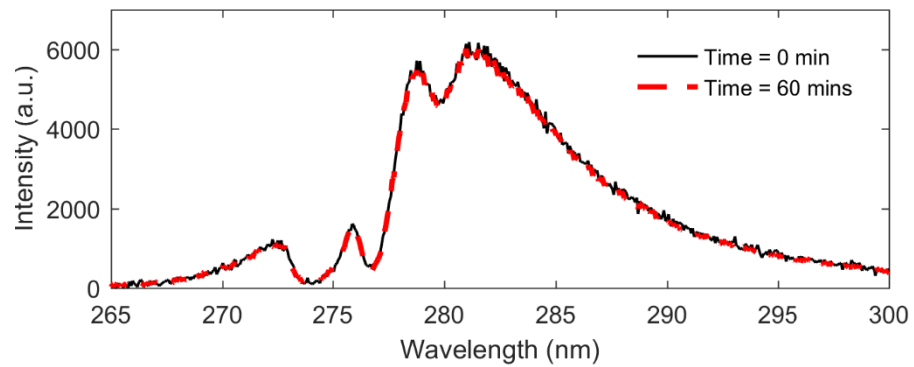
Figure 4.15 Output spectra from a 60-cm-long fibre sample C recorded before and after one hour of exposure to UV radiation from the LED.
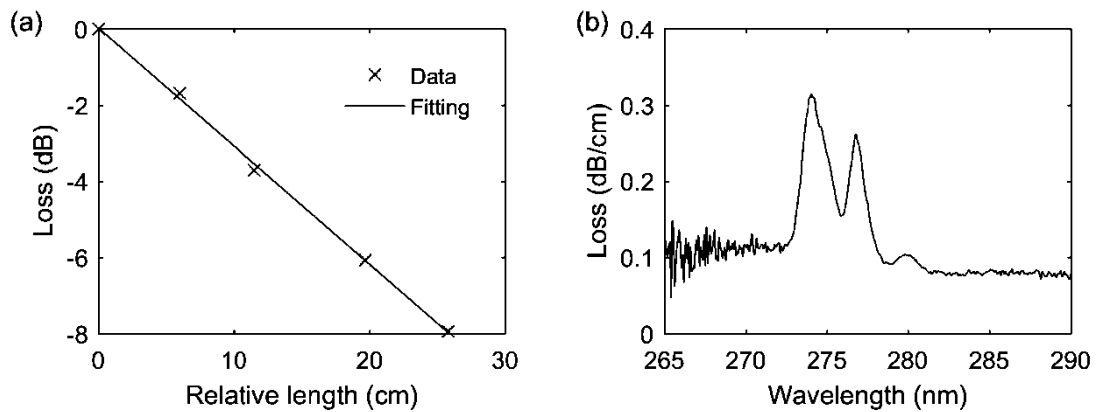


Figure 4.16 Cut-back measurement of propagation loss in sample C using an LED (a) at λ = 274 nm and (b) within the LED emission band.

With the Gd concentration of 517 ppm, the relative molecular mass of silica, and the density of the fused silica at 2.2 g/cm$^2$, the absorption cross section $\sigma_a$ is estimated to be 4.44 x 10$^{-21}$ cm$^2$, where $\sigma_a$ in the unit of area per atom is defined as $\sigma_a = \alpha/n_t$; $\alpha$ and $n_t$ are the absorption coefficient and dopant concentration, respectively. The absorption cross section is associated with an effective area in which the light is absorbed by an atom [87]. It should be noted that the exact value might be larger than the calculated value because part of the light propagates in higher-order fibre core modes that overlap with the undoped cladding. Coupled with the unknown Gd distribution in the fibre sample which, by judging from the refractive index profiles, differs from the disk, this makes it infeasible to improve the precision. Yet, the result is still comparable with that in the literature. By extracting the data from the absorption spectrum of the sol-gel silica doped with 0.5 mol% Gd [100], one can obtain an absorption cross section of approximate 4.96 x 10$^{-21}$ cm$^2$.

### 4.3.4    Sol-gel bulk sample

As mentioned in Section 4.3.3.1, although the input from the lamp was too weak to achieve population inversion, the absorption in sample A at short wavelengths related to Gd could still cause

emission at $\lambda \approx 312.5$ nm, part of which within a small propagation angle was guided in the fibre; thus, the measured value is smaller than the exact absorption at this wavelength. Alternative to the narrow-band LED, a grating-based spectrophotometer was considered to characterise the absorption, which could facilitate measurement at the absorption wavelength of the $^6P_{5/2} \rightarrow {}^8S_{7/2}$ transition that is close to the emission and thus infeasible with the LED. An attempt was made using a spectrophotometer set for bulk samples and thereby with a large spot size and low intensity. When a spatial filter was applied to collect the light transmitted from the < 1 mm-diameter cores of the phosphosilicate disk samples, the signals were submerged in background noise. An additional accessory could be considered in the future for focusing the excitation beam and for collimation.

A similar issue occurred in a 0.7-mm-diameter fibre cane of the silica sample B. Therefore, a fully-doped sol-gel bulk sample (provided by Norberto Chiodini at the University of Milano-Bicocca) was tested without the spatial filter. Figure 4.17 shows its transmission spectra.
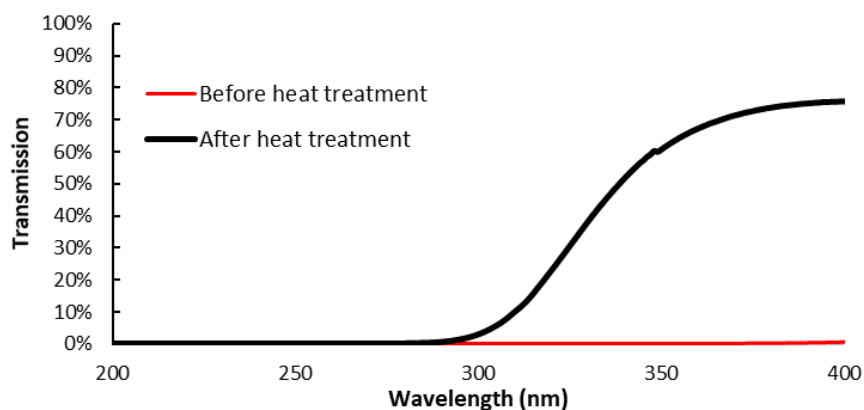


Figure 4.17 Transmission spectra of a low-concentration Gd-doped sol-gel sample taken before and after thermal treatment.

The sample was initially not transparent at wavelengths below 400 nm. After thermal treatment carried out (by Pranabesh Barua at the ORC) at temperature above 1000°C, although the transmission in the visible is improved, the sample is still opaque (Figure 4.18) in the UV. As suggested in [100] by the producer of this sample, the absorption at short wavelengths could be caused by Rayleigh scattering, because in the same type of samples no defect-related structures were observed, and because the absorption decreased with the increase in densification temperatures. In silica aerogels, the primary particles are a few nanometres in diameter; thus the Rayleigh scattering is attributed to a network of pores, although most of them are much smaller than the wavelengths. This can be controlled by changing fabrication recipe (e.g. the chemistry and pH) [115]. Another phenomenon due to Rayleigh scattering is the slightly blue reflection and red transmission, as shown in Figure 4.18b and c. The absorption could also be affected by defects, low-concentration impurities that are not detectable by the EDX, and/or crystallisation during the

annealing and cooling processes. Reducing the sample length could improve transmission, but the absorption at $\lambda \sim 312.5$ nm would not be resolvable due to the low dopant concentration. Repeating the thermal treatment with different parameters (e.g. the temperature, cooling speed and time) could improve the transmission in the future.
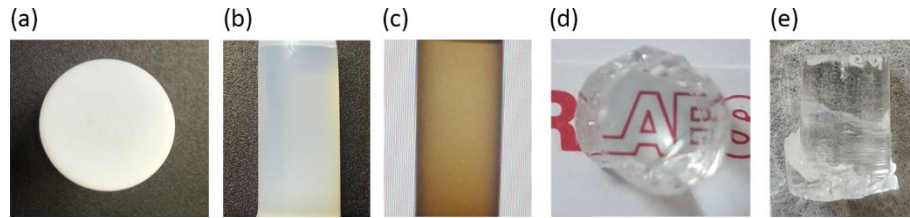


Figure 4.18 Photographs on the new sol-gel sample taken (a)-(c) before and (d)-(e) after thermal treatment.

## 4.4    Summary

In this chapter, three Gd-doped fibres are introduced. The dopant concentrations in the phosphosilicate sample A and C measured using EDX on fibre preform disks are 0.117 atomic% and 0.052 atomic%, respectively. In fibre sample A, the exact concentration might be higher than 0.14 atomic%, because the disk sample was cut from the end of the preform rather than the fibre-pulling region.

The characterisation of the fibre losses was carried out using a broadband light source. Gd-induced absorption was observed in sample A and C at the wavelengths in agreement with the energy levels in the literature. Photodarkening was observed in both samples and was more severe in sample C than sample A. This issue is supposed to be caused by the short-wavelength components from the source below the bandgap and/or be related to defects. When an LED with relatively higher spectral density and input coupling was applied instead of the lamp, the output from sample C was stable which facilitated the absorption characterisation at $\lambda = 274.3$ nm given by the ${}^8S_{7/2} \rightarrow {}^6I_J$ transition. Based on this, the absorption cross section is estimated to be $4.44 \times 10^{-21}$ cm$^2$.

There was no output from silica fibre sample B, which is surmised to be caused by a lossy core. Yet, it can still be considered for microsphere-based laser demonstration, because of the high cavity confinement and because of the microsphere fabrication carried out at high temperatures which would be accompanied by a redistribution of the dopant and reorder of the silica glass network.

# Chapter 5     Photoluminescence

This chapter reports the emission properties of $Gd^{3+}$ ions doped in silica. Due to the unavailability of a suitable pump source, UV sources available with different fixed wavelengths, including a UV LED with emission at $\lambda \approx 275$ nm, a broadband mercury-xenon lamp, and a femtosecond laser operating at $\lambda = 258$ nm were considered, followed by investigation into the defects in the silica hosts. With access to a spectrofluorometer integrated with a xenon lamp and gratings for wavelength tuning, photoluminescence (PL) and photoluminescence excitation (PLE) properties were then investigated.

## 5.1     Pumping with UV light sources

### 5.1.1     UV LED

The relatively low background absorption at $\lambda \approx 275$ nm and low loss induced by the LED reported in the previous chapter make the $^8S_{7/2} \rightarrow {}^6I_J$ transition a promising pump candidate. Compared with $^8S_{7/2} \rightarrow {}^6D_J$ transition, this transition leads to a relatively low loss from non-radiative decay between $^6I_J$ and $^6P_J$ levels. Moreover, the dense energy levels in $^6I_J$ compared with $^6P_{J=3/2,\,5/2}$ and $^6D_J$ imply the relatively efficient absorption of a pump source with a linewidth of a few nanometres, such as LEDs.

The phosphosilicate fibre sample A with a larger NA than the silica sample was first end-pumped with the same LED series that was used for the absorption characterisation in the previous chapter. The low-index polymer coating was removed due to its absorption in the UV. The resultant air coating still favours the idea of cladding pumping. Figure 5.1 shows the output spectrum from a 12-cm-long sample.
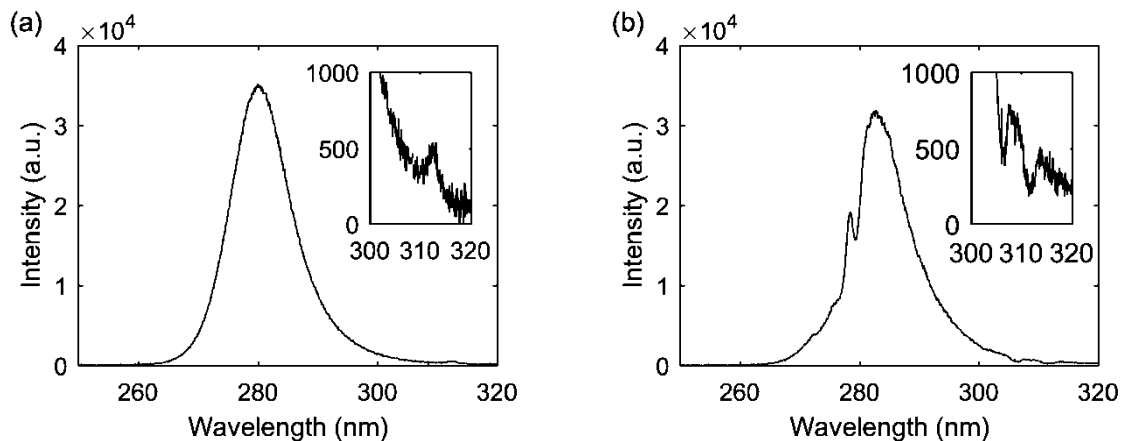


Figure 5.1 Output spectra from (a) a 12-cm-long phosphosilicate fibre sample A end-pumped with the UV LED and (b) the same sample with cladding modes removed at the output end.

A weak signal at 312 nm from $Gd^{3+}$ was observed. It should be noted that the intensity is relative since the integration time was optimised to avoid saturation at the pump wavelength. The absence of clear absorption dips at short wavelengths implies that the output mainly came from the cladding modes, which were not totally removed at the output end where the air coating was replaced with the fibre adaptor. However, removing the cladding modes by bending or applying carbon adhesive close to the end was prone to reabsorption in this region, as indicated in Figure 5.1b, confirming the cladding guidance arose from the relatively large NA. This could be solved by a side pumping scheme in which the fibre is spliced to a power delivery fibre, and the pump is set close to the splicing point. Nevertheless, there was no output with this scheme because of the low pump intensity and the short effective pump region.

Improvement in the coupling efficiency can be considered in the future for possible application of the LED in laser demonstration. The low coupling efficiency is mainly because the LED consists of a 1 mm x 1 mm LED array locating 0.8 mm beneath a 0.5-mm-thick flat fused silica window for packaging; hence, the minimal accessible spot size is large compared with fibre cores and microspheres. On the one hand, it is not feasible to set a small ball or half-ball lens with a short focal length adjacent to the array unless the glass window can be polished carefully to reduce its thickness. On the other hand, when a condensing lens (f = 45 mm) and an objective (f = 5.4 mm) were applied for collimation, most of the power was lost due to the large divergence angle and the gaps among them and the LED. An attempt was made by melting the fibre end using a $CO_2$ laser to form a spherical structure for focusing, which improved the efficiency only by half; most of the light collected was still guided into the cladding. For future work, one could consider using a lens array or customise an LED packaged with a hemispherical lens and a half-angle of divergence less than 10°.

### 5.1.2    Mercury-xenon lamp

Another potential pump transition is $^8S_{7/2} \rightarrow \, ^6P_{5/2, \, 3/2}$, for the subsequent in-band transition with a low non-radiative loss within $^6P_J$ levels, which favours a high slope efficiency. An attempt was made with a 200-W mercury-xenon lamp integrated within a Hamamatsu L9588 LightningCure light source available in the laboratory for UV curing. Its intense emission lines shown in Figure 5.1 overlap with the $Gd^{3+}$-related absorption at $\lambda$ = 302 nm and 313 nm. Since the latter is close to the expected emission wavelength, a filter with a bandwidth (FWHM) of 4 nm centred at $\lambda$ = 302 nm was applied to select the short-wavelength component, followed by an aspherical lens with a NA of 0.143 for focusing the light into the fibre samples. This scheme, however, did not work for three reasons: Firstly, the total power after the metallic output port for 1-inch lens tubes was below 5 W due to the large angle of divergence. Secondly, the output at 302 nm possessed only a small fraction

of the total power (Figure 5.2). Thirdly, although the filter was set before the lens to avoid possible damage caused by the focused intense light, the glue between the film of this filter and its glass substrate was, unfortunately, of low quality and sensitive to the UV light. As a result, the output power after the filter was significantly lower than the input and decreased fast with time (Figure 5.3). Meanwhile, the output at 313 nm from the source was not totally suppressed; a tiny peak was observed in the transmission spectrum taken with an undoped reference fibre sample, so other light sources were then considered.
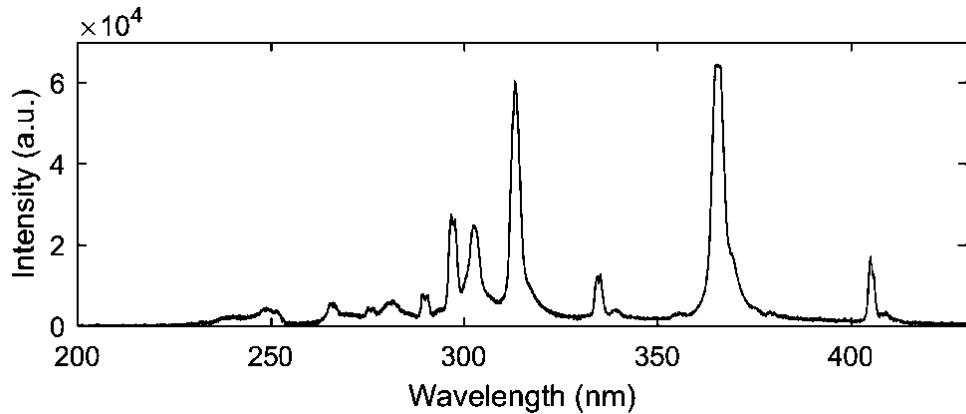


Figure 5.2 Emission spectrum of the Hamamatsu light source collected using the UV fibre.
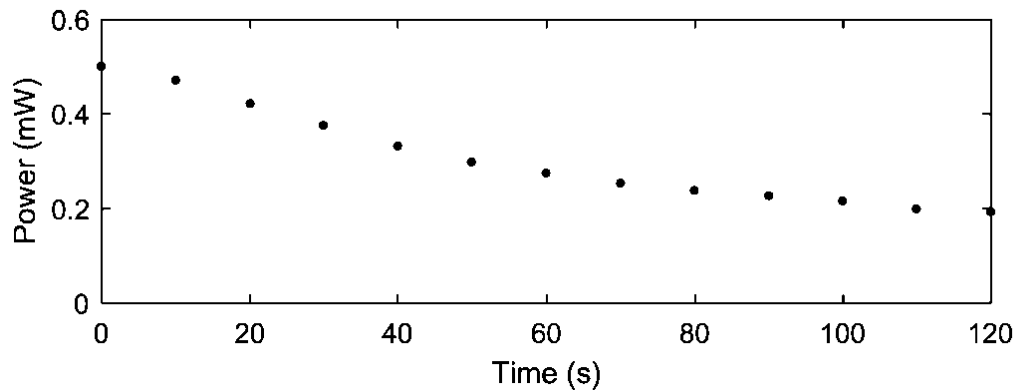


Figure 5.3 Power after the passband filter at 302 nm decreases with time, as the low-quality glue layer inside the filter is sensitive to the UV light.

### 5.1.3    Femtosecond laser

Pumping of Gd$^{3+}$ was also investigated with femtosecond pulses at $\lambda$ = 258 nm, which was generated from a solid-state femtosecond Yb:KGW laser at $\lambda$ = 1030 nm (PHAROS, Light Conversion) followed by a crystal-based fourth harmonic generator. Although this wavelength does not match the absorption wavelengths of Gd$^{3+}$ discussed in the previous chapter, PL can still be generated as a result of multi-photon absorption, which benefits from the high peak power of the pulsed laser

source. The multi-photon absorption can also lead to formation of defects in the host material, the investigation of which is discussed in Section 5.2.

### 5.1.3.1    Experiment setup

In the experiment, the pulse duration, repetition rate, and spectral FWHM of the laser at 1030 nm were 175 fs, 1 kHz, and 1.79 mm, respectively. By considering its high peak power and the sensitivity of the delicate spectrometer, a side pumping scheme was adopted. The Gd-doped fibre sample was set horizontally, and the circular laser spot was focused in the vertical direction perpendicular to the fibre using a cylindrical lens (f = 75 mm) and was focused into the fibre core from the side. The effective pump length along the fibre was the original beam waist. The relationship among the wavelength $\lambda$, beam waist $w_0$, Rayleigh length $Z_R$, and focal length f can be found in the textbook [87]: $z_R = \pi w_0^2 / \lambda$, and $w_{o2} = \lambda f / \pi w_{o1} [1 + (f/z_{R1})^2]^{1/2}$, where subscripts 1 and 2 refer to beam parameters before and after the lens, respectively. The beam waist ($1/e^2$ half-width) in the vertical direction and Rayleigh length after the lens were 4.1 µm and 205.3 µm, respectively. Collimation and alignment were performed according to the transmitted and scattering pattern after the fibre and were then optimised by maximising the real-time output signal intensity at 312 nm (i.e. the emission wavelength given by the $Gd^{3+}$ $^6P_{7/2} \rightarrow {}^8S_{7/2}$ transition).

### 5.1.3.2   Sample A

Figure 5.4 shows the output spectrum from fibre sample A. The tiny peak at 261 nm is the Stokes shift of 13.2 THz (for Raman scattering in silica) from the light source. The luminescence of $Gd^{3+}$ can be observed at 312 nm; however, it is covered by the broadband emission centred at $\lambda$ = 280 nm. This emission was also observed in a reference experiment using Z fibre (Figure 5.4b). It is ascribed to an interaction of ODC (II) with ODC (I) [116].
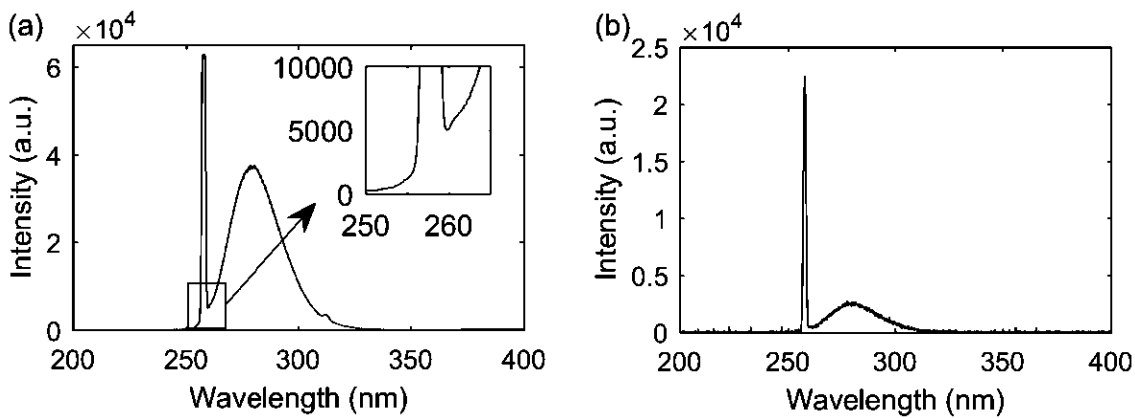


Figure 5.4 PL spectra of (a) sample A and (b) Z fibre side-pumped using the femtosecond laser.

### 5.1.3.3 Sample B

Figure 5.5 shows the results from fibre sample B. The absence of broadband emission from defects favours observations of the PL from $Gd^{3+}$ ions. Spectra were recorded at different pump power from 8.5 mW to 53 mW. Strong luminescence from $Gd^{3+}$ was observed at 315 nm with a linewidth (FWHM) of 2.95 nm. The 3 nm shift from the result of sample A is due to a host-related energy level shift. According to the pulse duration and repetition rate, the femtosecond laser peak power was 242 MW when the averaged power was 45 mW. It should be noted that, during the measurement, as the pump power increased, the high peak power modified material local structure as well as the refractive index. This was also visually observed when a fibre sample was side-pumped with the fundamental 1030 nm laser at a comparable power level and was end coupled with a fibre fault locator: changes in the scattering pattern of the latter with time implied modifications of the material. This effect with optimised laser parameters and a suitable focusing system can be applied for direct writing gratings [117]. In the present study, however, this destructive effect should be handled carefully. In the microsphere laser experiment in Chapter 7, the pump was therefore set to a suitable high level at the beginning to minimise this effect during the measurement.
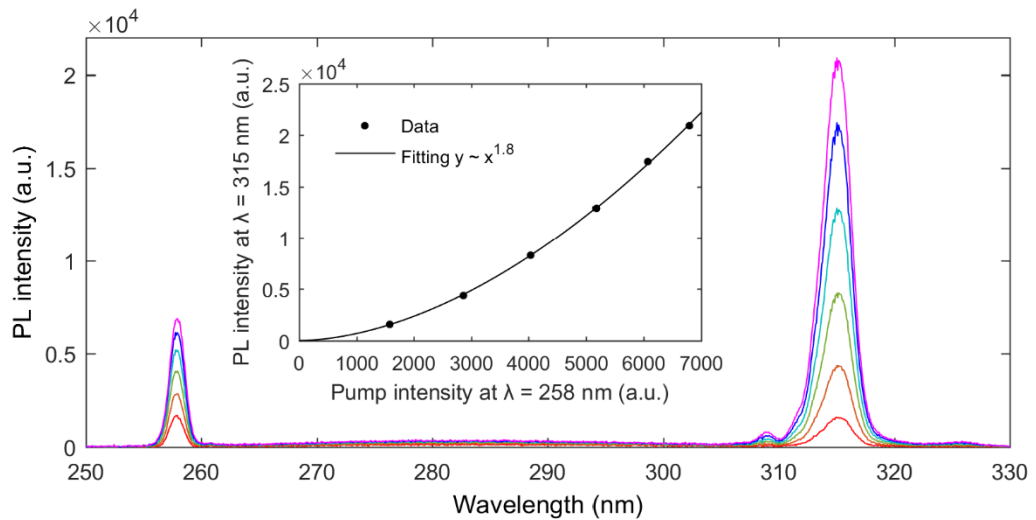


Figure 5.5 PL spectra of sample B under excitation by the femtosecond laser at $\lambda$ = 258 nm recorded at different pump power. The inset indicates the dependence of the PL peak intensity at $\lambda$ = 315 nm on the pump peak intensity.

The dependence of peak PL intensity on the pump is plotted in the inset. Since the refractive index modification led to scattering and reduced excitation coupling efficiency, instead of using the pump power recorded before the sample, the peak intensity of the signal at 258 nm in the spectra is employed as a reference. It has relatively low intensity because the beam is perpendicular to the fibre, whilst the PL at 315 nm was emitted in all directions. The scattering also increased pump longitudinal component that could be guided to the spectrometer. This effect increased with the pump power; therefore, if the emission of one photon at 315 nm was given by the absorption of

one photon at 258 nm, the slope of the curve in the inset should reduce as the pump power increases. The exact curve with a logarithm slope of 1.8 suggests that the origin of this luminescence is associated with both linear excitation and nonlinear multi-photon excitation. In the latter, absorption of multi-pump photons results in emission of only one photon at 315 nm. Because of the significantly high peak power, several nonlinear processes can occur simultaneously. For example, it can be associated with a nonlinear multi-photon absorption related to the silica bandgap or higher Gd energy levels that have not been reported in the literature, followed by single- or multi-photon emission. As for linear effects, it is worth noting that (i) although the linewidth of the pump is 1.79 nm, its tail extends to wavelengths below 256 nm and that (ii) if the 3 nm shift is applicable to other Gd absorption wavelengths, the absorption at 253.2 nm in Table 4.1 becomes 256.2 nm in sample B, which implies that a tiny fraction of the femtosecond laser might be absorbed directly by the $Gd^{3+}$, explaining the logarithm slope below 2. Furthermore, it could also be related to single-photon absorption, which leads to the excitation of a virtual level, followed by a nonradioactive decay to $^{6}P_{5/2}$.

The luminescence signal at 309 nm with a linewidth of 1.98 nm is ascribed to the $Gd^{3+}$ transition $^{6}P_{5/2}\rightarrow^{8}S_{7/2}$. Meanwhile, the luminescence at 325 nm is ascribed to the phononic replica (Raman shift) of $^{6}P_{5/2}\rightarrow^{8}S_{7/2}$ transition and is associated to the Si-O-Si fundamental vibration (1100 $cm^{-1}$), which is in agreement with the literature [100]. This shift is different from that in sample A (i.e. 13.2 THz) because the Raman spectrum of fused silica [96] typically shows several peaks corresponding to various vibration modes, and the dominant vibronic transition is determined by the Franck-Condon principle. Therefore, different glass compositions and dopant concentrations can result in a change in the relative intensity of these peaks.

Pumping with the second harmonic in the visible and the fundamental in the infrared were also considered. Luminescence was not observed with the former, which might be caused by poor alignment, as pumping with the fundamental using a grating writing set-up for focusing generated the emission from $^{6}P_{7/2}\rightarrow^{8}S_{7/2}$ transition although the signal-to-noise ratio (SNR) is poor.

### 5.1.3.4   Decay lifetime

An attempt was made to obtain information in the time domain, in particular the decay lifetime, using a photodiode detector and an oscilloscope. Three cylindrical lens were used to focus the excitation beam into the core. The first one (f = 50 mm) focused the light in the vertical direction; the resultant beam waist and Rayleigh length in the z-direction were 2.7 µm and 90 µm respectively. The other two cylindrical lens were employed to expand the beam in the horizontal direction and thus increased the length of the fibre exposed to the radiation.

However, as the pump wavelength did not well match the $Gd^{3+}$ energy levels, the fluorescence intensity in these experiments was extremely weak. According to the sensitivity of the spectrometer and the sampling integration time, the integration of the area under the peak suggests a power level in picowatts. The amplified GaP photodetector (PDA25K-EC, Thorlabs) that was available in the laboratory is sensitive to power levels down to ~1 nW; thus signal emitted from the $Gd^{3+}$ was too weak to be detected. Therefore, before a suitable pump source or amplifier is available, information in the literature is considered for theoretical work in the next chapter.

## 5.2    Defects in silica

Both the short-wavelength components from the lamp source and the high peak power of the pulse lasers caused formation of new defects in the material. With the three-cylindrical-lens setup, defects in silica were then investigated.

### 5.2.1    Common defects in the UV region

During the experiments with the femtosecond laser, it was also noted that the sample under excitation emitted red light, which was not observable at the beginning of the measurement. This indicates the formation of new defects accompanied by the refractive index modification as previously mentioned.

Various types of defects exhibit absorptions in the UV [118], and some can be directly investigated through their photoluminescence [75]. Two of the most common defects in wavelengths ranging from 200 nm to 300 nm attract particular interest due to their photoluminescence features. One is the ODC observed in both Z fibre and phosphosilicate samples, accounting for the absorption at 250 nm and the luminescence at 280 nm. The other is the non-bridging oxygen hole centre (NBOHC) that emitted red light under excitation with the femtosecond laser, which is discussed further in the following sections.

### 5.2.2    Non-bridging oxygen hole centre

In addition to ODC, the low transparency of fused silica glass compared with crystalline silica within the wavelength range of 200 to 300 nm could arise from other defects. When the Si-O bond in regular silica network or O-H bound in wet silica breaks, the resulting structure in which O has an unpaired electron is called NBOHC, noted as $\cdot O{-}Si{\equiv}$ [75]. To determine whether the red light observed in the experiments above was due to NBOHC, sample B was examined with its output spectra taken using another USB4000 spectrometer for the visible and infrared spectral range. The results presented in Figure 5.6 matches with the luminescence of NBOHC. The increase in its

intensity with time suggests that new NBOHC structures were induced by the femtosecond laser during the measurement.
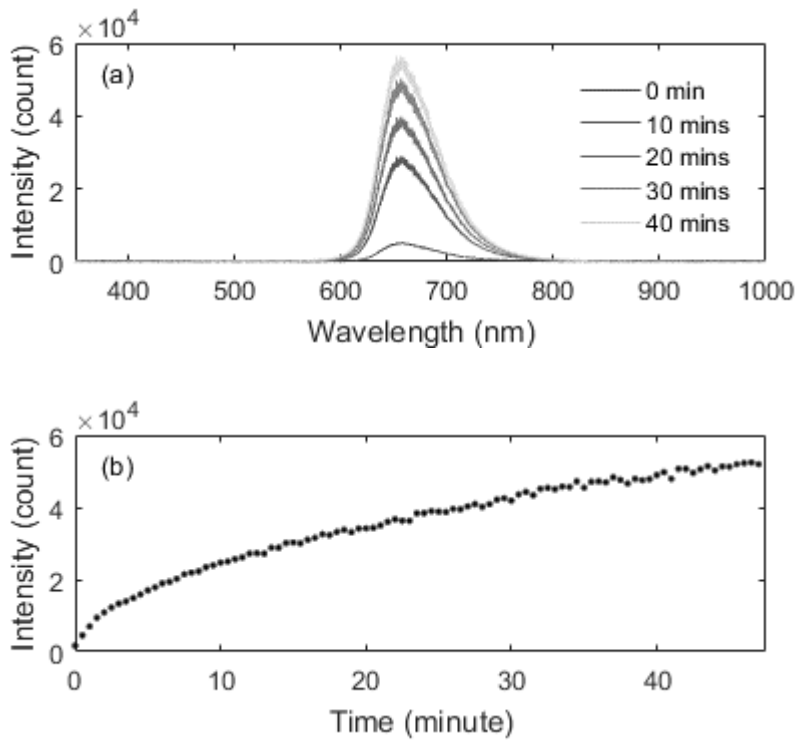


Figure 5.6 (a) Output spectra of sample B exposed to the femtosecond laser and (b) increase in the NBOHC peak emission intensity with time.

Silanol (SiOH) has absorption at 7.5-8.0 eV, and NBOHC can be formed with a $F_2$ laser (7.9 eV) via photolysis of silanol [119,120]. Here, the formation of NBOHC under femtosecond laser radiation at 258 nm (4.8 eV) is believed to be caused by multi-photon absorption. It is, therefore, recommended to use a continuous wave (CW) pump for laser demonstration to avoid decreasing pump efficiency. Improvement in the host material could also be considered.

### 5.2.3  Hydrogen loading

Research in [121] affirms that hydrogen loading can passivate the ultrafast laser-induced defects in SMF-28 and Z-fibres, except for the core of the SMF-28 where the modification threshold was reduced by the presence of Ge. To verify this passivation in Gd-doped samples, a hydrogen-loading process was conducted. A few metres of sample B was placed in a high-pressure (150 bars) chamber filled with hydrogen for three weeks at room temperature. The measurement above was then repeated. The results are shown in Figure 5.7.

A broadband emission at short wavelengths is evident. The profile implies that it might consist of more than one signal; thus, a multi-term Gaussian sum fitting is applied to separate them (see Figure 5.8). The relatively weak peak at ~650 nm is attribute to the NBOHC, while the one centred

at 560 ± 4 nm is presumed to be associated to the radiative recombination of electrons and holes separated on defect pairs ($V_O$ ; $(O_2)_i$), where $V_O$ is the oxygen vacancy, and $(O_2)_i$ is formed by two oxygen interstitials coming from two separate Si-O bonds [122].
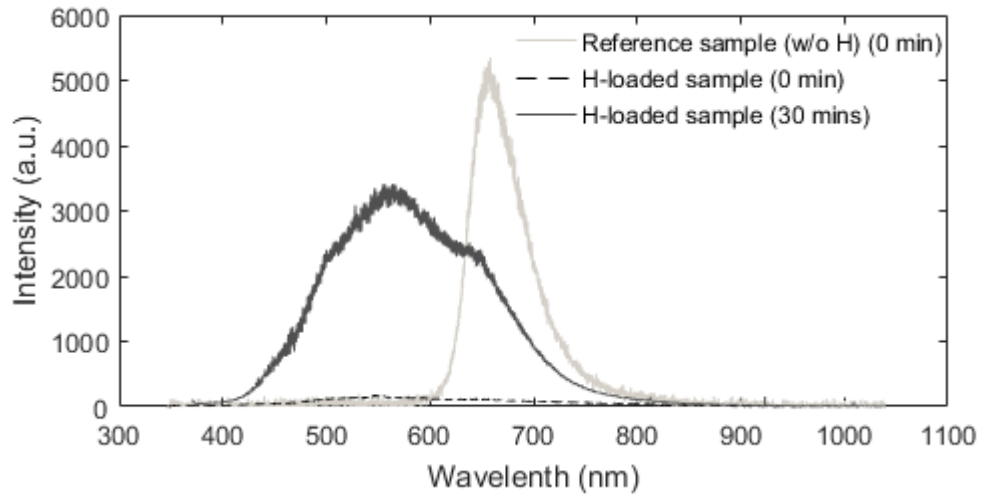


Figure 5.7 Luminescence from NBOHC in the hydrogen-loaded sample compared with the reference sample. (Data scaled according to sampling integration times for comparison)
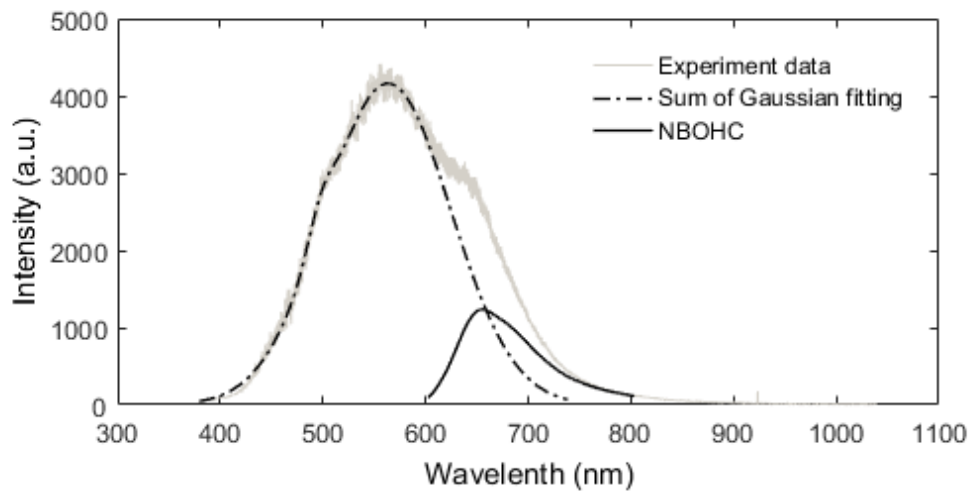


Figure 5.8 Decomposition of the luminescence spectrum recorded from the hydrogen-loaded sample exposed to femtosecond laser for 45 minutes.

Another similar process mentioned by the authors and based on a recombination of one vacancy and one oxygen interstitial—which is expected to form a weak donor-acceptor linkage with the nearest normally coordinated O atom—generated a weak signal at 468 nm. It is presumed to be the relatively 'noisy' part at the same wavelength in Figure 5.8. Note that in [122], the defects were induced by short pulses in the visible or infrared and then excited using a UV source at λ = 250 nm. Here, generation and recombination occurred simultaneously due to the high peak power of the femtosecond laser; hydrogen might act as a catalyst by forming O-H bonds, making this process

much more observable than in the original sample. The intensities of different components as a function of time are presented in Figure 5.9. The peak at 498 nm is relatively weak and tends to saturate after 45 minutes, while the luminescence intensity at 560 nm increases faster with time than the NBOHC signal.
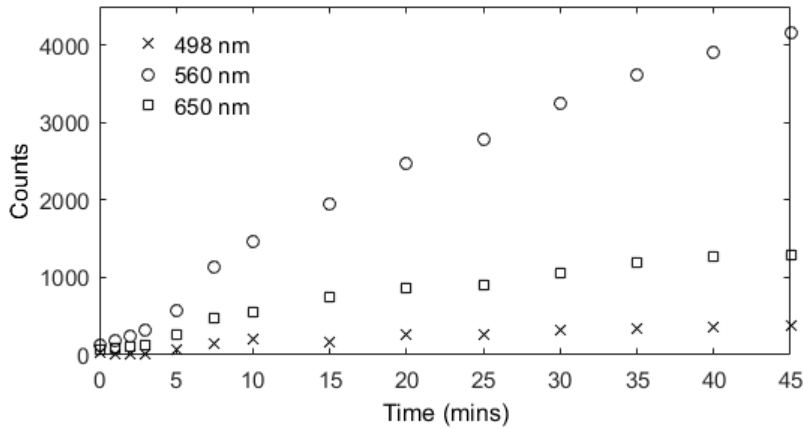


Figure 5.9 The intensities of different component peaks increase with time.

Notably, in Figure 5.8 after 30 minutes of exposure, the PL intensity of the defects in the hydrogen-loaded sample did not exceed the initial intensity recorded from unprocessed samples, suggesting that the hydrogen-loading process not only passivated the generation of new defects but also reduced the defects initially present in the samples without hydrogen loading. The fitting also facilitates a qualitative analysis of the effect of hydrogen on NBOHC. Firstly, the signal from NBOHC in the hydrogen-loaded sample is much weaker than that from the reference, and the large difference (~60 times) cannot be explained by the errors in alignment and fitting, suggesting that most of NBOHC in the sample disappeared after hydrogen loading. Secondly, the hydrogen-loading process is believed to have passivated femtosecond laser-induced NBOHCs. In both the reference samples and the annealed hydrogen-loaded sample (reported in the next section), the amount of femtosecond laser-induced defects as well as the emission intensity increased fast within the first three minutes, while this phenomenon was not observed in the hydrogen-loaded sample. The spectrum of the latter was almost unchanged within the first minute. Additionally, the change in the intensity was almost independent of the laser beam focusing position, suggesting that the defects in both core and cladding were passivated.

The results above suggest that silica doped with small amount of Gd has behaviour that is consistent with the results obtained in pure and F-doped silica in the literature, where 4,000 femtosecond-laser pulses at 800 nm did not induce NBOHC in hydrogen loaded samples [121]. Besides, in the experiment, the femtosecond laser was focused as close as possible to the core; an alignment error cannot explain the nearly two orders of magnitude difference between the hydrogen-loaded and the reference samples. Note that the laser Rayleigh length and waist were 91 μm and 2.7 μm,

respectively; thus without direct observation of the power distribution in the fibre, it is possible that the beam was focused a little more on the core in one sample than the other. Therefore, further quantitative investigations can be conducted by separating the signals from the core and cladding, for example, by adopting fluorescence microscope to analyse the cross-section or by focusing only on the core, which can be achieved, for instance, by removing the cladding using HF.

### 5.2.4    Thermal treatment after hydrogen loading

A section of sample B was placed in an oven at 200 °C for 10 hours directly after the hydrogen-loading process, followed by the same characterisation procedures. The results in Figure 5.10 reveal that the intensity of the luminescence at 652.5 nm increased by more than one order of magnitude within the first 3 minutes, suggesting that there was not enough atomic hydrogen for passivation after annealing. This is similar to the increase observed after ~5 minutes in Figure 5.9: because of the heat generated from the femtosecond laser radiation absorbed by the sample, hydrogen diffused, and its reaction with NBOHC centres became slower than the outgassing process. It has been reported in [123] that in a-SiO$_2$ the x-ray induced NBOHC and the hydrogen recombined with each other at cryogenic temperatures. Atomic hydrogen becomes mobile at temperature as low as ~30K and dimerises into molecular hydrogen at ~130 K. The latter becomes mobile at temperature above ~200 K [120].
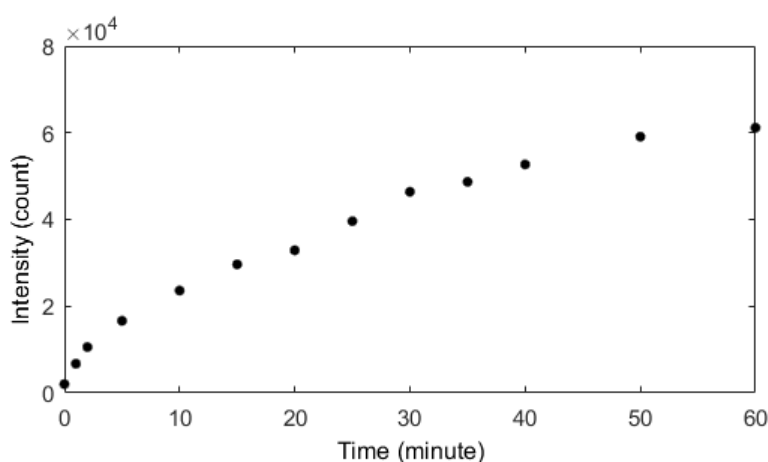


Figure 5.10 Increase in the NBOHC peak intensity with time.

## 5.3   PL and PLE spectra

Because the UV sources available either induced defects in the host material or had a poor beam quality, and also because their emission wavelengths were fixed, access to a spectrofluorometer (Horiba Fluorolog-3) equipped with a xenon excitation lamp was then acquired for 2D PL and PLE spectral mapping.

To improve the SNR and obtain a significant signal from the fibre sample, a bundle of approximately $10^3$ sample A fibres without polymer coating was assembled to form a parallelepiped with dimensions 1 cm x 1 cm x 1 mm (see Figure 5.11a). The light was incident on the fibre side that had the highest core-to-cladding aspect ratio. Both the excitation and emission slits were set to 1 nm bandpass with an estimated beam size of 1 mm x 6.5 mm at the sample surface.
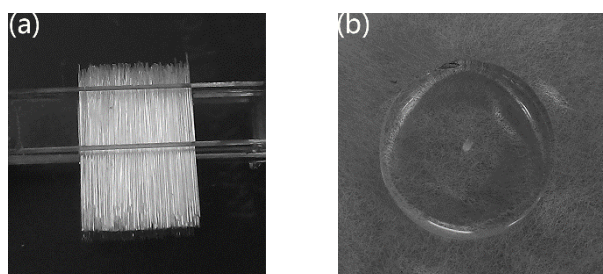


Figure 5.11 (a) Fibre bundle of phosphosilicate sample A and (b) its preform disk with a core diameter of ~0.8 mm.

The spectra were recorded at room temperature and corrected with excitation spectrum, detector spectral sensitivity, and blaze angle of emission grating. The results from the phosphosilicate fibre sample are shown in Figure 5.12.
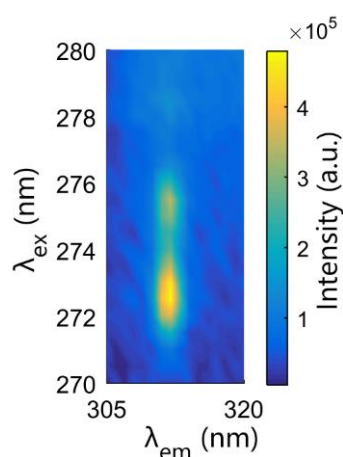


Figure 5.12 2D PL/PLE spectral mapping of the phosphosilicate fibre sample. The excitation and emission mapping steps were 0.5 nm and 1 nm, respectively.

In the spectral mapping, intense PL emission at $\lambda_{em} \approx 312$ nm, generated by the $^6P_{7/2} \rightarrow {}^8S_{7/2}$ transition, was observed under excitation at $\lambda_{ex} = 272.7$ nm and 275.4 nm (i.e. pumping into the $Gd^{3+}$ $^6I_J$ multiplet levels). The ~1 nm shift from the absorption spectrum in the previous chapter is attributed to the different calibrations of the spectrometer and the spectrofluorometer used.

As the fibre drawing process corresponds to a thermal treatment at high temperature, fibre preforms were also analysed for comparison. The disk cut from the phosphosilicate preform (Figure 5.11b) was also characterised with its cross-section polished to minimise scattering. Due to the weak excitation intensity at short wavelengths, mappings were taken on multiple sub-areas with scanning step ranging from 0.5 nm to 2 nm before combination.

Figure 5.13 shows the results from the phosphosilicate preform disk. Slit widths and peak values differ because of the increased excitation and emission slit widths used for PL and PLE signal optimisations, respectively. The wavelength ranges are limited to the data available in the system for correction based on the wavelength-dependent source power and detector sensitivity.
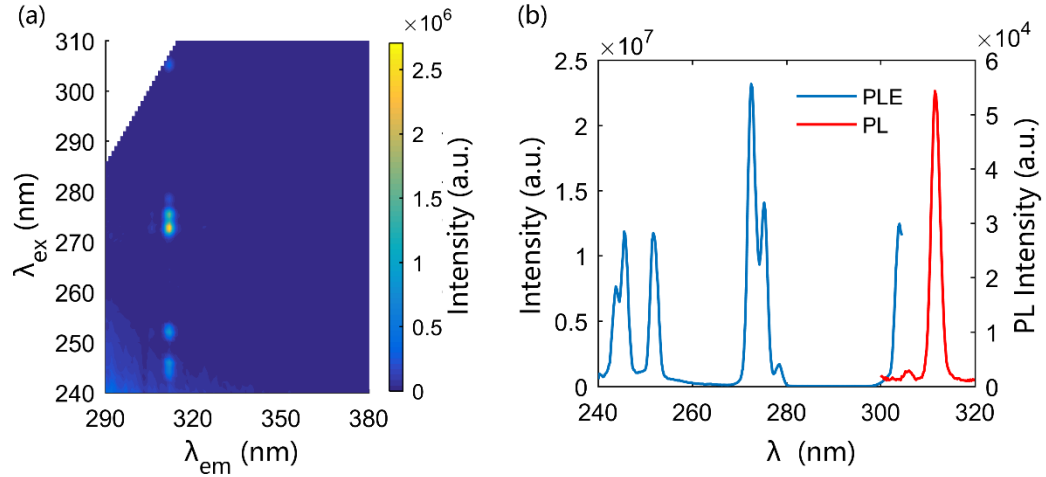


Figure 5.13 (a) 2D PL/PLE spectral mapping of the phosphosilicate preform disk. (b) PL (excitation wavelength $\lambda_{ex}$ = 272.5 nm) and PLE (emission wavelength $\lambda_{em}$ = 312 nm) spectra.

The disk sample exhibited intense emissions at $\lambda_{em}$ = 311.7 nm, attributed to the $Gd^{3+}$ $^6P_{7/2} \rightarrow$ $^8S_{7/2}$ transition, observed under excitations at $\lambda_{ex}$ = 243.7 nm, 245.7 nm, and 251.9 nm, attributed to pumping into the $^6D_J$ levels; excitations at $\lambda_{ex}$ = 272.6 nm, 275.2 nm, and 278.3 nm, attributed to pumping into the $^6I_J$ levels; and excitations at $\lambda_{ex}$ = 304.0 nm, attributed to pumping into the $^6P_{5/2}$ levels, respectively. A comparison with the results obtained for the fibre sample suggests that the emission wavelengths, and thus the energy levels of the $Gd^{3+}$ dopant, were unaffected by the fibre pulling process performed at high temperature. The $^6P_{7/2} \rightarrow$ $^8S_{7/2}$ transition, which features a spin change, is associated with an emission band having a linewidth of $\Delta\lambda$ ~ 2.5 nm (FWHM). The relatively strong emission signal at excitation of $\lambda_{ex}$ = 272.5 nm is partly attributed to the dense distribution of energy levels in the $^6I_J$ energy level group, which results in multiple lines broadened by glass host and overlapping within the bandpass 1 nm wavelength range. At this excitation, a weak emission from the $^6P_{5/2}$ energy level was also observed at $\lambda_{em}$ ~ 306 nm in the PL spectrum. Excitation to this level, followed by an inter-band, non-radiative decay to $^6P_{7/2}$, corresponds to a peak at $\lambda_{em}$ ~ 304 nm in the PLE spectrum, suggesting a Stokes shift of $\Delta\lambda$ ~ 2 nm.

The polished disk sample had a higher SNR than the fibre bundle. Although the SNR is relatively low at short excitation wavelengths, mostly due to the weak intensity of the light source below $\lambda_{ex}$ ~ 250 nm, a weak signal from ODC(II) [75] was clearly observed as a wide-band emission (see the left bottom of Figure 5.13a. Despite the wide transparency range of pure silica, various types of defects can induce loss in the UV wavelength region. The ODC is one of the most common silica defects

optically active in the UV region; it has attracted particular interest due to its photoluminescence features [75]. The excitation spectra for two characteristic emission wavelengths of the ODC(II) (i.e. $\lambda_{em}$~282 nm and $\lambda_{em}$~459 nm [105]) was verified (Figure 5.14). Their absorption band overlap with some of the transitions in $Gd^{3+}$, thus affecting pump efficiency in potential applications.
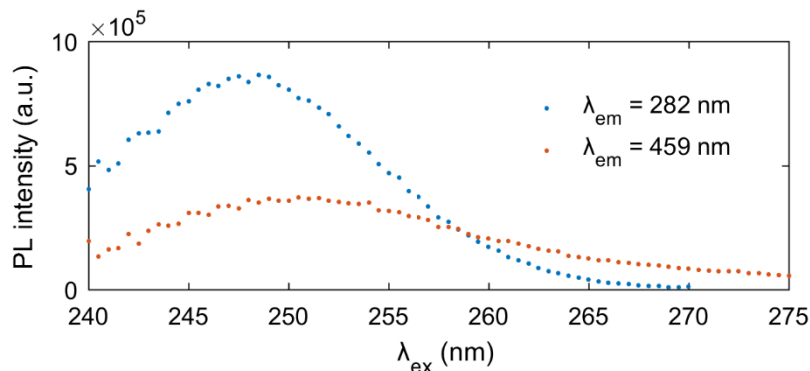


Figure 5.14 PLE spectra of ODCs at two emission wavelengths in the phosphosilicate preform sample.

The PL/PLE mapping and PL(E) spectra from the Gd-doped silica fibre sample B were recorded with a wavelength step of 0.5 nm and slit widths of 1 nm (Figure 5.15). A stack of 50 Gd-doped silica fibre canes without polymer coating was prepared to form a parallelepiped with dimensions 1 cm x 1 cm x 1 mm. Results indicate an approximately $\Delta\lambda$~1.5 nm shift in the $Gd^{3+}$ emission wavelengths with respect to the phosphosilicate sample. A weak luminescence signal at $\lambda_{em}$~325 nm, nearly $\Delta\tilde{v}$~1100 $cm^{-1}$ from $\lambda_{em}$~314 nm, matches the Raman shift associated with the Si-O-Si fundamental vibration.

Compared with the phosphosilicate sample, instead of the ODC (II) emission band, a wide-band emission at $\lambda_{em}$~390 nm previously observed in the disk sample [124] was detected here with its peak intensity reduced to about 1/18 of the peak PL intensity from $Gd^{3+}$. This wavelength is close to the $T_1 \rightarrow S_0$ transition of the Ge-ODC [125], which was previously detected in silica containing germanium (Ge) impurities at concentrations of the order of 10 ppm by weight [126]. In this preform, Ge might have been induced during preform fabrication, using the sol-gel method in the form of impurity in the silicon precursors. However, here the excitation-wavelength-dependent peak position implies a more complex explanation. Since this signal was not observed in the phosphosilicate samples, it is currently supposed to emerge from intrinsic defects of the host. The difference in intensity between $Gd^{3+}$ luminescence and this signal increased compared with that recorded in the sol-gel disk sample before the fibre-drawing process [124]. As the fibre-pulling process corresponds to a rapid thermal treatment of the sample, this phenomenon is in accordance with the enhanced Gd luminescence observed in the literature after rapid thermal treatment [95]. Moreover, the excitation peak at $\lambda_{ex}$ = 307.5 nm (to $^6P_{5/2}$ level) features a shoulder at 305.5 nm, which is different from the peak profile observed previously. This difference is similar to the host-

dependent $Er^{3+}$ $^4I_{13/2} \rightarrow {^4I_{15/2}}$ transition [21]. Both phenomena confirm that the $Gd^{3+}$ ions experience a different surrounding in the silica and phosphosilicate samples [127].
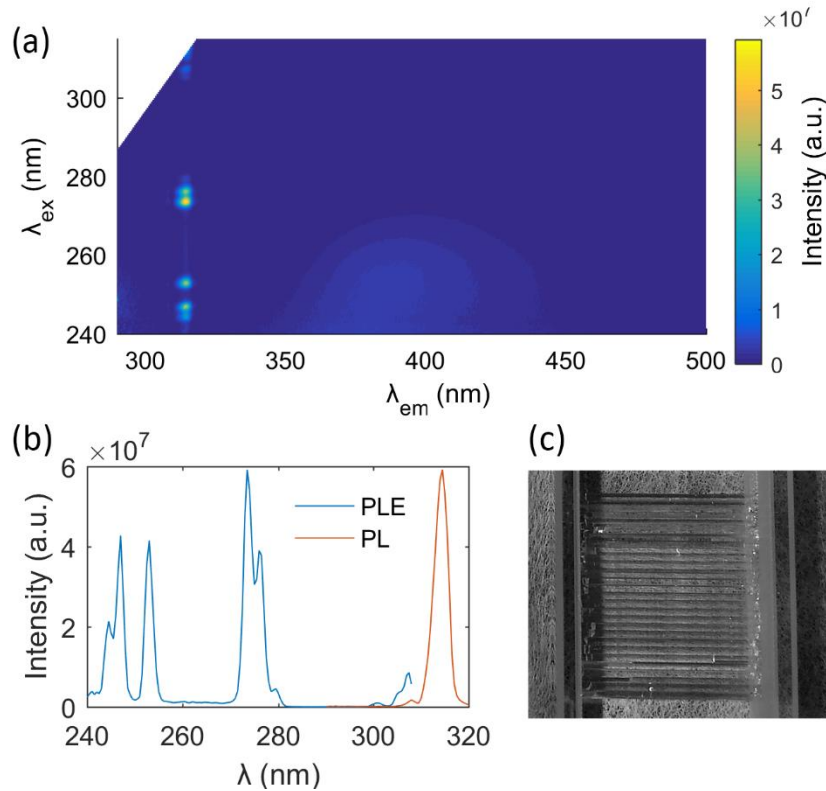


Figure 5.15 (a) 2D PL/PLE spectral mapping of the Gd-doped silica fibre sample. (b) PL ($\lambda_{ex}$ = 274 nm) and PLE ($\lambda_{em}$ = 314 nm) spectra extracted from (a). (c) Silica fibre bundle hold in a cuvette.

## 5.4    Summary

Luminescence given by the $^6P_{7/2} \rightarrow {^8S_{7/2}}$ transition in the Gd-doped fibre was observed with various UV pump sources, including a femtosecond laser, a UV LED source, and a lamp. The hydrogen-loading process can remove the NBOHCs initially present in the samples and passivate defects induced by the femtosecond laser. Photoluminescence spectra of optical fibre bundles and fibre preforms have been recorded. Emissions at 312 nm (phosphosilicate) and 314 nm (pure silica) were observed when pumping to $Gd^{3+}$ $^6D_J$, $^6I_J$, and $^6P_{J=5/2, 3/2}$ energy levels. Oxygen deficient centre was observed in the solution-doping sample with a wide absorption band centred at around 248 nm, which does not affect pumping to $^6I_J$ states. Meanwhile, PL(E) spectra taken before and after fibre drawing reveal that phosphosilicate and pure silica fibres doped with $Gd^{3+}$ are optically active in the UV with emissions observed at $\lambda_{em}$~312 and 314 nm when the samples are pumped at $\lambda_{ex}$~272.5 nm or 252 nm in the phosphosilicate sample A and $\lambda_{ex}$~274 nm or 253 nm in the silica sample B, respectively.

# Chapter 6    Theoretical Analysis of Gd-based Laser

The unique properties of lasers, including monochromaticity, coherence and directionality, make them more desirable than ordinary light in medical, industrial and commercial applications. Based on the information presented in Chapters 4 and 5, the essential requirements for laser action are investigated in this chapter, to theoretically predict the lasing behaviour of Gd, with emphasis on the estimation of the laser threshold power required, followed by the generation of pump light and a discussion on laser cavity designs.

## 6.1    Rate equations

The energy level diagram of Gd$^{3+}$ (recalled in Figure 6.1) indicates a three-level system. Ions in the ground level 1 ($^{8}S_{7/2}$) are excited to level 3 ($^{6}I_{J}$), which is followed by non-radiative decay to $^{6}P_{J}$ levels. The stimulated transition from energy level 2 ($^{6}P_{7/2}$) to level 1 ($^{8}S_{7/2}$) gives rise to laser emission at $\lambda \approx 312$ nm to 314 nm.
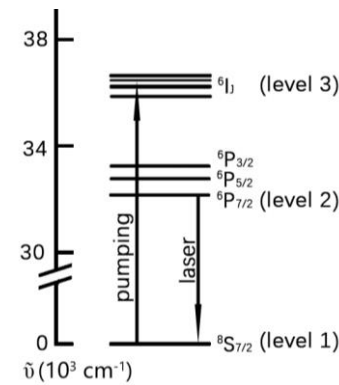


Figure 6.1    Gd$^{3+}$ energy level diagram

The rate equations for the population density of each level are similar to four-level and quasi-three-level systems [22,87,128]:

$$\frac{dn_3}{dt} = (n_1 - n_3)\emptyset_p\sigma_p - \frac{n_3}{\tau_3} \tag{6.1a}$$

$$\frac{dn_2}{dt} = \frac{n_3}{\tau_{32}} - \frac{n_2 - n_2^0}{\tau_2} - (n_2\sigma_e - n_1\sigma_a)\emptyset_l \tag{6.1b}$$

$$\frac{dn_1}{dt} = -(n_1 - n_3)\emptyset_p\sigma_p - \frac{n_1 - n_1^0}{\tau_2} + (n_2 - n_1)\emptyset_l\sigma_l \tag{6.1c}$$

where $n_i$ is the population density of level i and is dependent on location; the superscript 0 denotes the initial state in the absence of a pump light; $\emptyset$ is the photon flux; the subscripts l and p indicate laser and pump, respectively; $\sigma_a$ and $\sigma_e$ are the absorption and emission cross sections at the laser wavelength,

respectively, and are associated with the fractions ($f_i$) of lower and upper manifold populations residing in the laser levels 1 and 2: $f_1\sigma_e = f_2\sigma_a$; $\tau_i$ is the decay lifetime of level i; in the ideal case of lasers with perfect quantum efficiency, $\eta_q \approx 100\%$, $\tau_3 = \tau_{32}$ and $\tau_2$ refers to the spontaneous emission lifetime, meaning that all ions excited to level 3 transfer to level 2 and are for radiative transitions. It is reasonable to assume $n_3 \approx 0$ by considering the fast phonon transition from level 3 to level 2 compared with the pump rate from level 1 to level 3, and the model can be simplified to a two-level system. Since almost all ions remain at level 1 in the unpumped medium at room temperature, $n_2^0 \approx 0$ and $n_1^0 \approx n_t$, where $n_t \equiv n_1 + n_2$ is the total population density. Moreover, in a steady state, when the population densities are clamped, these three equations are equal to zero. Because the transition rate depends on the transition cross section, signal intensity and population difference between these two levels, at least half of Gd$^{3+}$ ions should be excited to the upper laser level in order to achieve lasing, which gives rise to the so-called reabsorption loss. Though the energy is actually not lost, it makes three-level lasers less efficient than four-level ones.

At the laser threshold under steady state, on the one hand, in order to achieve positive net gain for laser action, the round-trip gain provided by population inversion should compensate for the round-trip loss, i.e.:

$$n_{2,th}\sigma_e - n_{1,th}\sigma_a = \alpha_c \tag{6.2a}$$

$$n_{1,th} = \frac{n_t\sigma_e - \alpha_c}{\sigma_e + \sigma_a} \tag{6.2b}$$

$$n_{2,th} = \frac{n_t\sigma_a + \alpha_c}{\sigma_e + \sigma_a} \tag{6.2c}$$

where $n_{i,th}$ is the population density in level i at the threshold. Equations (6.2b) and (6.2c) are derived from Equation (6.2a) with the definition of $n_t$. The left-hand side of Equation (6.2a) provides the gain. The right-hand side ($\alpha_c$) is the cavity loss with the dimension of (length)$^{-1}$, which limits the cavity lifetime given by $\tau_c = 1/\alpha_c c$. The cavity loss consists of the external losses (i.e., the output coupling) and the internal losses arising from, for instance, material absorption and imperfect feedback components (e.g. mirrors and fibre Bragg gratings with non-zero absorption and scattering). The cavity loss can also be induced by scattering, contamination and curved dielectric structures (e.g. bent waveguides and microspheres) resulting in radiative losses [129]. The radiative loss depends on the curvature and the wavelength, and can thus be minimised by optimising the cavity shape or size. To estimate the threshold pump power level required by a Gd-based laser, the first three factors (i.e. output coupling, imperfect feedback and material absorption) are usually dominant and are considered here.

On the other hand, at the onset of lasing, no lasing output occurs and there is no lasing photon in the cavity. Then, the rate equations at the threshold are simplified to:

$$\frac{n_{2,th}}{\tau_2} = n_{1,th}\emptyset_p\sigma_p \tag{6.3}$$

which implies that at the threshold the amount of local pump rate is equivalent to the local depopulation rate governed by the spontaneous decay in the upper laser level. Threshold pump power is then deduced by an integral of pump intensity $\emptyset_p h\nu_p$ over the active medium. Similar to the four-level and quasi-three-level systems [87], the integral that relates the pump power to the local pump rate and population inversion depends on the pump and laser mode profiles. Here, as far as the pump threshold power level is concerned for designing suitable pump source and laser resonator, for simplicity, the integral is estimated using the mode volume $V_p$. This takes advantage of the close pump and laser wavelengths, which result in the good overlap between the pump and laser fundamental modes in a longitudinal pumping scheme. Moreover, $n_1\sigma_p$ determines the pump absorption efficiency $\eta_{abs}$. Therefore, the pump photon energy multiplied by the total number of the depopulated ions per unit time gives the minimum pump threshold $P_{p,mth}$:

$$\eta_p P_{p,mth} = \int \frac{h\nu_p n_{2,th}}{n_{1,th}\sigma_p\tau_2}\, dV \approx \frac{h\nu_p n_{2,th}}{\eta_{abs}\tau_2}V_p \tag{6.4}$$

where $\eta_p$ is the pump efficiency, a cumulative product of (i) in the frequency domain, the overlap between the pump emission and gain medium absorption bands, $\eta_f$; (ii) in the spatial domain, the coupling efficiency, $\eta_s$, determined by the pumping configuration; (iii) the quantum efficiency, $\eta_q$, mentioned above; and (iv) the pump absorption efficiency, $\eta_l$, determined by material loss at the pump wavelength. The subscript mth indicates the minimum threshold, as this approximation does not consider the effect of different pump and laser mode distributions that also influence laser slope efficiency [130]. With the help of Equations (6.2b) and (6.2c), $P_{p,mth}$ approximates to:

$$P_{p,mth} \approx \frac{h\nu_p(n_t\sigma_a + \alpha_c)V_p}{\eta_p\eta_{abs}\tau_2(\sigma_e + \sigma_a)} = \frac{h\nu_p(n_t + \alpha_c/\sigma_a)V_p}{\eta_p\eta_{abs}\tau_2(1 + f_2/f_1)} \tag{6.5}$$

where $f_1$ and $f_2$ are associated with the degeneracies of levels 1 and 2, respectively. This expression is similar to the threshold equation for quasi-three-level lasers. Nevertheless, care should be taken when evaluating the absorption efficiency, $\eta_{abs}$. The exact fraction of power absorbed by ions in the ground level, as expressed in the rate Equation (6.1c), depends on the pump intensity, absorption cross section and ground level population, and thus varies with pumping schemes [131]. In four-level lasers and some quasi-three-level lasers with much smaller lower-laser-level population fraction $f_1$ than the upper-laser-level population fraction $f_2$ [132,133](and hence $\sigma_a \ll \sigma_e$) at the laser threshold, the ground level manifold is not significantly depopulated; therefore, the pump absorption saturation effect is negligible. However, in three-level lasers where the ground level is significantly (>50%) depopulated, the absorption coefficient $\alpha_p'$ for calculating the absorption efficiency $\eta_{abs} = 1 - e^{-\alpha_p'l}$ is less than the absorption coefficient characterised with the low power lamp in previous chapters. With the help of Equation (6.2b), it is given by:

$$\alpha_{p,th}' = n_{1,th}\sigma_p = \frac{n_t\sigma_e - \alpha_c}{\sigma_e + \sigma_a}\sigma_p \tag{6.6}$$

## 6.2    Theoretical laser threshold

To estimate the laser threshold, Table 6.1 lists the optical properties of Gd³⁺ based on the characterisation results reported in previous chapters as well as data from the literature.

Table 6.1 Optical properties of Gd³⁺ for laser threshold estimation.

| Parameter | Value | |
| --- | --- | --- |
| $\lambda_p$ | 274 | nm |
| $\sigma_p$ | $4.44 \times 10^{-25}$ | m² |
| $n_t$ | $1.2 \times 10^{25} \sim 1.2 \times 10^{26}$ | m³ |
| $\sigma_e, \sigma_a$ | $3.3 \times 10^{-26} \sim 4.7 \times 10^{-26}$ | m² |
| $\sigma_e \tau_2$ | $2.34 \times 10^{-28}$ | m²s |
| $\tau_2$ | $\sigma_e \tau_2 / \sigma_e : 5 \sim 7$ | ms |
| $\alpha_m$ | 0.346 | m⁻¹ |
| $\eta_p$ | 70 | % |

The pump wavelength $\lambda_p$ is set to 274 nm for the intense signals around this wavelength in the PL and PLE spectra. The relatively dense upper three ⁶I_J sub-levels in the energy level diagram favour the efficient absorption of a pump source with an emission linewidth of a few nanometres, such as femtosecond-pulsed lasers and LEDs with minimum linewidths limited by minimum possible time-bandwidth product and thermal fluctuation, respectively.

The total population density $n_t$ is decided according to the different dopant concentrations of the samples measured using EDX. Errors in the EDX measurements and induced by microsphere fabrication are much smaller than the difference between two samples.

The absorption cross section at the laser wavelength has been worked out in Chapter 4 with the help of the $n_t \sigma_a$ product, which was obtained from the cut-back propagation loss measurement performed on the fibre samples. The loss in sample A, together with the Gd concentration $n_t$ obtained from a preform disk of sample A using EDX, gives $\sigma_a \approx 1.07 \times 10^{-25}$ m². However, this result is not precise, because the disk and fibres samples were from different sections of the fibre preform. Due to the nature of the MCVD technique, which leads to non-uniform dopant distribution along the preform, the measurement error cannot be evaluated without information on the exact distribution; however, the error should not be underestimated.

Nevertheless, the phosphosilicate sample C does not have this issue since this error is minimised because the fibre and disk samples were from the same region of the preform. Although the cut-back measurement of sample C at the laser wavelength using the lamp was not feasible due to the UV-induced loss resulting in absorption saturation issues, the narrowband UV LED made characterisation at the pump wavelength possible and resulted in reliable pump absorption cross

section of $\sigma_p = 4.44 \times 10^{-25}$ m$^2$. By considering the errors in the EDX measurement, this result is in agreement with the value extracted from [100], in which, the absorption coefficient attributed to 0.5 mol Gd% doped in a sol-gel silica glass were 0.043 cm$^{-1}$ and 0.55 cm$^{-1}$ at the emission and pump wavelengths, respectively, corresponding to $\sigma_a \sim 3.90 \times 10^{-22}$ cm$^2$ and $\sigma_p \sim 4.97 \times 10^{-21}$ cm$^2$.

Then, with $\sigma_p$, a relatively more reliable $\sigma_a$ value can be estimated based on the $\sigma_p$ to $\sigma_a$ ratio reported in [100] for a SiO$_2$:0.5 mol% Gd sample, by considering that the sol-gel sample employed in the present study was made by one of the authors using the same technique and that both samples were not heavily doped. With the $\sigma_p$ to $\sigma_a$ ratio of ~12 extracted from the absorption spectrum in [100], the absorption cross section at the laser wavelength is approximately $\sigma_a \approx 3.7 \times 10^{-26}$ m$^2$.

The $\tau_2 \sigma_e$ product can be determined from the recorded PL spectrum. However, the characterisation of $\tau_2$ is not completed during the present study due to the lack of a suitable pump source and amplifier in the UV; therefore, its characterisation is recommended for future work. By considering the non-degenerate orbital number of the ground level and the spectral profile, based on a true-three-level model, it is expedient to set $\sigma_e$ equivalent to $\sigma_a$, which, together with the $\tau_2 \sigma_e$ product, suggests a decay lifetime of $\tau_2 \approx 6.3$ ms.

In [94,134,135], the lifetimes in a GdCOB crystal, a crystalline GdCl$_3$·6H$_2$O, Gd-doped calcium phosphate glasses and a 3 mol% Gd-doped sol-gel silica glass were 2.79 ms, 7.2 ms, 4.83 to 5.46 ms depending on dopant concentrations and 5 ms, respectively. The last one has the most similar composition to the samples in this study. If $\tau_2 \approx 5$ ms, with the $\sigma_e \tau_2$ product, the transition cross section at the emission wavelength is $\sigma_{a,e} \approx 4.69 \times 10^{-26}$ m$^2$. In the simulation, in order to take both cases into consideration, since the reliable $\sigma_e \tau_2$ product should be fixed, $\sigma_{a,e}$ and $\tau_2$ are swept within the ranges listed in Table 6.1.

The pump efficiency $\eta_p$ is determined based on the material loss at $\lambda$ = 274 nm in the phosphosilicate sample as well as assumed perfect $\eta_f$, $\eta_s$ and $\eta_q$. $\alpha_m$ is the internal loss due to material absorption at the laser wavelength and can be evaluated in fibre samples from cut-back propagation loss measurement results. It should be noted that the exact $\eta_p$ and $\alpha_m$ values are further modified by UV-induced loss during the experiment.

Cavity loss $\alpha_c$ and mode volume V$_p$ vary with the design of a laser cavity. Fibre lasers benefited from their small core sizes, long length and high surface area to volume ratio tend to have excellent beam quality, extraordinary brightness and small thermal detrimental effects at high power levels. Relatively low laser thresholds can be achieved by reducing the core size, which improves light confinement as well as intensity. In a fibre Fabry-Pérot cavity, due to the cavity loss, the ratio of the

power after one round-trip to the initial power becomes: $P_1 = P_0 e^{-2\alpha_m l} R_1 R_2$, where $R_1$ and $R_2$ are the reflections at the two ends of the cavity. Therefore, the total internal loss per unit length is given by:

$$\alpha_c \approx \alpha_m - \frac{\ln(R_1 R_2)}{2l} \tag{6.7}$$

Then, the laser threshold pump power can be estimated by substituting Equations (6.6) and (6.7) in (6.5). The result in Figure 6.2 shows the dependence of threshold on cavity length l and mode radius ω for a Fabry-Pérot cavity with $R_1$ = $R_2$ = 95%. The reflections vary with the cavity design which will be discussed later. $\sigma_e$ and $\sigma_a$ are $3.7 \times 10^{-26}$ m$^2$, and $n_t$ is set to the concentration of sample A disk (i.e. $1.036 \times 10^{26}$ m$^3$), which assumes that the concentration in the fibre is ~ 0.14 atomic%.

The blank region at cavity lengths shorter than around 0.02 cm corresponds to cavity losses higher than what can be offset by the gain which is limited by the transition cross section and dopant concentrations; the latter further limits the population inversion. In such short cavities, the loss is dominated by the output coupling. This implies that lasing is not achievable within this region.

The threshold does not monotonically increase with cavity length, as the latter also affects round-trip loss, reabsorption in a three-level system and pump absorption. An optimal value can be found to minimise the threshold. Within the sweep range at a mode radius of 2.35 μm (i.e., the radius of the fundamental mode in the fibre sample A (Figure 6.3)), the laser threshold ranges from below 20 mW at l = 0.07 m to above 160 mW at l = 1m.
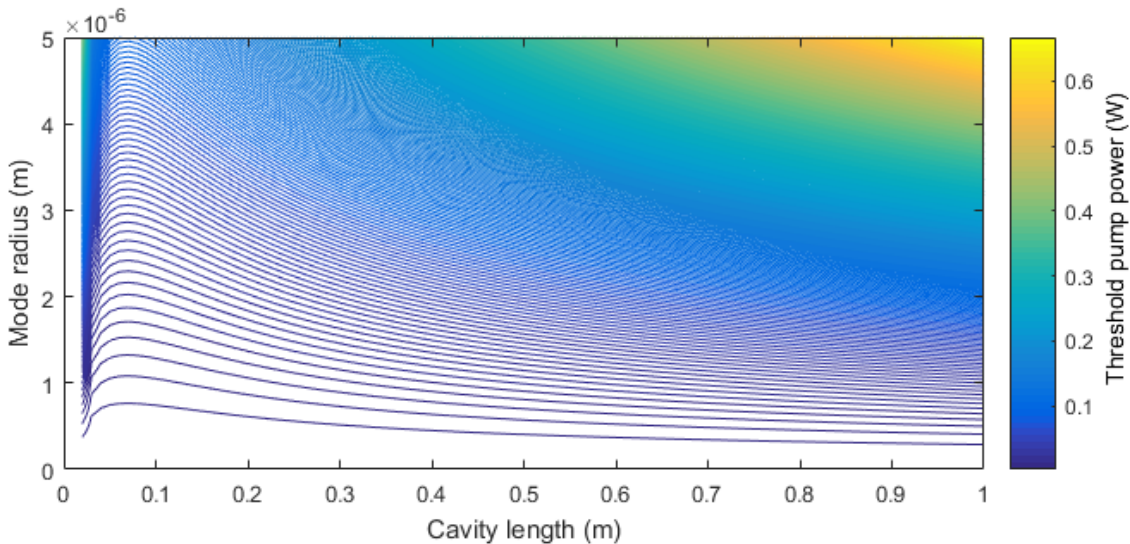


Figure 6.2 A contour plot of $P_{p,mth}$ as a function of cavity length and mode radius.

The estimations, as mentioned above, assume that both the pump and laser beam are guided in the fibre fundamental core modes and are well overlapped with each other, as indicated in Figure 6.3. However, the phosphosilicate fibre sample has a low refractive index coating for the cladding

pumping scheme [136,137], in which the pump light can be guided in the cladding. The resultant polymer-clad and large glass-core multimode fibre for the pump beam makes high input coupling efficiency feasible with a powerful but low beam quality source (e.g. laser diodes); thus it is beneficial for optical amplifiers with high-power output. However, the subsequent increase in the pump mode area results in a pump power in the order of watts, which is higher than the thresholds of most rare-earth fibre lasers due to the nature of the three-level system as well as the cross section of the forbidden transition in $Gd^{3+}$, which is nearly 70 times smaller than that of Yb $^2F_{5/2} \rightarrow$ $^2F_{7/2}$ emission transition at 980 nm in Yb-doped silica fibre [22]. Moreover, the UV curable polymer is unlikely to be suitable for guiding the deep-UV pump, though it may facilitate a two-photon pumping scheme. Therefore, a small beam size with high local intensity is preferred to offset this disadvantage at this stage.
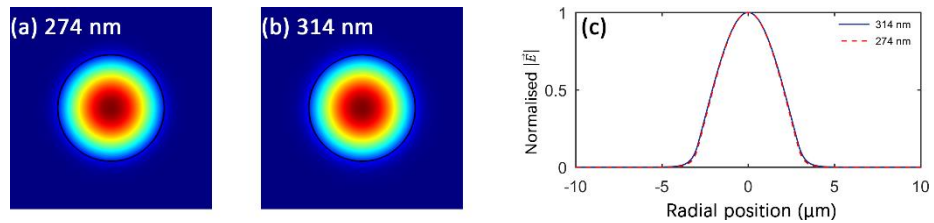


Figure 6.3 Normalised electric field norm $\left|\vec{E}\right|$ of the fundamental modes at (a) pump and (b) laser wavelengths with (c) their overlap in a step-index fibre with $r_{co}$ = 2.9 μm and $\Delta n_{co/cl}$ = 0.006.

Figure 6.4 evaluates the effects of $Gd^{3+}$ concentration and transition cross sections (within the margin of error) on laser threshold. In Figure 6.4(a), $R_1$ = $R_2$ = 95%. The cavity length, 0.07 m, and the mode radius, 2.35 μm, are decided based on the results presented in Figure 6.2 and Figure 6.3, respectively. At the edge in yellow, despite sufficient $Gd^{3+}$ concentrations, the tiny proportion of the population in the ground level results in low pump absorption efficiency and thus high laser thresholds (> 50 mW). Figure 6.4b is an example of micro-lasers that trap light efficiently with long effective interaction lengths and thus efficient pump absorption and high local intensity, which, especially in four-level lasers, make near-zero thresholds possible [33]. Therefore, threshold pump absorption $\eta_{abs}P_{p,mth}$ instead of $P_{p,mth}$ from Equation (6.5) is evaluated, with $R_1R_2$ = 99.9%. The mode radius and cavity length are 0.5 μm and 0.2 mm, respectively. The result suggests a laser threshold power level of a few microwatts. Even if $\eta_{abs}$ is considered, the threshold at, for example, $\sigma_a = 3.7 \times 10^{-26}$ m$^2$ and $n_t = 1.04 \times 10^{26}$ m$^{-3}$ is less than of that in (a). However, while short cavity lengths imply low round-trip gains, further reducing the cavity length will hinder laser action, similar to the effect of a low $Gd^{3+}$ concentration. The blank region corresponding to insufficient population inversion at low $Gd^{3+}$ concentration is evident. Nevertheless, in practice, an increase of $Gd^{3+}$ concentration may lead to an increase in defects due to the damage of Si-O bonds by relatively large Gd ions, which results in high material loss and high threshold power. Therefore, optimisation of the host material and dopant concentration is desirable for future work.
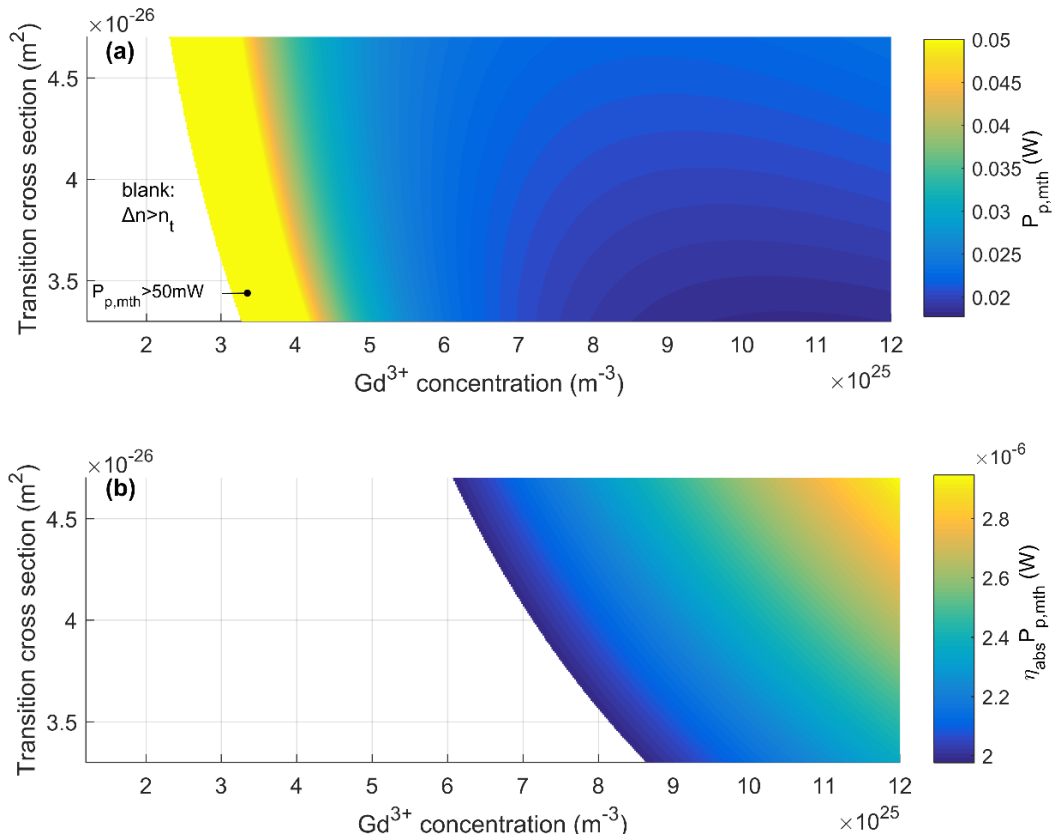
Figure 6.4 Theoretical minimum pump threshold as a function of transition cross section $\sigma_{a,e}$ and Gd concentration, where (a) l = 0.07 m, $\omega$ = 2.35 µm and $R_1$ = $R_2$ = 95%, and (b) l = 0.2 mm, $\omega$ = 0.5 µm and $R_1 R_2$ = 99.9%.

## 6.3    Pump source

As indicated by the simulated results, a pump source with an output power of a few milliwatts at $\lambda \approx 274$nm is desirable. Compared with transition metal ions such as $Ti^{3+}$ in which transitions between unshielded electronic d levels strongly interact with crystal fields and lead to large bandwidths [138], and compared with most other rare-earth ions such as $Er^{3+}$ and $Yb^{3+}$ where Stark splittings give rise to a broad absorption spectrum in the IR [139,140], $Gd^{3+}$ with increased ground state stability associated with the half-filled 4f shell features narrow transition linewidths in the UV, which implies a tight wavelength tolerance placed on the pump source. However, without the help of nonlinear frequency conversion, gas, solid-state or dye lasers operating at 274 nm are not commercially available at present, while the short-wavelength components from a broadband UV lamp such as that used in previous chapters tend to induce defects to the silica hosts. Therefore, a suitable pump source should be established prior to laser demonstration.

The LED array used in the previous chapters provided up to ~15 mW in practice within a 10nm FWHM emission band centred at 282 nm; however, it requires improvements in beam quality in order to reach an intensity higher than the laser threshold. By considering the cost of multiple LED

arrays and the necessary optical components for beam shaping, compared with that of a BBO crystal for harmonic generation, and by considering the time limitations[1], the present study benefited from the availability of a tuneable Ti:sapphire laser plus an optical parametric oscillator (OPO) system at the ORC, with which a deep-UV pump was generated via frequency doubling of a green laser using a BBO crystal.

The output from the Mai Tai HP Ti:sapphire laser plus Inspire HF 50 OPO system used can reach up to above 300 mW. Due to a four-day time limit with the available equipment, in order to decide the parameters of BBO crystal and estimate SH power level, the pulse duration $\tau_{fs}$ of 200 fs and output beam M$^2$ factor less than 1.2 (TEM$_{00}$ mode) were taken directly from the device manual. The output beam features a tiny divergence angle, $\theta_1 \approx 2$ mrad. After the harmonic generation, the SH beam quality was characterised for the laser demonstration. BBO is a negative uniaxial crystal ($n_o > n_e$). By taking advantage of polarisation-dependent dispersion, the critical phase-matching condition for SHG was achieved by using a type I BBO crystal in which the refractive index $n_{\omega}^{o}$ of the ordinary polarised fundamental beam is equal to $n_{2\omega}^{e}(\theta_m)$ of the extraordinary polarised second harmonic beam, when the fundamental beam propagates at an angle $\theta_m$ relative to the crystal optic axis. $\theta_m$ decides the crystal cutting angle and can be derived from the index ellipsoid with the condition $n_{\omega}^{o} = n_{2\omega}^{e}(\theta_m)$ [54]. $\theta_m$ is 45.5° for SHG of 274 nm from 548 nm, where $n_{2\omega}^{o}$ = 1.7496, $n_{2\omega}^{e}$ = 1.6087 and $n_{\omega}^{o}$ = 1.6736.[2]

Although a long interaction length normally implies high power conversion efficiency, for short pulses, the thickness of the BBO crystal is limited by the group velocity mismatch (GVM) between the fundamental and second harmonic pulses, which leads to the so-called temporal walk-off issue and increases the pulse duration. It was found that a ns-pulse UV laser would induce huge loss in the Z fibre (presented in the next chapter), and a collaborator claimed to have successfully performed a similar UV light generation experiment using the same type of fibres and a 274 nm fs-laser without noticing this detrimental effect, although it was later subsequently considered doubtable and in need of further investigation. At this stage, maintaining the femtosecond pulse duration was desirable. Therefore, the BBO thickness needed to be small enough to ensure that the fundamental overlaps with the second harmonic inside the crystal in the temporal domain. GVM can be determined using BBO dispersive refractive indexes and turns out to be 523 fs/mm for the

---

[1] Setting up a suitable pump for fibre laser demonstration was initially assigned to a researcher in 2015. By considering the high laser thresholds required by fibre lasers, a nanosecond-pulsed pump was established by the end of 2017 and characterised by February 2018. Unfortunately, its seed source stopped working after being switched to remote control by the manager. The repair took approximately three months; thus a simple self-built femtosecond-pulsed pump was set. If time and funds permit, LED beam shaping could be considered for micro-lasers with low thresholds, for possible low UV-induced defects.

[2] BBO dispersive refractive indexes: $n_0^2 = 2.7405 + \frac{0.0184}{\lambda^2 - 0.0179} - 0.0155\,\lambda^2$; $n_e^2 = 2.3730 + \frac{0.0128}{\lambda^2 - 0.0156} - 0.0044\,\lambda^2$ [175]

SHG of 274 nm, indicating an interaction length $\tau_{fs}$/GVM of 0.38 mm. By considering the spatial walk-off issue and the possible estimation error in the pulse duration, the thickness of the BBO (from Eksma Optics) used in the following experiments was 0.3 mm.

During the experiment, both the central wavelength (tuned within a range from 545 nm to 550 nm) and the linewidth (5±0.5 nm) of the fundamental beam were monitored in real time by a built-in spectrometer of the OPO system. The spot size measured close to the HF 50 output end was $\omega_2$ = 475 um (1/e$^2$, the average of the x- and y- axes values) and was focused using a lens f = 50 mm to the BBO, as illustrated in Figure 6.5.
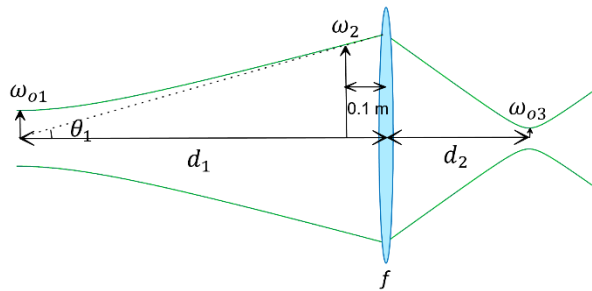


Figure 6.5 Fundamental pump laser characterisation schematic diagram.

The lens was set 0.1 m after $\omega_2$. Then, the spot size $\omega_{o3}$ at the focal point, as well as its Rayleigh range, was estimated using the textbook formula for Gaussian beams and the ray transfer matrices. The estimations were carried out by letting M$^2$ and $\theta_1$ be 1.2 and 2 mrad, respectively. Then, $\omega_{o3}$ turned out to be 18 μm with a Rayleigh range $z_{R3}$ of 1.6 mm, which is much longer than the crystal length, suggesting that the beam radius is approximately constant within the BBO.

Although tight focusing of the fundamental beam facilitates high intensity as well as high conversion efficiency, the fact that the Poynting vector of the extraordinary polarised second harmonic propagates at an angle against the crystal—which is the so-called spatial walk-off—leads to a deviation of intensity propagation direction away from the wave vector with a walk-off angle ρ given by [141]:

$$\rho = -\frac{1}{n_e(\theta,\lambda)}\frac{\partial n_e(\theta,\lambda)}{\partial\theta} \tag{6.8}$$

It turns out to be 76 mrad for the aforementioned system. This walk-off issue can be compensated by exploiting two crystals with opposite walk-off directions [141]. Here, with a single crystal, the resultant degraded second harmonic power can be estimated using the analytical solution in [142,143] and is 9.3 mW for a fundamental power of 300 mW (i.e. $P_{peak}$ = 17.6 kW, assuming a Gaussian profile), where the field-gain coefficient is approximately 1.71×10-4 W$^{-1/2}$ for BBO with a nonlinear coefficient $d_{eff}$ of 2.01 pm/V [143,144], and where the dimensionless function—which

determines the focusing dependence of the SH—is estimated from Figure 2 in [142] and is h(2.9, 0.094) ≈ 0.066. 2.9 and 0.094 quantify the effects of transverse walk-off and focusing, respectively, based on the BBO thickness, beam profile and walk-off angle. Depending on the exact green laser parameters (e.g. $M^2$ value and pulse duration), this roughly estimated SH power could be above 10 mW; however, this estimation does not consider the temporal walk-off issue [145], which further degrades the conversion efficiency. The complex mathematical work is outside the scope of the present study and is thus not discussed here. Additionally, the conversion efficiency is also affected by the exact beam quality and losses induced by optical components.

In the experiment (as illustrated in Figure 6.6a), the SH DUV beam after the BBO was collimated and focused using two lenses. SH power was measured after two dichroic mirrors with high reflection at the SH wavelength and high transmission at the fundamental (see Figure 6.6b).
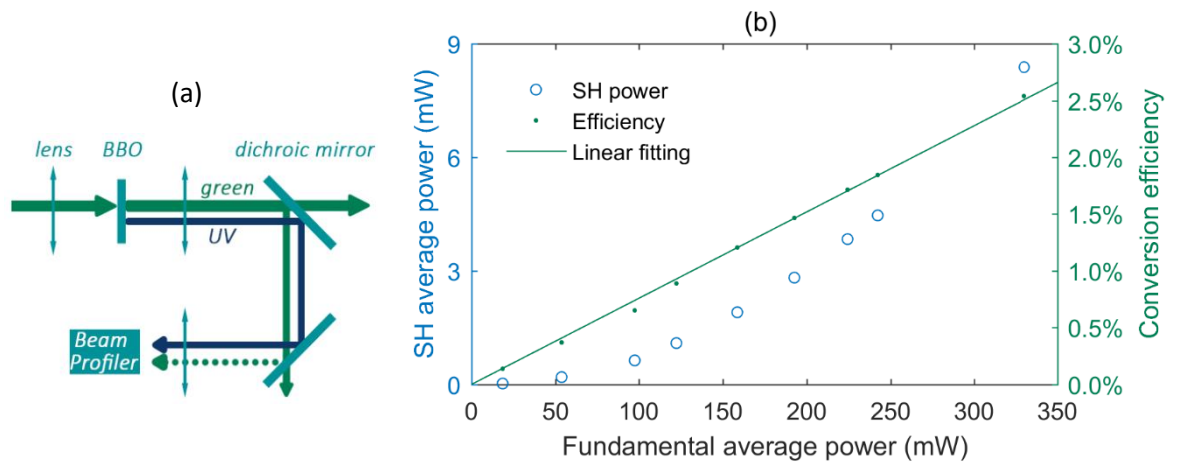


Figure 6.6 (a) SHG schematic diagram, and (b) experimental conversion efficiency.

In the experiment, the effect of green laser residue on the broadband power detector used was removed with additional measurements on the green with a UV filter. The results confirm the linear dependence of the conversion efficiency upon the fundamental power, with a SH power of 8.4 mW for a fundamental power of 330 mW. This is comparable to the theoretical prediction with a reasonable difference arising from the temporal walk-off issue, additional losses induced by optical components and the exact beam quality that might slightly differ from the parameters obtained from the manual.

Prior to laser demonstration, the $M^2$ factors were characterised for a lightly focused beam so that the waist of a tightly focused beam can later be determined by only measuring its divergence. The beam waists at different longitudinal positions are plotted with standard deviation (SD) error bars in Figure 6.7. It was confirmed with a filter removing the DUV component that the weak green laser residue did not affect the results. The measurement errors were dominated by the signal-to-noise ratio limited by the weak signal relative to the beam profiler sensitivity, especially at positions away

from the waist, where large spot sizes result in low intensity. SD$^{-2}$-weighted Gaussian fittings suggest M$^2$ factors of 1.47 ± 0.03 and 1.60 ± 0.04 for horizontal X and vertical Y directions, respectively. The difference between the two directions originated from the elliptical cross section of the fundamental beam and the walk-off issue.
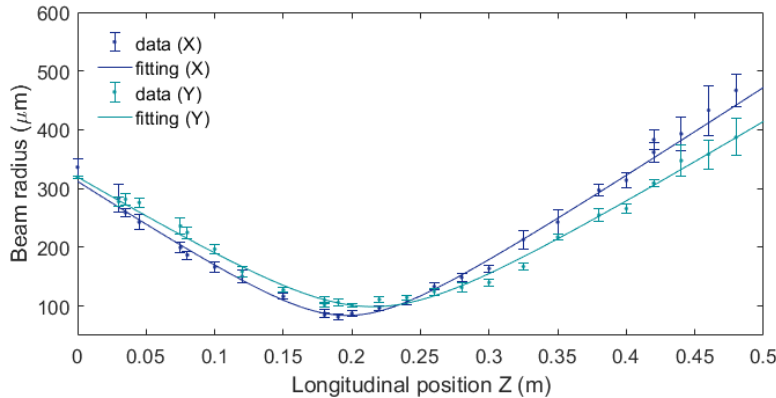


Figure 6.7 Beam radius of a lightly focused SH beam in horizontal X and vertical Y directions as functions of longitudinal positions with fittings weighted by SD$^{-2}$.

## 6.4 Fabry-Pérot resonators

In addition to the gain medium and the pump source, laser operation requires another essential component—the resonant cavity—which provides positive feedback by making the light repeatedly pass through the gain medium, and thus favours the stimulated emission. The resonator can be designed to select specific laser modes and hence control the output conditions including spatial coherence, directionality and brightness. For instance, the longitudinal modes in Fabry-Pérot resonators are determined by cavity lengths. The transverse modes, which are self-reproducing after each round-trip inside the cavity, can be selected by, for example, mirror radii and curvatures. In fibre lasers, the modes are discrete solutions of Maxwell's equation based on continuity at the core-cladding interface and can be selected by tailoring fibre refractive index profiles and excitation methods. By taking advantage of the excellent beam quality of the fundamental mode with an M$^2$ value close to one, a double-clad fibre can also be exploited as a brightness converter [22]. As mentioned in previous sections, the laser threshold increases with the cavity loss which includes but is not limited to output coupling loss and reflector absorption. The 4% refection from the glass-air interface at fibre ends is far less than that assumed in the modelling and leads to a high threshold power exceeding the maximum pump output available, which makes additional feedback components necessary. Therefore, Fabry-Pérot resonators formed with fibre Bragg gratings [146] or dielectric mirrors deposited at cleaved fibre ends [147] are considered here, followed by micro-resonators in the following chapter. External feedback is not discussed at this stage, for the additional losses induced by components for collimation and focusing.

### 6.4.1 Fibre Bragg grating

In fibre lasers, fibre-Bragg-grating-based laser resonators are commonly used and can be fabricated via two prevailing approaches. In a grating, the refractive index perturbation ($\Delta n$) along the light propagation direction is parodic, and the reflectance reaches its maximum at wavelength $\lambda=2n_{eff}\Lambda$, where $n_{eff}$ ($\gg\Delta n$) and $\Lambda$ are the effective index and the grating period, respectively. One of the fabrication approaches is the phase mask technique [148], in which the refractive index of a photosensitive fibre exposed to UV laser light transmitted through a phase grating mask is periodically modified according to the UV interference pattern. Due to the nature of the fibres sensitive to UV radiation, they are not available to guide the UV pump light in this project; thus, exploitation of this technique may require investigation of, for example, the effect of gas loading on the photosensitivity of the fibres available. The other prevailing approach is the point-by-point technique [149]. As its name indicates, the grating is written directly into the fibre point-by-point using focused laser pulses. A few attempts were made for the UV fibre laser project to fabricate gratings in the Z fibres and Gd-doped fibres using the IR femtosecond laser at $\lambda$= 1030 nm, which was used for the defects characterisation in Chapter 5. Figure 6.8 presents one of the fabricated gratings.

(a)  (b)
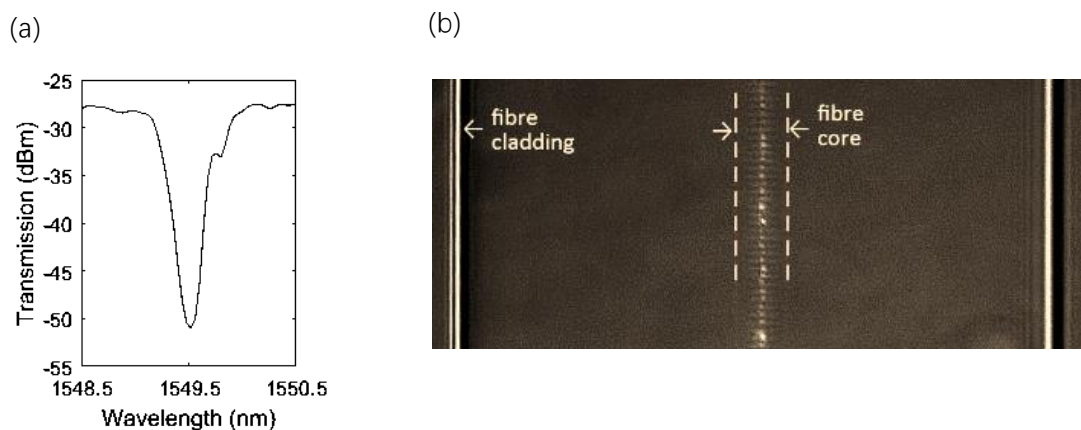


Figure 6.8 (a) Transmission spectrum of a third-order grating written into a fibre core and (b) a photograph of the grating.

Limited by the structure fineness, only the higher-order grating in the IR was observed in the transmission spectra. Utilisation of the harmonics at short wavelengths from this writing laser to reduce the diffraction-limited spot size or an investigation into sub-wavelength structures [150,151] could be considered for future work. Nevertheless, care should be taken when optimising the laser parameters, as the formation of gratings was accompanied by the formation of defects due to the high peak power and nonlinear multi-photon excitation which, as investigated in Chapter 5, increase absorption loss in the UV. Although thermal treatment after fabrication can remove colour centres, the refractive index change could be partly attributed to these colour centres, depending on the glass composition and laser parameters [152,153]. Therefore, high-performance gratings

with losses of less than 1% for the milliwatts pump source are not guaranteed, which, coupled with the time required for optimisation and the availability of the writing-laser with its wavelength fixed for other projects, makes it necessary to consider other resonators.

### 6.4.2    Dielectric mirror

Dielectric mirrors consisting of multiple layers of materials with different refractive indices deposited at fibre end facets are then considered. The transmittance T and reflectance R of a multilayer structure can be estimated using the transfer matrix method [154]:

$$\begin{pmatrix} M_{11} & M_{12} \\ M_{21} & M_{22} \end{pmatrix} = D_0^{-1}[D_1 P_1 D_1^{-1} D_2 P_2 D_2^{-1}]^N D_S \tag{6.9a}$$

$$R = \left| \frac{M_{21}}{M_{11}} \right|^2 \tag{6.9b}$$

$$T = \frac{n_S}{n_0} \left| \frac{1}{M_{11}} \right|^2 \tag{6.9c}$$

where, for normal incidence:

$$D_m = \begin{pmatrix} 1 & 1 \\ n_m & -n_m \end{pmatrix} \tag{6.10a}$$

$$P_m = \begin{pmatrix} e^{ik_m h_m} & 0 \\ 0 & e^{-ik_m h_m} \end{pmatrix} \tag{6.10b}$$

where $k_m$, $n_m$ and $h_m$ are the wave vector, the refractive index and the thickness of the $m^{th}$ layer material, respectively; subscripts 0 and s refer to the initial and final mediums, respectively. Similar to gratings, constructive interference from the reflection at each interface results in a high reflectance. The coating materials should have low losses (i.e., low extinction coefficients) at Gd-related wavelengths. Although aluminium is widely used for mirrors in the UV, with a refractive index of 0.289-3.760i at 314 nm [155,156], a silica-aluminium-air structure provides a reflectance of 90% with an aluminium thickness of 50 nm and an absorption loss of around 10% which is not desirable for the low-loss input and output coupling required. Regarding dielectric mirrors, fluoride and oxide are commonly used as coating materials. Figure 6.9 shows two examples based on the refractive index from the literature and the transfer matrix method.

The layer thicknesses are determined by the material refractive indexes and central wavelengths, while the number of layers depends on the index contrast as well as the required reflectance and stopband width. Due to the relatively high absorption loss at short wavelengths, a low index contrast with a thick stack may lead to low pump efficiency. The exact complex refractive indexes

depend on fabrication techniques and parameters; thus, optimisation would be required for this approach in the future.

The evaluation can also be carried out using the FEM method with commercially available software (e.g. COMSOL). In a 2D square model with (i) the same geometry and material parameters, (ii) perfect electric conductor boundary conditions for a linearly polarised infinite plane wave, and (iii) two port boundary conditions at the input and output ends with a linear polarised field being excited at one port, results identical to those presented in Figure 6.9 can be obtained.
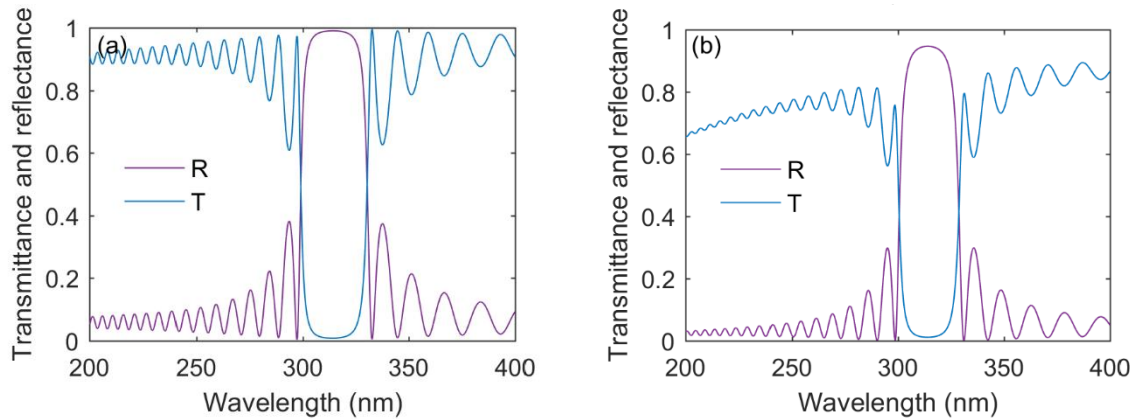


Figure 6.9 Transmittance T and reflectance R of (a) a $SiO_2$-$(Al_2O_3$-$SiO_2)^{25}$-air multilayer structure, and (b) a $SiO_2$-$(LaF_3$-$MgF_2)^{27}$-air multilayer structure. The thicknesses of $Al_2O_3$, $SiO_2$, $LaF_3$ and $MgF_2$ layers are 45.99 nm, 52.44 nm, 48.70 nm and 54.63 nm, respectively, based on dispersive refractive indexes extracted from [156–159].

## 6.5    Summary

In this chapter, the Gd-based UV laser threshold has been theoretically evaluated based on the rate equations for a three-level system and the Gd optical properties reported in previous chapters, followed by generation of the pump required and a brief discussion on FP laser cavities. It is shown that a FP cavity with high internal reflection (R>95%) at the emission wavelength for low laser threshold and high transmission at the pump wavelength for efficient input coupling requires additional study, and is thus not available at present. Higher absorption and output coupling losses imply a higher pump threshold, which are not preferred, by considering the pump power available, the photodarkening issues, and the dopant concentrations of the samples. Moreover, the high absorption and low coupling efficiency caused by UV modification in the silica fibre samples would further increase the fibre laser threshold. Therefore, instead of discussing fabrication and optimisation processes required by demonstration of a Gd-based UV fibre laser, microsphere resonators are introduced and employed in the following chapter.

# Chapter 7     UV generation in Gd-doped Microspheres

The previous chapter highlights the necessity of considering the micro-resonators for lasing demonstration at this stage. In this chapter, microspheres are investigated, beginning with the field distributions of the whispering gallery mode and the fabrication of microspheres, which is followed by a discussion on the spree-face pumping scheme. Then, UV generation is experimentally demonstrated in Gd-doped silica glass microspheres.

## 7.1     Whispering gallery modes

To minimise cavity loss and simplify the fabrication process, microcavities that can trap light in a small volume for long periods [160] depending on quality factor limited by loss and can substantially decrease laser threshold [33,161–163] are desirable. Among various micro-resonator structures, glass microsphere is a suitable candidate, considering its manufacturing complexity and the available Gd-doped fibre samples.

Based on the foregoing pioneering theoretical work reviewed in Chapter 2, take a 30 μm-radius microsphere as an example:  Figure 7.1 shows normalised fundamental TE mode fields at different resonant wavelengths and high-order mode fields at λ ≈ 314 nm.

It can be found that the mode number q corresponds to the number of field extremum in the radial direction; l-m+1 yields the same result but for the polar direction; and m refers to the result in the azimuthal direction: $2\pi n_{eff} \approx m\lambda$. For TE (or TM) modes, the electric (or magnetic) field is parallel to the surface, $E_\theta$ (or $H_\theta$) = $\psi_{lmn}$, and $E_\phi = E_r$ (or $H_\phi = H_r$) = 0. The evanescent tails are short at short wavelengths, with small fractions of power interacting with the field outside. Low-order radial modes are closer to the surface than high-order modes and are thus more sensitive to surface perturbation [164]. The latter can be suppressed by modifying the filling material. The mode volume is around 10 cubic micrometres, which is more than four orders of magnitude smaller than the volume in metre-long fibres, implying a much lower laser threshold.

## 7.2     Gd-doped silica glass microsphere fabrication

The prevailing method for fabricating silica glass microspheres is melting material, based on which the spherical shape benefiting from its small surface-area-to-volume ratio is naturally formed under surface tension, resulting in higher quality factor than what other techniques (e.g. micromachining and chemical etching) can achieve. The raw material can be glass powder [165,166], bulk [167] and fibre [168]. The heat source can be torches [166,169], ceramic heater [170] (e.g. the one used for fibre
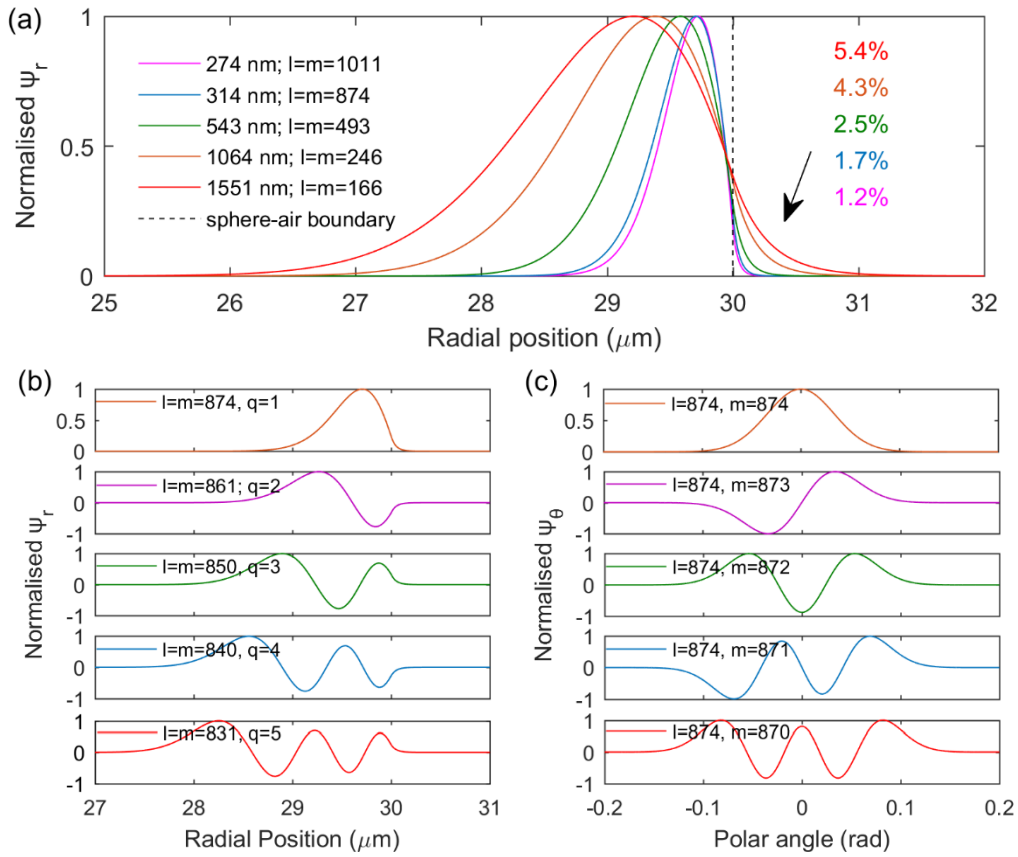
Figure 7.1 (a) Radial field distributions of fundamental TE modes normalised with respective peak values at different resonant wavelengths with percentages of the field outside the microsphere. Normalised (b) radial and (c) polar field distributions of the fundamental and high-order modes at $\lambda \approx 314$ nm.

tapering), electric arc  [165,168] (i.e. those in fibre fusion splicers), furnace [167], or lasers, which benefit from high material absorption at specific wavelengths accompanied by rises in temperature. By considering the preform and fibre samples available and the complexity of fabrication processes, microspheres were fabricated by melting fibre tips using a $CO_2$ laser. The use of $CO_2$ lasers helps to achieve localised heating and rapid energy control with reduced contamination and without an extra polishing step. It was also employed in the development of the fibre-pulling methods used in gravitational wave detector mirror suspensions [171].

To fabricate Gd-doped glass microspheres, Gd-doped silica (sample B) tips were prepared from doped fibre canes with diameters ranging from 500 μm to 700 μm (Figure 7.2). The fibre cane was set vertically with its top and bottom ends fixed on one 3D translation stage and one fixed stage, respectively. In the beginning, the collimated laser beam was launched directly to the sample. The power was increased gradually until the temperature reached around 1,000 °C, at which the cane could be pulled. By lifting the upper stage, the cane was tapered down to a diameter of a few tens of micrometres. A ZnSe lens was then set before the sample to focus the beam for fine fabrication. By controlling the moving speed of the upper stage, the cane was further tapered and separated

from its lower section with a diameter of less than 10 μm. Regarding the doped phosphosilicate (sample A) microspheres, since there were only fibre samples available with undoped cladding, which decreases the average dopant concentration by three orders of magnitude and impedes laser action, the cladding was removed using HF (by Neil Sessions at the ORC).
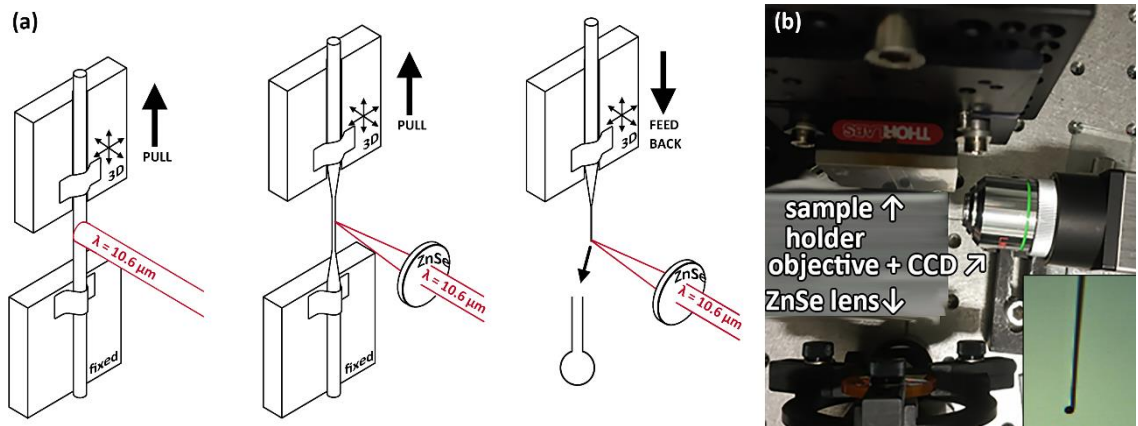


Figure 7.2 (a) Fibre tip pulling and microsphere fabrication process. (b) Top view of the enclosed fabrication setup with a CCD image of a sample under fabrication in the inset.

Once a tip was fabricated, by focusing the laser beam to its end, the surface tension resulted in a spherical structure, the diameter of which was tailored by controlling the amount of material fed back to the laser focusing point. It was noted in the beginning that sometimes the size suddenly decreased during the fabrication. This decrease might be caused by a high temperature arising from self-focusing inside the molten part, which led to evaporation. Because the dopant and the host material have different boiling temperatures, this can change the dopant concentration and should therefore be handled carefully. The offset between the microsphere centre and the fibre axis due to the temperature difference between the front and back sides of the sample relative to the laser was monitored using an objective and was suppressed by rotating the sample, which also improved its uniformity. However, it should be noted that in the lasing experiment, the uniformity can be modified by the UV pulsed pump, which has a double-edged effect on the spree-space coupling reported in the following sections. The size of the microsphere was roughly estimated from the CCD image during the fabrication and confirmed after by examining the sample under a calibrated microscope in the laboratory. The latter requires the sample to be removed from the stage, which can be circumvented by improving and calibrating the objective and the CCD in the future.

Figure 7.3 shows some examples of microspheres with different diameters. Since only the upper stage (in Figure 7.2a) was adjusted to pull the fibre cane, and this pulling was handled manually, only one tip could be made each time and the tapering region was sometimes crooked. Motorisation of the stages to pull the sample from both ends with well-controlled speeds or the application of force or weight to pull it from the bottom [170] could be considered in the future to

generate relatively better and possibly reproducible quality. Additionally, the fibre canes can also be pulled from both ends using the fibre tapering setup equipped with a micro-heater employed in Chapter 3, provided that the samples are fine enough to fit in the heater without being contaminated.

OMFs for power coupling were fabricated using the fibre tapering setup. The waist diameters were measured using SEM after the experiment.
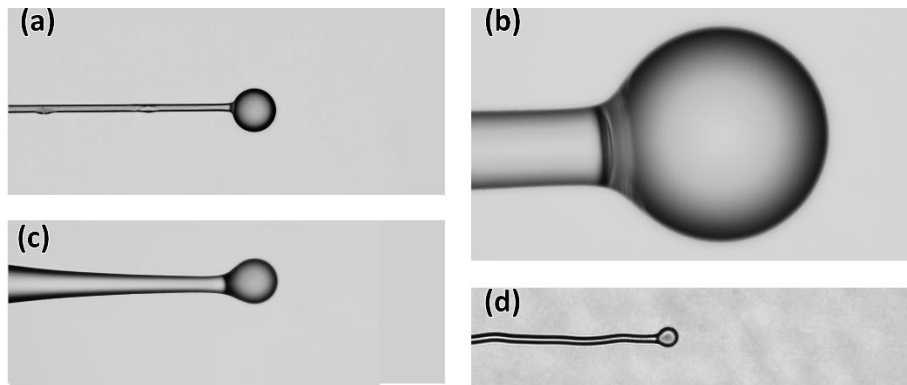


Figure 7.3 Examples of Gd-doped microspheres with radii of (a) 27.5 μm, (b) 134 μm, (c) 28.8 μm and (d) 14 μm.

## 7.3     Pump power coupling into fibres

It would be preferable to couple the pump light into a microsphere through a microfibre with which phase-matching and high coupling efficiency could be achieved and tuned, by tailoring microfibre diameter and the spacing between the microsphere and the fibre. This approach, however, was hindered by UV-induced modification in the glass. Figure 7.4a shows the output from a 60-cm-long untapered Z fibre. To briefly examine the power-dependent response, the pump power was increased step by step, which corresponds to the sharp increases in the figure. Each increase was followed by a steep decrease (i.e., the spike that does not fit exponential decay). The input was adjusted by tuning attenuators, thus the spikes are real responses from the sample and irrelevant to the stability of the source. This is more severe at high power levels, due to the power-dependent UV modification in the material. In the end, the output power reduced to below 20 μW, which is less than the relatively stable 45 μW at low pump power levels. When the input increased by 8.5 times, the output increased from 44 μW to only about 110 μW.

The maximum instant output power was 115 μW at an input power of 1.9 mW, while the spot size before the fibre (with a core radius of ~5 μm) was estimated to be 15 μm with NAs in both directions smaller than that of the fibre, corresponding to a coupling geometrical loss of ~56%. Therefore, the extremely low output was not only caused by the defect-induced loss but could also by the

refractive index modification, which degraded coupling efficiency, increased scattering loss, and changed power distribution among different modes. Additionally, the high pump peak power with the fast decay in the output power suggests both single-photon and multi-photon excitation. This was confirmed by the visually observed red emission from NBOHCs (see Figure 7.4b), which was not observable at the beginning.
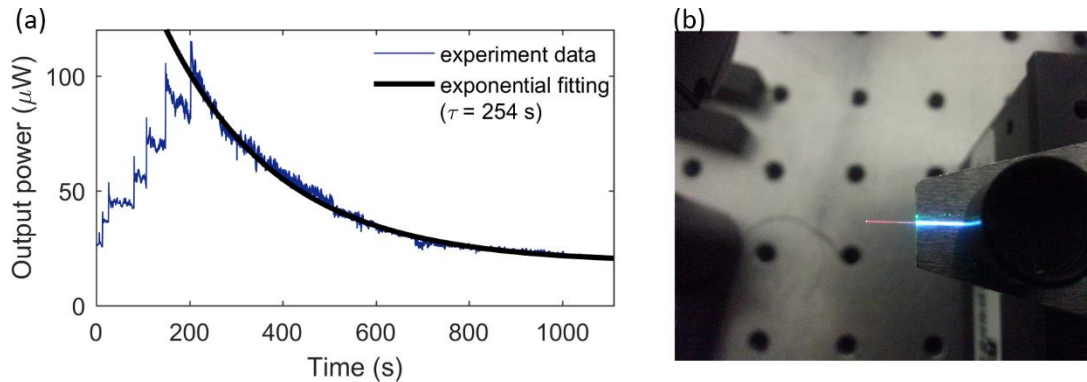


Figure 7.4 (a) Output power from a 60 cm-long untapered Z fibre decreases with time due to femtosecond UV laser modification, and (b) red emission from NBOHC with blue fluorescence generated by leaked light.

A similar result (in Figure 7.5) was obtained with a nanosecond laser from another 60 cm-long Z fibre. The relatively better SNR in Figure 7.5 is due to the use of a different power metre with lower sensitivity and rolling averaged results and due to the relatively stable output at low power. The sharp increases after ~400 s originated from fibre position realignments, because of different high-order modes excited, and because the most damaged section was located at the input coupling point. The realignments reduced the overlap with the generated defects although the beam deviates from the longitudinal axis of the fibre.
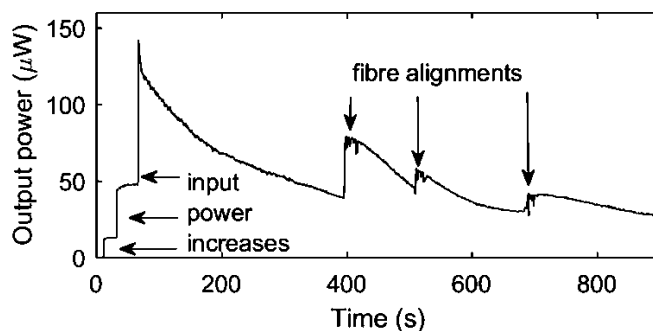


Figure 7.5 Output power from a 60 cm-long untapered Z fibre decreases with time, with an input from a nanosecond UV laser.

The maximum stable power level is comparable with that in Figure 7.4a. However, the nanosecond laser source had an irregular spot shape due to a slightly damaged BBO and was temporarily unavailable for several months; thus, before a pinhole can be applied as a spatial filter for a second photodarkening measurement, quantitative comparison between results from these two sources

with different pulse durations is not recommended. Besides, the irregular beam cross-section leads to lower intensity than that could be achieved using the femtosecond laser with the same focusing setup and thus higher laser threshold power. Moreover, the instability of this nanosecond source at high power levels and a limit in space limited the reliability of laser demonstration, for the lack of precise instant power measurement: a glass slide was applied to generate a reflection for reference, yet its long-term stability and reproducibility were poor. Therefore, further investigation with improved setup and beam quality could be considered for future work.

Replacing the untapered fibre with tapered ones for light coupling into the microspheres further degraded the power to a few microwatts or even worse. This issue might be due to the higher-order modes that were filtered out in the taper transition region and due to the small taper waist, which resulted in high intensity and, subsequently, more defects than that in untapered fibres. Investigation on whether the DUV-induced defects were mostly formed in the pure silica core, the F-doped silica cladding, or in both has been considered. If the core is affected more than the cladding, the loss could be reduced by shortening the untapered fibre pigtail at the input end. However, previous research [121] on defect-related PL from femtosecond (~125fs, 100Hz, 900μJ, $E_{photon}$~1.5eV) written FBGs based on multi-photon absorption in SMF-28 and Z-fibre, suggests that the fluorine doped in the cladding of the Z fibre does not play a large role. Moreover, the photodarkening issue, which originated from the high intensity in the fibre taper waist region, is still inevitable. Also, the handling of a short microfibre is not as convenient as that of coupling with long pigtails, prisms, or waveguides. Therefore, an alternative pump configuration based on free-space coupling was then considered.

## 7.4     UV generation in Gd-doped silica microspheres

### 7.4.1      Pumping scheme

In free-space coupling, the pump beam in free space was focused on the edge of the microsphere. With this pumping scheme, WGM can be excited in liquid droplets and solid microspheres, though not as efficiently as with micro-fibres or prisms. The localisation principle [172] links the mode number of a specific WGM to the position of a Gaussian beam relative to the sphere centre. Previous studies in the literature have verified theoretically the validity of free-space coupling for circular and deformed micro-cavities [46]. In [164], van de Hulst localization principle was experimentally proved for high-order modes, while for low-order modes, the optimal beam position was located inside the sphere rim, which contradicts the localization prediction. However, WGM was still efficiently excited in the latter case, and this was attributed to surface irregularity-induced scattering and diffraction. The authors also theoretically assessed the relation between the optimal

beam position and the surface perturbation, which is likely the dominant coupling pathway for surface-limited modes in large (>20 μm in diameter) spheres. In [173], based on the same coupling method, an extinction ratio of 5 dB was observed. Although the Q factor was limited by the material to around 6 x 10$^3$, for a sphere radius of 390 μm, the theoretical coupling Q factor reported reaches 10$^{17}$ to 10$^{21}$, depending on the beam position. In [169], by focusing a Nd:YAG pulsed laser to the edge of a Tm$^{3+}$-doped ZBLAN microsphere, three-photon-excited lasing emission at 480 nm and 800 nm were observed, with threshold power of 20 mW and 4 mW, respectively.

## 7.4.2    Experiment setup

The Gd-based UV generation experiment started with the setup for the SH generation. As illustrated in Figure 7.6a, the SH pump beam was focused tightly, using two lenses, to the edge of a microsphere, through a pinhole and a tube set before the power detector to remove additional green laser spots reflected from the back sides of the dichroic mirrors and to minimise background noise. The power was taken before the last lens with a transmission above 90%. The spot size before the sample was estimated to be 8 μm, with a distance of 0.2 mm, which is less than the Rayleigh ranges, between the focal points in horizontal and vertical directions. The pump wavelength was tuned to maximise the signal-to-pump ratio.
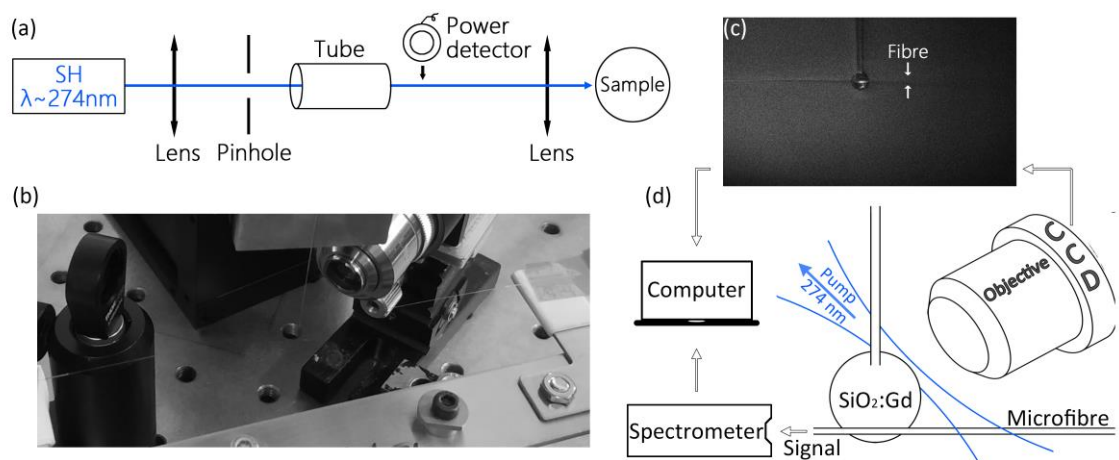


Figure 7.6 Schematic diagram of the experiment setup: (a) pump source and (d) pumping and detection system, with (c) a CCD image of the microsphere and microfibre samples. (b) A photograph of the pumping scheme.

Light emitted from excited Gd$^{3+}$ ions was collected by a microfibre and guided to a spectrometer (HR4000, OceanOptics). The output coupling coefficient depends on the overlap between the whispering gallery and fibre modes, the interaction length, and the phase-matching within the interaction region. A low output coupling loss is desirable to reduce the threshold power and minimise the amount of defects created by unabsorbed pump light coupled into the microfibre. Although single-mode operation allows a straightforward interpretation, it requires a fibre

diameter less than 0.22 μm which is challenging to handle. The diameter and length of the microfibre used in the experiment were 1.55 μm (see Figure 7.7) and ≲ 2 mm, respectively, although the designed parameters were 1 μm and 4mm, respectively. The fabrication errors could be related to the airflow and the old ceramic heater used for tapering. The relatively large diameter microfibre ensured a negligible coupling between the fundamental modes and collected a minimal amount of scattered signals. WGMs with relatively high output coupling loss could not lase, as mentioned in Section 6.2. The exact output coupling efficiency also depended on where the microsphere was set along the tapered fibre.
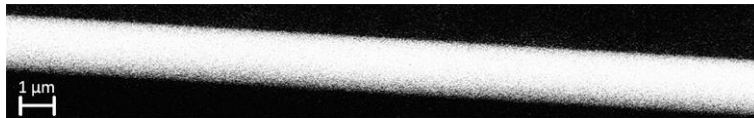


Figure 7.7 SEM image showing the size of a microfibre used.

The sample position relative to the focal points was aligned and fine-tuned according to the transmitted beam profile, the CCD images taken via an objective, and the output signal intensity. The distance between the fibre and the microsphere was reduced gradually, and no signal was observed at the emission wavelength until they suddenly touched each other under electrostatic force. This is because the short wavelengths in contrast to the large microsphere radius led to short evanescence field tails and small modal overlaps between the fibre and the microsphere modes. This contact was confirmed by launching red light from a fibre fault locator to the microfibre. The brightness of scattered red light changed when the fibre touched the sample. This contact maintained by the electrostatic force during the experiment reduced the influence of environmental vibration on the setup stability and the coupling efficiency. This influence could otherwise be noisy, especially when the setup is not fully isolated.

### 7.4.3 Experiment results

Figure 7.8 shows the emission spectra from a 28.8-μm-radius microsphere at different incident pump power. The redshift of the central wavelength $\lambda \approx 315$ nm, compared with the PL spectra presented in Chapter 5, is larger than that which can be explained by the calibration errors of the two spectrometers used. The alignment at the beginning was performed at low pump power, where the initial emission band of some samples centred at $\lambda \approx 314$ nm; thus, at present, the shift is believed to be caused by microsphere fabrication processes and the UV pump light, which modified the local environment of $Gd^{3+}$ ions and also increased material loss. To avoid issues induced by this power-dependent loss during the experiment, in the beginning the pump power was carefully increased to a relatively high value (e.g. 4.5 mW in this experiment), at which the UV-induced loss was stabilised and the output stability was ensured. Then the spectra recording was started from

low power levels, and the setup stability was confirmed by reproduction of the result at the highest pump power at the end.
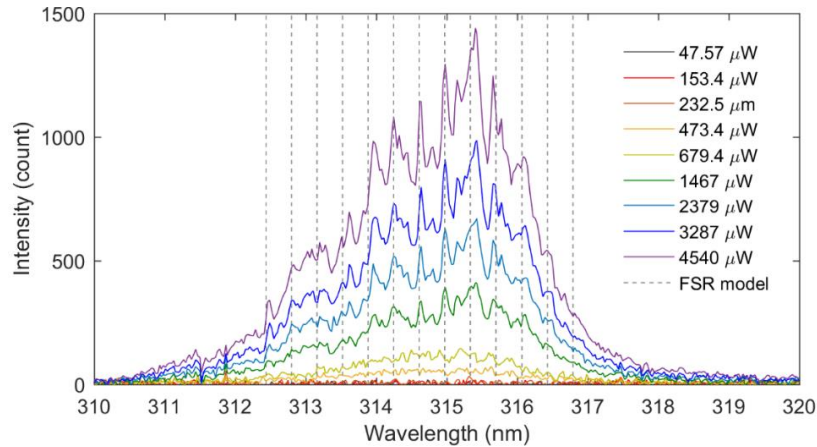


Figure 7.8 Emission spectra of a 28.8-μm-radius Gd-doped silica microsphere at different incident pump power measured before the microsphere. Theoretical free spectral range is indicated by dotted lines.

Individual emission lines are not resolvable due to multimode operation resulting from scattering- and diffraction-based pumping mechanism and to the limited spectrometer resolution. During the experiment, no obvious spectral broadening was observed with time or when the spectral profile changed due to dust or high pump power; these confirm that the detected spectra do not embody information on the exact linewidth of each resonance.

The theoretical free spectral range (FSR) can be estimated using a familiar equation (i.e. $\Delta\lambda \approx \lambda^2/2\pi R_s n_s$). With the refractive index of silica at 314nm being $n_s = 1.4839$, $R_s = 28.8$ μm and $\lambda = 315$ nm, the FSR is $\Delta\lambda \approx 0.37$ nm. This can also be determined using the characteristic equation in Section 2.1.2, the results of which are plotted as the dotted lines in Figure 7.8. The recorded FSR is around 0.36 nm and is in agreement with the theoretical prediction. Aside from those less than the spectrometer resolution, the mismatches could be related to the exact modes excited: the peaks at 315.41 nm, 313.96 nm and 313.62 nm were 0.07 nm, 0.07 nm and 0.09 nm away from the prediction and all 'shift' in the same direction, while the spacing between for example $TE_l$ and $TM_{l-1}$ in theory is 0.096 nm. It can be found that due to the long perimeter, in contrast with the wavelength, a slight modification in the refractive index caused by the UV can shift the resonant wavelength by multi-FSR, almost without changing the FSR. For this reason, mode assignment to exact mode orders is challenging.

As the power detector employed covered a wide spectral range from 200nm to 1100nm, the output spectrum at long wavelengths was examined prior to power measurement. The result (see Figure 7.9) confirms the existence of red emission from NBOHC and green laser residue. To avoid their influence on output power measurement, the microfibre output pigtail was spliced to 1 metre of bent SM300 fibre employed as a short-pass filter. The effect of the pump at 274 nm could then be

cancelled according to the pump-to-signal ratio and the sensitivity of the spectrometer. However, after the spectrometer was replaced with the power meter, no signal was detected, suggesting an output power of less than 0.5 nW. Besides the degradation of less than one order of magnitude caused by the core diameter mismatch between the SM300 and the Z fibre, the low output was mainly caused by the low output coupling efficiency. Note that in other cases, a low output can also arise from defects in fibres created by lossy higher-order modes that cannot lase and from higher-order fibre modes dissipated in the tapering region.
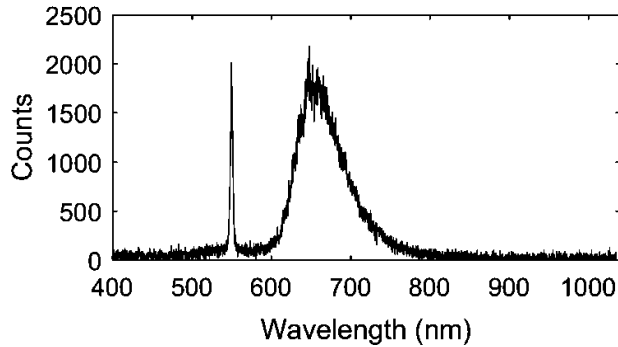


Figure 7.9 Output spectrum in the visible and IR taken with Ocean Optics USB4000 spectrometer (with slit size = 25 μm and resolution = 1.426 nm). Note that the FSR at λ = 650 nm is 1.6 nm and comparable with the spectrometer resolution.

### 7.4.4    Analysis

For the reasons mentioned above, the response of the output to the pump is analysed based on the spectra. The total output (i.e. the integration over the emission band) is plotted as a function of the average pump power in the UV measured before the sample. The results in Figure 7.10a exhibits a change in the slope efficiency with increasing pump power − one of the signature characteristics of lasing action − and indicates a threshold power of 237 ± 30 μW. The standard error is given by the fitting.
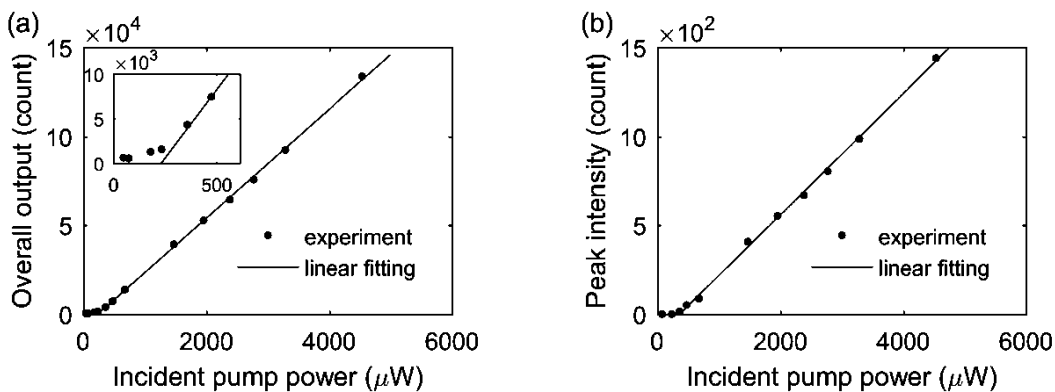


Figure 7.10 Dependence of (a) the overall output within the emission band and (b) the intensity at the peak wavelength on the incident pump power measured before the microsphere, based on in total thirteen measurements.

Figure 7.10b is the same plot but for a single peak at $\lambda$ = 315.4 nm. A different threshold power of 359 ± 39 µW implies multimode operation with the threshold varied from mode to mode. It should be noted that because of the limited spectral resolution, the threshold indicated in Figure 7.10b is from data collected by one pixel of the CCD and thus could be also associated with multiple modes and different from the laser threshold of each mode in the case of single-mode operation.

Analogous to FP cavities, the threshold pump absorption in the microsphere laser is modelled using Equation (6.5). The mode volume is estimated according to the microsphere perimeter and the laser fundamental mode 1/e waists in polar and radial directions which are assumed to be independent of the azimuthal coordinate. The microsphere circumference $R_1$ is set to 1 as the light passes the output coupling point only once per round trip. The results illustrated in Figure 7.11 suggest the threshold pump absorption is of the order of several microwatts.
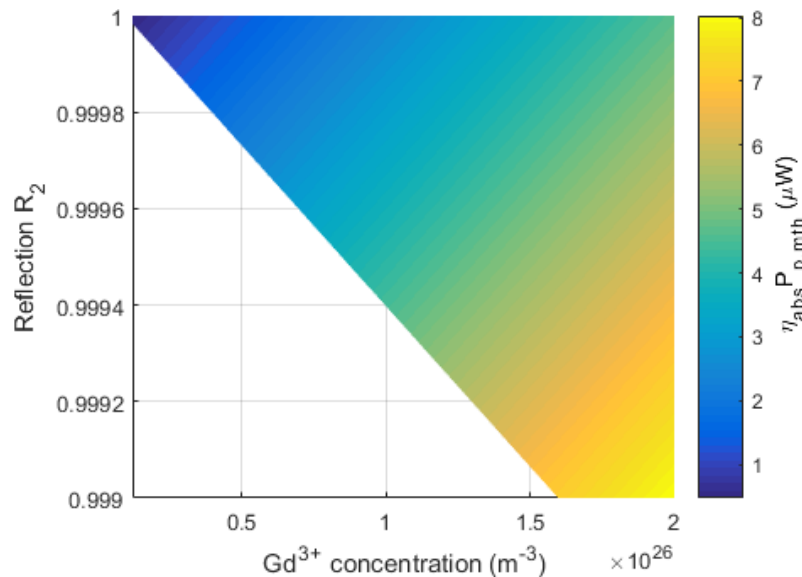


Figure 7.11 Theoretical minimum pump threshold, varying with output coupling and dopant concentration.

Power measurement after the microsphere, with the absence of the microfibre, suggests transmission of less than 75%, corresponding to total loss and absorption of 60 µW (or 90 µW) at the threshold of Figure 7.10a (or Figure 7.10b), which is considerably higher than the theoretical prediction in Figure 7.11. The extremely low pump efficiency is believed to be mainly caused by the low-efficiency free-space pumping scheme ($\eta_s$) and material loss ($\eta_l$), and partly due to the overlap between the pump emission and the gain medium absorption bands ($\eta_f$). First, the measurement of the exact pump power absorbed by Gd³⁺ ions was not feasible. The difference in the pump power before and after the microsphere arose not only from Gd absorption but also from scattering and reflection loss and material loss dominated by the defects. Although in the experiment there was no observable or detectable scattering signal, the integration over the full solid angle was not available and thus the exact absorption could not be quantified. Second, the ratio between Gd

absorption and material loss considered in the modelling was evaluated with doped phosphosilicate fibre sample A which differs from the doped silica sample B. The exact material loss was affected by the microsphere fabrication process and further increased due to UV-induced modification in the lasing experiment. Fabrication using a $CO_2$ laser could also modify the concentration and change $Gd^{3+}$ decay lifetime. Therefore, the amount of scattered light coupled into WGMs and finally absorbed by Gd was less than the measured value. Third, the free-space input coupling led to the excitation of higher-order WGMs with large mode volume and thus high threshold pump power. In addition, the emission propagated in both clockwise and counter-clockwise modes, which doubled the number of lasing modes.

It is worth noting that, in the modelling results for the fundamental mode, changes of a few hundredths of a per cent in R would make laser operation infeasible, because the round-trip loss is higher than the maximum gain associated to the specific dopant concentration. This is also applicable to other modes. However, even if the low-order modes in the equator plane are suppressed, higher-order modes and, depending on the pump distribution inside the sphere, the modes in other planes with relatively less overlaps with the modes in the microfibre and thus with low output coupling losses can still be excited. For the 28.8-μm-radius sample, due to the short evanescent tail and the phase mismatch between the WGMs and the fibre modes, only minimal amount of scattered light was collected with an output power less than 0.5 nW.

The effect of excited-state absorption on pump efficiency is not discussed here, not only because of lack of information on the transitions from $^6P_J$ and $^6I_J$ levels to high-energy levels but also because the possible subsequent emission in the red (or the IR) given by $^6G_{2/7} \rightarrow {}^6P_J$ (or $^6G_{2/7} \rightarrow {}^6I_J$) transition was not observed during the experiment (see Figure 7.9). Output characterisation of laser dynamics is recommended for future work as it can be another approach to confirm the lasing action [174].

Free-space coupling to WGMs is low efficient compared with that achieved with microfibres, gratings, or prisms. Here, the coupling could arise from defects and surface perturbation introduced during fabrication. It was also affected by UV modification in the glass, which varied from sample to sample, resulting in poor reproducibility, thus making it difficult to investigate the exact coupling mechanism. Moreover, due to the low pump coupling efficiency and pump source stability limited by a software issue for remote control, only a few results with changes in slope efficiency at the peaks were observed; however, spectrum recording of most of them was not completed successfully. For example, Figure 7.12 shows results from a 45 μm-radius microsphere. The spacing between the main resonant peaks matches with the theoretical FSR = 0.24 nm. It is evident that the output at $\lambda$ = 314.3 nm grows at a different rate than that at adjacent peak wavelengths and, at low pump power levels, is dominated by multiple modes. The values at high power levels suggest a

threshold of around 241 µW, while the dependence of the overall output within the emission band on the pump power does not lead to a reliable threshold, which can be a consequence of multimode operation. Precise results require additional measurements at different pump levels. However, the spectrum taken at the highest pump power 5.7 mW is not reproduced at the end and exhibits a different profile than others at 314 nm. This can be caused by (i) possible pump and setup instability, which changed pump power distribution inside the sample as well as the mode competition dynamics, or (ii) possible contamination from the air, increasing the absorption and scattering loss of some modes. To avoid these detrimental factors that hindered the experiment measurements, a remote-controlled isolation system and, again, improvements in photodarkening resistance are recommended for future work.
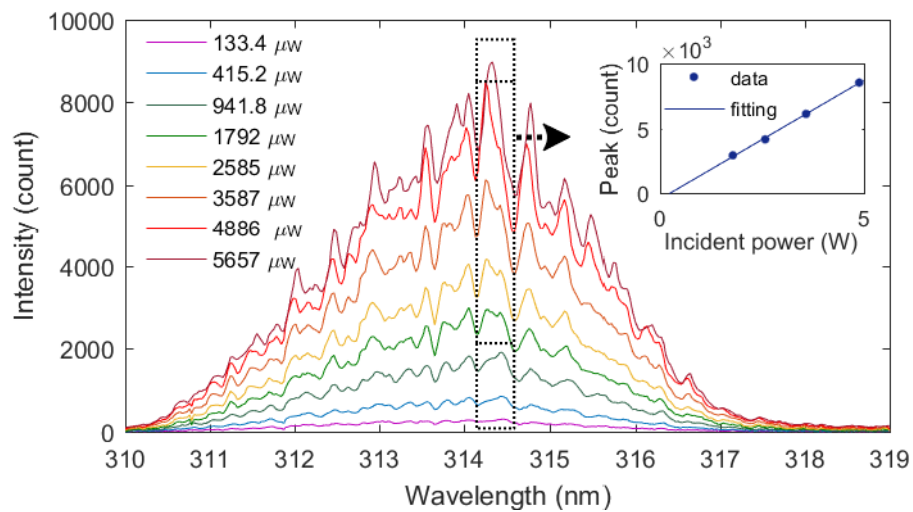


Figure 7.12 Emission spectra of a 45 µm-radius Gd-doped silica microsphere at different incident pump power measured before the microsphere. The inset shows the peak output at λ ≈ 314.3 nm as a function of the incident pump power.

## 7.5    Summary

Taking advantage of its low laser threshold, a microsphere laser was considered prior to the fibre laser demonstration. Microspheres with different diameters were fabricated from Gd-doped fibre samples. Coupling the pump into WGMs was hindered by photodarkening occurring in the power delivery fibre; therefore, a free-space pumping scheme was considered. Despite its low coupling efficiency, changes in the slope efficiency were observed at pump power above 200 µW, two orders of magnitude higher than the prediction. The difference was mainly caused by the low-efficiency free-space pumping scheme and material loss. Repeating the experiment in a dust-free environment is recommended after photodarkening issue can be solved.

# Chapter 8     Conclusions

## 8.1  Summary

The present study focuses on the UV generation in silica glass. Two approaches have been theoretically and experimentally investigated using a submarine telecom optical fibre and Gd-doped silica/phosphosilicate fibres and microspheres.

After the introduction and background chapters, the sixth-harmonic generation of deep UV light from a pump at $\lambda$ = 1550 nm was simulated and experimentally demonstrated in a fully fiberised system in Chapter 3. The temporal walk-off was minimised by using a nanosecond pulse laser as a pump source. Material absorption in the UV was minimised by using fibres with F-doped claddings and pure silica cores. A power of 0.15 nW was recorded at a wavelength of 259 nm, which could be further increased by orders of magnitude by optimising the taper profile and by improving the pumping and detection methods.

The other approach, presented in Chapters 4–7, benefits from the spectroscopic properties of the rare earth ion $Gd^{3+}$; three silica fibres doped with Gd were characterised in the present study. Absorption from $Gd^{3+}$ was observed at the wavelengths in agreement with well-known energy level diagrams reported in the literature. The $Gd^{3+}$-induced absorption at the pump wavelength was characterised using an LED, providing an estimated absorption cross section of 4.44 x $10^{-21}$ $cm^2$. Hydrogen loading has been trialled to remove the NBOHCs initially presented in the samples and confirmed to be able to passivate the defects induced by the femtosecond laser.

The luminescence generated by the $^6P_{7/2} \rightarrow {}^8S_{7/2}$ transition in the Gd-doped fibre was observed with various UV pump sources, including an femtosecond laser, a UV LED source and a lamp. The photoluminescence spectra of optical fibre bundles and fibre preforms were recorded and showed emissions at 312 nm and 314 nm in the doped phosphosilicate and doped silica, respectively, when pumping to the $Gd^{3+}$ $^6D_J$, $^6I_J$ and $^6P_{J=5/2, 3/2}$ energy levels. Light emission from oxygen-deficient centres were observed in samples produced by solution doping, whereas their wide absorption bands centred at $\lambda \approx$ 250 nm do not affect pumping to the $^6I_J$ states. Photoluminescence and photoluminescence excitation spectra before and after fibre drawing have shown that phosphosilicate and pure silica samples doped with $Gd^{3+}$ are optically active in the UV with emission observed at $\lambda_{em}$~ 312 and 314 nm when the samples are pumped at $\lambda_{ex}$ ~ 272.5 nm or 252 nm in the phosphosilicate sample and $\lambda_{ex}$ ~ 274 nm or 253 nm in the silica sample, respectively.

Due to the weak luminescence signal and a lack of suitable pump sources and amplifiers when the present research was carried out, lifetime measurements were not successful; thus to estimate the laser threshold power, information available in the literature was considered. By taking advantage of its low laser threshold, a microsphere laser was investigated prior to optical fibre lasers. To circumvent the photodarkening occurring in the power delivery fibre, a free-space pumping scheme was adopted. Despite its low coupling efficiency, changes in the slope efficiency were observed at pump power above 200 µW.

Although the output power is not comparable to that which can be obtained with most UV sources available in the market, the results in the present study pave the way towards the practical application of silica-based UV sources with excellent beam quality or high spatial localisation as well as the manufacture of UV fibre lasers. Moreover, the weak luminesce signal from Gd-doped silica glass can also be applied for practical applications, for example, a remote X-ray dose monitor.

## 8.2  Outlook

Since the research in Chapters 6 and 7 with a provisional pump source was carried out within a limited time, possible improvement in the current work shall be considered first. On the one hand, it is recommended to perform microsphere laser experiments in a dust-free environment to prevent measurements from being affected by particles falling on the samples, which changes cavity quality factors as well as laser dynamics. On the other hand, other pumping schemes using, for example, a prism instead of a microfibre would facilitate sample handling during the experiment and also benefit for potential application in liquid environments.

Future work should include the measurement of decay lifetime and the reduction of radiation-induced defects. The pump wavelength is within the transparent window of silica glass. Although the Gd dopants, which are impurities to the original SI-O structures, shift the absorption bandgap, according to the measured bandgap of the samples, it is possible to minimise the photodarkening issue by employing continuous-wave pump sources with low peak power. Therefore, it is recommended to further investigate the effects of continuous-wave UV light at ~274 nm on the defect-related material absorption. Moreover, the pilot fabrication of the first Gd-doped silica fibres has room for optimisation in terms of material transparency in the UV region.

Furthermore, although the work in this thesis is restricted to Gd-doped step-index fibres, it would be worth examining other fibre structures, such as hollow-core fibre filled with rare earth ions in gas form or hydrogen to reduce the formation of defects.

# Appendix A

# List of Publications

## A.1    Journal articles

1.      Y. Wang, T. Lee, F. De Lucia, M. I. M. Abdul Khudus, P. J. A. Sazio, M. Beresna, and G. Brambilla, "All-fiber sixth-harmonic generation of deep UV," Opt. Lett. **42**, 4671 (2017).

2.      Y. Wang, J. He, P. Barua, N. Chiodini, S. Steigenberger, M. I. M. Abdul Khudus, J. K. Sahu, M. Beresna, and G. Brambilla, "Ultraviolet photoluminescence in Gd-doped silica and phosphosilicate fibers," APL Photonics **2**, 046101 (2017).

3.      "UV generation in Gd-doped silica microspheres" (to be submitted)

## A.2    Conference and workshop papers

1.      Y. Wang, M. Zervas, and G. Brambilla, "Optical nanofibers with gold nano-aperture antenna for sensing," in *The 4th International Workshop on Optical Nanofiber Applications (ONNA 2016)* (2016).

2.      Y. Wang, J. He, P. Barua, N. Chiodini, S. Steigenberger, M. I. M. A. Khudus, J. K. Sahu, M. Beresna, and G. Brambilla, "UV luminescence in Gd-doped silica and phosphosilicate optical fibers," in 2017 Conference on Lasers and Electro-Optics Pacific Rim (CLEO-PR) (IEEE, 2017), pp. 1–3.

# Bibliography

1.  K. Song, M. Mohseni, and F. Taghipour, "Application of ultraviolet light-emitting diodes (UV-LEDs) for water disinfection: A review," Water Res. **94**, 341–349 (2016).

2.  T. Bintsis, E. Litopoulou-Tzanetaki, and R. K. Robinson, "Existing and potential applications of ultraviolet light in the food industry - A critical review," J. Sci. Food Agric. **80**, 637–645 (2000).

3.  A. Endruweit, M. S. Johnson, and A. C. Long, "Curing of composite components by ultraviolet radiation: A review," Polym. Compos. **27**, 119–128 (2006).

4.  M. Han, W. Lee, S. K. Lee, and S. S. Lee, "3D microfabrication with inclined/rotated UV lithography," Sensors Actuators, A Phys. **111**, 14–20 (2004).

5.  J. M. Hoffman, A. K. Hays, and G. C. Tisone, "High power uv noble-gas-halide lasers," Appl. Phys. Lett. **28**, 538–539 (1976).

6.  H. M. Pask, P. Dekker, R. P. Mildren, D. J. Spence, and J. A. Piper, "Wavelength-versatile visible and UV sources based on crystalline Raman lasers," Prog. Quantum Electron. **32**, 121–158 (2008).

7.  G. K. Samanta, S. C. Kumar, A. Aadhi, and M. Ebrahim-Zadeh, "Yb-fiber-laser-pumped, high-repetition-rate picosecond optical parametric oscillator tunable in the ultraviolet," Opt. Express **22**, 11476–11487 (2014).

8.  M. Yoshimura, Y. Takahashi, H. Adachi, and Y. Mori, "Nonlinear Crystals for Deep-UV Light Generation," in *Advanced Solid State Lasers, OSA Technical Digest (Online)* (Optical Society of America, 2014), p. ATu4A.1.

9.  Y. Urata, T. Shinozaki, Y. Wada, Y. Kaneda, S. Wada, and S. Imai, "Deep UV light generation by a fiber/bulk hybrid amplifier at 199 nm.," Appl. Opt. **48**, 1668–1674 (2009).

10.  J. H. Kim, M.-K. Chen, C.-E. Yang, J. Lee, S. S. Yin, P. Ruffin, E. Edwards, C. Brantley, and C. Luo, "Broadband IR supercontinuum generation using single crystal sapphire fibers," Opt. Express **16**, 4085–4093 (2008).

11.  S. P. Stark, J. C. Travers, and P. S. J. Russell, "Extreme supercontinuum generation to the deep UV," Opt. Lett. **37**, 770–772 (2012).

12.  M. Shatalov, W. Sun, R. Jain, A. Lunev, X. Hu, A. Dobrinsky, Y. Bilenko, J. Yang, G. A. Garrett, L. E. Rodak, M. Wraback, M. Shur, and R. Gaska, "High power AlGaN ultraviolet light emitters," Semicond. Sci. Technol. **29**, 84007 (2014).

13.  Sensor Electronic Technology Inc., "Total UV solution provider: Seoul Viosys and SETi," http://www.s-et.com/en/product/SETi.pdf.

14.  J. Limpert, F. Röser, S. Klingebiel, T. Schreiber, C. Wirth, T. Peschel, R. Eberhardt, and A. Tünnermann, "The rising power of fiber lasers and amplifiers," IEEE J. Sel. Top. Quantum Electron. **13**, 537–544 (2007).

15.  M. N. Zervas and C. A. Codemard, "High power fiber lasers: A review," IEEE J. Sel. Top. Quantum Electron. **20**, 219–241 (2014).

16.  E. Gabryte, S. Sobutas, M. Vengris, and R. Danielius, "Control of thermal effects in fast-

switching femtosecond UV laser system," Appl. Phys. B Lasers Opt. **120**, 31–39 (2015).

17.    G. H. Siegel, "Ultraviolet spectra of silicate glasses: A review of some experimental evidence," J. Non. Cryst. Solids **13**, 372–398 (1974).

18.    Fiberguide Industries Limited, "Solarguide$^{TM}$ Solarization Resistant UV FIber," https://www.fiberguide.com/wp-content/uploads/2012/09/Solarguide_090712.pdf.

19.    T. Lee, Y. Jung, C. a. Codemard, M. Ding, N. G. R. Broderick, and G. Brambilla, "Broadband third harmonic generation in tapered silica fibres," Opt. Express **20**, 8503–8511 (2012).

20.    M. I. M. Abdul Khudus, F. De Lucia, C. Corbari, T. Lee, P. Horak, P. Sazio, and G. Brambilla, "Phase matched parametric amplification via four-wave mixing in optical microfibers," Opt. Lett. **41**, 761–764 (2016).

21.    W. Miniscalco, "Optical and electronic properties of rare earth ions in glasses," in *Rare-Earth-Doped Fiber Lasers and Amplifiers, Revised and Expanded*, M. J. F. Digonnet, ed., 2nd ed. (CRC Press, 2001).

22.    M. J. F. Digonnet, *Rare-Earth-Doped Fiber Lasers and Amplifiers, Revised and Expanded*, Second Edi (CRC Press, 2001).

23.    E. Williams, E. B. Brousseau, and A. Rees, "Nanosecond Yb fibre laser milling of aluminium: effect of process parameters on the achievable surface finish and machining efficiency," Int. J. Adv. Manuf. Technol. **74**, 769–780 (2014).

24.    J. Gabzdyl, "Materials processing: Fibre lasers make their mark," Nat. Photonics **2**, 21–23 (2008).

25.    R. A. McFarlane, "High-power visible upconversion laser," Opt. Lett. **16**, 1397–1399 (1991).

26.    J. Y. Allain, M. Monerie, and H. Poignant, "Room temperature CW tunable green upconversion holmium fibre laser," Electron. Lett. **26**, 261–263 (1990).

27.    P. Xie and T. R. Gosnell, "Room-temperature upconversion fiber laser tunable in the red, orange, green, and blue spectral regions," Opt. Lett. **20**, 1014–1016 (1995).

28.    A. W. Kueny, W. E. Case, and M. E. Koch, "Infrared-to-ultraviolet photon-avalanche-pumped upconversion in Tm:LiYF$_4$," J. Opt. Soc. Am. B **10**, 1834–1839 (1993).

29.    H. W. Gandy and R. J. Ginther, "Stimulated emission of ultraviolet radiation from gadolinium-avtivated glass," Appl. Phys. Lett. **1**, 25–27 (1962).

30.    H. El hamzaoui, G. Bouwmans, B. Capoen, A. Cassez, R. Habert, Y. Ouerdane, S. Girard, D. Di francesca, N. Kerboub, A. Morana, D. Söderström, A. Boukenter, and M. Bouazaoui, "Gd$^{3+}$-doped sol-gel silica glass for remote ionizing radiation dosimetry," OSA Contin. **2**, 715–721 (2019).

31.    M. L. Gorodetsky, A. A. Savchenkov, and V. S. Ilchenko, "Ultimate Q of optical microsphere resonators," Opt. Lett. **21**, 453–455 (1996).

32.    D. W. Vernooy, V. S. Ilchenko, H. Mabuchi, E. W. Streed, and H. J. Kimble, "High-Q measurements of fused-silica microspheres in the near infrared," Opt. Lett. **23**, 247–249 (1998).

33.    V. Sandoghdar, F. Treussart, J. Hare, V. Lefèvre-Seguin, J. M. Raimond, and S. Haroche, "Very low threshold whispering-gallery-mode microsphere laser," Phys. Rev. A **54**, R1777–R1780 (1996).

34.   F. Vollmer and S. Arnold, "Whispering-gallery-mode biosensing: Label-free detection down to single molecules," Nat. Methods **5**, 591–596 (2008).

35.   A. W. Snyder and J. D. Love, *Optical Waveguide Theory* (Springer US, 1984).

36.   K. Okamoto, *Fundamentals of Optical Waveguides*, Second Edi (Academic Press, 2006).

37.   E. Snitzer, "Cylindrical Dielectric Waveguide Modes," J. Opt. Soc. Am. **51**, 491–498 (1961).

38.   G. Brambilla, "Optical fibre nanotaper sensors," Opt. Fiber Technol. **16**, 331–342 (2010).

39.   G. Brambilla, Y. Jung, and F. Renna, "Optical fiber microwires and nanowires manufactured by modified flame brushing technique: Properties and applications," Front. Optoelectron. China **3**, 61–66 (2010).

40.   J. D. Love, W. M. Henry, W. J. Stewart, R. J. Black, S. Lacroix, and F. Gonthier, "Tapered single-mode fibres and devices. Part 1: Adiabaticity criteria," IEE Proc. J Optoelectron. **138**, 343–354 (1991).

41.   Y. Jung, G. Brambilla, and D. J. Richardson, "Broadband single-mode operation of standard optical fibers by using a sub-wavelength optical wire filter," Opt. Express **16**, 14661–14667 (2008).

42.   A. N. Oraevsky, "Whispering-gallery waves," Quantum Electron. **32**, 377–400 (2002).

43.   B. E. Little, J. P. Laine, and H. A. Haus, "Analytic theory of coupling from tapered fibers and half-blocks into microsphere resonators," J. Light. Technol. **17**, 704–715 (1999).

44.   J. C. Knight, G. Cheung, F. Jacques, and T. A. Birks, "Phase-matched excitation of whispering-gallery-mode resonances by a fiber taper," Opt. Lett. **22**, 1129–1131 (1997).

45.   V. S. Ilchenko, D. S. Starodubov, M. L. Gorodetsky, L. Maleki, and J. Feinberg, "Coupling light from a high-Q microsphere resonator using a UV-induced surface grating," in *Technical Digest. Summaries of Papers Presented at the Conference on Lasers and Electro-Optics. Postconference Edition. CLEO '99. Conference on Lasers and Electro-Optics (IEEE Cat. No.99CH37013)* (Opt. Soc. America, 2006), Vol. 3, p. 67.

46.   C.-L. Zou, F.-J. Shu, F.-W. Sun, Z.-J. Gong, Z.-F. Han, and G.-C. Guo, "Theory of free space coupling to high-Q whispering gallery modes," Opt. Express **21**, 9982–9995 (2013).

47.   Y.-F. Xiao, C.-H. Dong, C.-L. Zou, Z.-F. Han, L. Yang, and G.-C. Guo, "Low-threshold microlaser in a high-Q asymmetrical microcavity," Opt. Lett. **34**, 509–511 (2009).

48.   D. A. Akimov, A. A. Ivanov, A. N. Naumov, O. A. Kolevatova, M. V. Alfimov, T. A. Birks, W. J. Wadsworth, P. S. J. Russell, A. A. Podshivalov, and A. M. Zheltikov, "Generation of a spectrally asymmetric third harmonic with unamplified 30-fs Cr:forsterite laser pulses in a tapered fiber," Appl. Phys. B Lasers Opt. **76**, 515–519 (2003).

49.   V. Grubsky and A. Savchenko, "Glass micro-fibers for efficient third harmonic generation.," Opt. Express **13**, 6798–6806 (2005).

50.   V. Grubsky and J. Feinberg, "Phase-matched third-harmonic UV generation using low-order modes in a glass micro-fiber," Opt. Commun. **274**, 447–450 (2007).

51.   M. Delgado-Pinar, Y. Li, D. M. Bird, T. A. Birks, and W. J. Wadsworth, "Third Harmonic Generation in Uniform Fibre Nanotapers via Intermodal Coupling," in *Conference on Lasers and Electro-Optics 2010* (OSA, 2010), p. CWL4.

52.   T. Lee, Y. Jung, C. Codemard, G. Brambilla, and N. G. R. Broderick, "Third Harmonic Generation in Silica Microfibres," in *Nonlinear Optics* (OSA, 2011), p. NTuD7.

53.   M. I. M. A. Khudus, T. Lee, P. Horak, and G. Brambilla, "Effect of intrinsic surface roughness on the efficiency of intermodal phase matching in silica optical nanofibers," Opt. Lett. **40**, 1318–1321 (2015).

54.   R. W. Boyd, *Nonlinear Optics*, Third Edit (Academic Press, 2008).

55.   G. Agrawal, *Nonlinear Fiber Optics*, 5th Editio (Academic Press, 2012).

56.   I. H. Malitson, "Interspecimen Comparison of the Refractive Index of Fused Silica," J. Opt. Soc. Am. **55**, 1205–1209 (1965).

57.   M. I. M. Abdul Khudus, F. De Lucia, C. Corbari, T. Lee, P. Horak, P. Sazio, and G. Brambilla, "Four-wave mixing UV generation in optical microfibers," in *Proc. SPIE 9894, Nonlinear Optics and Its Applications IV* (2016), p. 98941I.

58.   M. A. Gouveia, T. Lee, R. Ismaeel, M. Ding, N. G. R. Broderick, C. M. B. Cordeiro, and G. Brambilla, "Second harmonic generation and enhancement in microfibers and loop resonators," Appl. Phys. Lett. **102**, 201120 (2013).

59.   Covesion Ltd., "Material properties of Lithium Niobate," www.covesion.com/support/covesion-guide-to-ppln/material-properties-of-lithium-niobate.html.

60.   Fiberguide Industries Inc., "High power laser assemblies," www.fiberguide.com/wp-content/uploads/2012/08/HP_Laser_Assemblies_SPEC_SHEET.pdf.

61.   P. G. Kazansky and P. S. J. Russel, "Thermally poled glass: frozen-in electric field or oriented dipoles?," Opt. Commun. **110**, 611–614 (1994).

62.   P. G. Kazansky, L. Dong, and P. S. J. Russell, "High second-order nonlinearities in poled silicate fibers," Opt. Lett. **19**, 701–703 (1994).

63.   D. Wong, M. Sceats, Y. Zhao, T. Fujiwara, S. Fleming, and S. Poole, "Electro-optic modulation in germanosilicate fibre with UV-excited poling," Electron. Lett. **31**, 573–575 (1995).

64.   W. Margulis, O. Tarasenko, and N. Myrén, "Who needs a cathode? Creating a second-order nonlinearity by charging glass fiber with two anodes," Opt. Express **17**, 15534–15540 (2009).

65.   F. De Lucia, D. W. Keefer, C. Corbari, and P. J. A. Sazio, "Thermal poling of silica optical fibers using liquid electrodes," Opt. Lett. **42**, 69–72 (2017).

66.   J. A. Armstrong, N. Bloembergen, J. Ducuing, and P. S. Pershan, "Interactions between light waves in a nonlinear dielectric," Phys. Rev. **127**, 1918–1939 (1962).

67.   A. Canagasabey, C. Corbari, Z. Zhang, P. G. Kazansky, and M. Ibsen, "Broadly tunable second-harmonic generation in periodically poled silica fibers.," Opt. Lett. **32**, 1863–1865 (2007).

68.   E. L. Lim, C. Corbari, A. V. Gladyshev, S. U. Alam, M. Ibsen, D. J. Richardson, and P. G. Kazansky, "Multi-Watt All-Fiber Frequency Doubled Laser," in *Advanced Photonics, OSA Technical Digest (Online)* (Optical Society of America, 2014), p. JTu6A.5.

69.   D. S. Hum and M. M. Fejer, "Quasi-phasematching," Comptes Rendus Phys. **8**, 180–198 (2007).

70.   P. G. Kazansky and V. Pruneri, "Electric-field poling of quasi-phase-matched optical fibers," J. Opt. Soc. Am. B **14**, 3170–3179 (1997).

71. G. Xiao, G. Fallah Tafti, A. Zareanborji, A. Ghaznavi, and Q. Zhao, "Measurement of Active Optical Fibers," in *Handbook of Optical Fibers* (Springer Singapore, 2019), pp. 1–38.

72. B. D. Fahlman, *Materials Chemistry* (Springer Netherlands, 2011).

73. B. Hafner, "Energy Dispersive Spectroscopy on the SEM:A Primer," http://www.charfac.umn.edu/instruments/eds_on_sem_primer.pdf.

74. K. I. White, "Practical application of the refracted near-field technique for the measurement of optical fibre refractive index profiles," Opt. Quantum Electron. **11**, 185–196 (1979).

75. R. Salh, "Defect Related Luminescence in Silicon Dioxide Network: A Review," in *Crystalline Silicon - Properties and Uses*, S. Basu, ed. (IntechOpen, 2011), pp. 135–172.

76. T. A. Birks and Y. W. Li, "The Shape of Fiber Tapers," J. Light. Technol. **10**, 432–438 (1992).

77. J. Lægsgaard, "Theory of surface second-harmonic generation in silica nanowires," J. Opt. Soc. Am. B **27**, 1317–1324 (2010).

78. T. Seydel, M. Tolan, B. M. Ocko, O. H. Seeck, R. Weber, E. DiMasi, and W. Press, "Freezing of capillary waves at the glass transition," Phys. Rev. B - Condens. Matter Mater. Phys. **65**, 184207 (2002).

79. J. Jackle and K. Kawasaki, "Intrinsic roughness of glass surfaces," J. Phys. Condens. Matter **7**, 4351–4358 (1995).

80. M. Sumetsky, D. J. DiGiovanni, Y. Dulashko, J. M. Fini, X. Liu, E. M. Monberg, and T. F. Taunay, "Surface nanoscale axial photonics: robust fabrication of high-quality-factor microresonators," Opt. Lett. **36**, 4824–4826 (2011).

81. J. Kirchhof, S. Unger, K.-F. Klein, and B. Knappe, "Diffusion behaviour of fluorine in silica glass," J. Non. Cryst. Solids **181**, 266–273 (1995).

82. K. Shiraki and M. Ohashi, "Scattering property of fluorine-doped silica glasses," Electron. Lett. **28**, 1565–1566 (1992).

83. M. Planck, "Ueber das Gesetz der Energieverteilung im Normalspectrum," Ann. Phys. **309**, 553–563 (1901).

84. N. Bohr, "I. On the constitution of atoms and molecules," London, Edinburgh, Dublin Philos. Mag. J. Sci. **26**, 1–25 (1913).

85. N. Bloembergen, "Solid state infrared quantum counters," Phys. Rev. Lett. **2**, 84–85 (1959).

86. J. S. Chivian, W. E. Case, and D. D. Eden, "The photon avalanche: A new phenomenon in Pr3+-based infrared quantum counters," Appl. Phys. Lett. **35**, 124–125 (1979).

87. O. Svelto, *Principles of Lasers* (Springer US, 2010).

88. G. H. Dieke and H. M. Crosswhite, "The spectra of the doubly and triply ionized rare earths," Appl. Opt. **2**, 675–686 (1963).

89. R. T. Wegh, A. Meijerink, R.-J. Lamminmäki, and Jorma Hölsä, "Extending Dieke's diagram," J. Lumin. **87**–**89**, 1002–1004 (2000).

90. U. Vetter, J. Zenneck, and H. Hofsäss, "Photon cascade luminescence of $Gd^{3+}$ in $GdBaB_9O_{16}$," Appl. Phys. Lett. **83**, 2145–2147 (2003).

91. Z. Yang, J. . Lin, M. . Su, Y. Tao, and W. Wang, "Photon cascade luminescence of $Gd^{3+}$ in

GdBaB$_9$O$_{16}$," J. Alloys Compd. **308**, 94–97 (2000).

92.    Z. Tian, H. Liang, B. Han, Q. Su, Y. Tao, G. Zhang, and Y. Fu, "Photon cascade emission of Gd$^{3+}$ in Na(Y,Gd)FPO$_4$," J. Phys. Chem. C **112**, 12524–12529 (2008).

93.    G. S. A. Voloshinovskii, N. Pidzyrailo, I. Sol'skii, G. Zimmerer, Yu. Romanyshyn, *Luminescence of Gd$^{3+}$ Ions in LiGdP$_4$O$_{12}$ Phosphor* (2004).

94.    N. Chiodini, M. Fasoli, M. Martini, F. Morazzoni, E. Rosetta, R. Scotti, G. Spinolo, A. Vedda, M. Nikl, N. Solovieva, A. Baraldi, R. Capelletti, and R. Francini, "Rare-Earth Doped Sol-Gel Silicate Glasses for Scintillator Applications," Radiat. Eff. Defects Solids **158**, 463–467 (2003).

95.    D. Di Martino, N. Chiodini, M. Fasoli, F. Moretti, A. Vedda, A. Baraldi, E. Buffagni, R. Capelletti, M. Mazzera, M. Nikl, G. Angella, and C. B. Azzoni, "Gd-incorporation and luminescence properties in sol-gel silica glasses," J. Non. Cryst. Solids **354**, 3817–3823 (2008).

96.    D. J. Little, M. Ams, P. Dekker, G. D. Marshall, J. M. Dawes, and M. J. Withford, "Femtosecond laser modification of fused silica: the effect of writing polarization on Si-O ring structure," Opt. Express **16**, 20029–20037 (2008).

97.    M. J. Yuen, "Ultraviolet absorption studies of germanium silicate glasses," Appl. Opt. **21**, 136–140 (1982).

98.    J. E. Townsend, S. B. Poole, and D. N. Payne, "Solution-doping technique for fabrication of rare-earth-doped optical fibres," Electron. Lett. **23**, 329–331 (1987).

99.    O. G. Okhotnikov, *Fiber Lasers* (Wiley-VCH Verlag GmbH & Co. KGaA, 2012).

100.    F. Moretti, N. Chiodini, M. Fasoli, L. Griguta, and A. Vedda, "Optical absorption and emission properties of Gd$^{3+}$ in silica host," J. Lumin. **126**, 759–763 (2007).

101.    W. Hermann, A. Raith, and H. Rau, "Diffusion of fluorine in silica," Berichte der Bunsengesellschaft für Phys. Chemie **91**, 56–58 (1987).

102.    K. Lyytikäinen, S. T. Huntington, A. L. G. Carter, P. McNamara, S. Fleming, J. Abramczyk, I. Kaplin, and G. Schötz, "Dopant diffusion during optical fibre drawing," Opt. Express **12**, 972–977 (2004).

103.    Heraeus Holding GmbH, "High purity fused silica tubes for specialty fiber production," https://www.heraeus.com/media/media/hqs/doc_hqs/products_and_solutions_8/optical_fiber/Fiber_Tubes_EN.pdf.

104.    R. Sen and A. Dhar, "An improved method of fabricating rare earth doped optical fiber," in *Selected Topics on Optical Fiber Technology*, Moh Yasin, S. W. Harun, and H. Arof, eds. (IntechOpen, 2012).

105.    L. Skuja, "Optically active oxygen-deficiency-related centers in amorphous silicon dioxide," J. Non. Cryst. Solids **239**, 16–48 (1998).

106.    H. Imai, K. Arai, H. Imagawa, H. Hosono, and Y. Abe, "Two types of oxyge-deficient centers in synthetic silica glasses," Phys. Rev. B **38**, 772–775 (1988).

107.    M. Engholm and L. Norin, "Preventing photodarkening in ytterbium-doped high power fiber lasers; correlation to the UV-transparency of the core glass.," Opt. Express **16**, 1260–1268 (2008).

108.    K. Tsujikawa, K. Shiraki, M. Ohashi, and M. Tateda, "Scattering property of F and GeO$_2$ codoped silica glasses," Electron. Lett. **30**, 351–352 (1994).

109.   K. Tsujikawa, M. Tateda, K. Shiraki, and M. Ohashi, "Effect of thermal treatment on Rayleigh scattering in silica-based glasses," Electron. Lett. **31**, 1940–1941 (1995).

110.   K. Tajima, M. Ohashi, K. Shiraki, M. Tateda, and S. Shibata, "Low Rayleigh scattering $P_2O_5$-F-$SiO_2$ glasses," J. Light. Technol. **10**, 1532–1535 (1992).

111.   C. F. Bohren and D. R. Huffman, *Absorption and Scattering of Light by Small Particles* (Wiley, 1998).

112.   K. E. Mattsson, "Photo darkening of rare earth doped silica," Opt. Express **19**, 19797–19812 (2011).

113.   M. Oto, S. Kikugawa, T. Miura, M. Hirano, and H. Hosono, "Fluorine doped silica glass fiber for deep ultraviolet light," J. Non. Cryst. Solids **349**, 133–138 (2004).

114.   L. J. Poyntz-Wright and P. S. J. Russell, "Spontaneous relaxation processes in irradiated germanosilicate optical fibres," Electron. Lett. **25**, 478–480 (1989).

115.   N. Moitra, T. Kamei, K. Kanamori, K. Nakanishi, K. Takeda, and T. Shimada, "Recyclable Functionalization of Silica with Alcohols via Dehydrogenative Addition on Hydrogen Silsesquioxane," Langmuir **29**, 12243–12253 (2013).

116.   H. Nishikawa, E. Watanabe, D. Ito, and Y. Ohki, "Decay kinetics of the 4.4-eV photoluminescence associated with the two states of oxygen-deficient-type defect in amorphous $SiO_2$," Phys. Rev. Lett. **72**, 2101–2104 (1994).

117.   A. Martinez, M. Dubov, I. Khrushchev, and I. Bennion, "Direct writing of fibre Bragg gratings by femtosecond laser," Electron. Lett. **40**, 1170–1172 (2004).

118.   L. Skuja, H. Hosono, and M. Hirano, "Laser-induced color centers in silica," in *Proc. SPIE 4347, Laser-Induced Damage in Optical Materials: 2000* (2001).

119.   K. Kajihara, L. Skuja, M. Hirano, and H. Hosono, "Formation and decay of nonbridging oxygen hole centers in $SiO_2$ glasses induced by $F_2$ laser irradiation: In situ observation using a pump and probe technique," Appl. Phys. Lett. **79**, 1757–1759 (2001).

120.   K. Kajihara, L. Skuja, M. Hirano, and H. Hosono, "Diffusion and reactions of hydrogen in $F_2$-laser-irradiated $SiO_2$ glass," Phys. Rev. Lett. **89**, 135507 (2002).

121.   N. Troy, C. W. Smelser, and D. M. Krol, "Role of hydrogen loading and glass composition on the defects generated by the femtosecond laser writing process of fiber Bragg gratings," Opt. Mater. Express **2**, 1663–1670 (2012).

122.   M. Watanabe, S. Juodkazis, H.-B. Sun, S. Matsuo, and H. Misawa, "Luminescence and defect formation by visible and near-infrared irradiation of vitreous silica," Phys. Rev. B **60**, 9959–9964 (1999).

123.   D. L. Griscom, "Diffusion of radiolytic molecular hydrogen as a mechanism for the post-irradiation buildup of interface states in $SiO_2$-on-Si structures," J. Appl. Phys. **58**, 2524–2533 (1985).

124.   J. He, Y. Wang, S. Steigenberger, A. Macpherson, N. Chiodini, and G. Brambilla, "Intense ultraviolet photoluminescence at 314 nm in $Gd^{3+}$-doped silica," in *Conference on Lasers and Electro-Optics* (OSA, 2016), p. JTh2A.86.

125.   G. Pacchioni, L. N. Skuja, and D. L. Griscom, *Defects in $SiO_2$ and Related Dielectrics: Science and Technology* (Springer Netherlands, 2000).

126.   M. Cannas, "Luminescence properties of point defects in silica," in *GNSR 2001: State of Art and Future Development in Raman Spectroscopy and Related Techniques*, G. Messina and S. Santangelo, eds. (IOS Press, 2002), pp. 91–112.

127.   A. Saitoh, S. Matsuishi, C. Se-Weon, J. Nishii, M. Oto, M. Hirano, and H. Hosono, "Elucidation of codoping effects on the solubility enhancement of $Er^{3+}$ in $SiO_2$ glass: Striking difference between Al and P codoping," J. Phys. Chem. B **110**, 7617–7620 (2006).

128.   P. C. Becker, N. A. Olsson, and J. R. Simpson, "Erbium-doped fiber amplifiers Amplifier basics," in *Erbium-Doped Fiber Amplifiers: Fundamentals and Technology* (Academic Press, 1999), pp. 131–152.

129.   G. Kozyreff and N. Acharyya, "Dispersion relations and bending losses of cylindrical and spherical shells, slabs, and slot waveguides," Opt. Express **24**, 28204–28220 (2016).

130.   W. A. Clarkson and D. C. Hanna, "Effects of transverse-mode profile on slope efficiency and relaxation oscillations in a longitudinally-pumped laser," J. Mod. Opt. **36**, 483–498 (1989).

131.   Y. Sato and T. Taira, "Saturation Factors of Pump Absorption in Solid-State Lasers," IEEE J. Quantum Electron. **40**, 270–280 (2004).

132.   W. P. Risk, "Modeling of longitudinally pumped solid-state lasers exhibiting reabsorption losses," J. Opt. Soc. Am. B **5**, 1412–1423 (1988).

133.   T. Y. Fan and Byer, "Modelling and CW operation of a quasi-three-level 946 nm Nd:YAG laser," IEEE J. Quantum Electron. **23**, 605–612 (1987).

134.   P. Solarz, M. Nikl, A. Kłos, R. Lisiecki, W. Ryba-Romanowski, A. Rzepka, S. Ganschow, and A. Pajączkowska, "Luminescence characteristics of undoped and Eu-doped $GdCa_4O(BO_3)_3$ single crystals and nanopowders," Cryst. Res. Technol. **42**, 1308–1313 (2007).

135.   S. H. Nandyala, G. Hungerford, S. Babu, J. L. Rao, I. B. Leonor, R. Pires, and R. L. Reis, "Time resolved emission spectra and electron paramagnetic resonance studies of $Gd^{3+}$ doped calcium phosphate glasses," Adv. Mater. Lett. **7**, 277–281 (2016).

136.   V. Dominic, S. MacCormack, R. Waarts, S. Sanders, S. Bicknese, R. Dohle, E. Wolak, P. S. Yeh, and E. Zucker, "110 W fibre laser," Electron. Lett. **35**, 1158–1160 (1999).

137.   Y. Jeong, J. K. Sahu, D. N. Payne, and J. Nilsson, "Ytterbium-doped large-core fiber laser with 1.36 kW continuous-wave output power," Opt. Express **12**, 6088–6092 (2004).

138.   P. F. Moulton, "Spectroscopic and laser characteristics of $Ti:Al_2O_3$," J. Opt. Soc. Am. B **3**, 125–133 (1986).

139.   R. Paschotta, J. Nilsson, A. C. Tropper, and D. C. Hanna, "Ytterbium-doped fiber amplifiers," IEEE J. Quantum Electron. **33**, 1049–1056 (1997).

140.   D. C. Hanna, R. M. Percival, I. R. Perry, R. G. Smart, P. J. Suni, and A. C. Tropper, "An Ytterbium-doped monomode fibre laser: broadly tunable operation from 1.010μm to 1.162μm and three-level operation at 974nm," J. Mod. Opt. **37**, 517–525 (1990).

141.   R. J. Gehr, M. W. Kimmel, and A. V Smith, "Simultaneous spatial and temporal walk-off compensation in frequency-doubling femtosecond pulses in $\beta$-$BaB_2O_4$," Opt. Lett. **23**, 1298–1300 (1998).

142.   G. D. Boyd and D. A. Kleinman, "Parametric interaction of focused Gaussian light beams," J. Appl. Phys. **39**, 3597–3639 (1968).

143. Michiel .J.A. de Dood, "*Second-Harmonic Generation*, " Huygens Laboratorium 909a (2006).

144. Y. R. Shen, *The Principles of Nonlinear Optics* (John Wiley, 1984).

145. H. Wang and A. M. Weiner, "Efficiency of short-pulse type-I second-harmonic generation with simultaneous spatial walk-off, temporal walk-off, and pump depletion," IEEE J. Quantum Electron. **39**, 1600–1618 (2003).

146. G. A. Ball, W. W. Morey, and W. H. Glenn, "Standing-wave monomode erbium fiber laser," IEEE Photonics Technol. Lett. **3**, 613–615 (1991).

147. M. Shimizu, H. Suda, and M. Horiguchi, "High-efficiency Nd-doped fibre lasers using direct-coated dielectric mirrors," Electron. Lett. **23**, 768–769 (1987).

148. K. O. Hill, B. Malo, F. Bilodeau, D. C. Johnson, and J. Albert, "Bragg gratings fabricated in monomode photosensitive optical fiber by UV exposure through a phase mask," Appl. Phys. Lett. **62**, 1035–1037 (1993).

149. G. D. Marshall, R. J. Williams, N. Jovanovic, M. J. Steel, and M. J. Withford, "Point-by-point written fiber-Bragg gratings and their application in complex grating designs," Opt. Express **18**, 19844–19859 (2010).

150. G. D. Marshall, P. Dekker, M. Ams, J. A. Piper, and M. J. Withford, "Directly written monolithic waveguide laser incorporating a distributed feedback waveguide-Bragg grating," Opt. Lett. **33**, 956–958 (2008).

151. W. Yang, E. Bricchi, P. G. Kazansky, J. Bovatsek, and A. Y. Arai, "Self-assembled periodic sub-wavelength structures by femtosecond laser direct writing," Opt. Express **14**, 10117–10124 (2006).

152. A. Saliminia, R. Vallée, and S. L. Chin, "Waveguide writing in silica glass with femtosecond pulses from an optical parametric amplifier at 1.5µm," Opt. Commun. **256**, 422–427 (2005).

153. P. Dekker, M. Ams, G. D. Marshall, D. J. Little, and M. J. Withford, "Annealing dynamics of waveguide Bragg gratings: evidence of femtosecond laser induced colour centres," Opt. Express **18**, 3274–3283 (2010).

154. E. X. Pérez, "Design Fabrication and characterization of porous silicon multilayer optical devices," Universitat Rovira i Virgili (2007).

155. A. D. Rakić, "Algorithm for the determination of intrinsic optical constants of metal films: application to aluminum," Appl. Opt. **34**, 4755–4767 (1995).

156. "RefractiveIndex.INFO," https://refractiveindex.info/.

157. M. T. Aguilar-Gama, E. Ramírez-Morales, Z. Montiel-González, A. Mendoza-Galván, M. Sotelo-Lerma, P. K. Nair, and H. Hu, "Structure and refractive index of thin alumina films grown by atomic layer deposition," J. Mater. Sci. Mater. Electron. **26**, 5546–5552 (2015).

158. L. V. Rodríguez-de Marcos, J. I. Larruquert, J. A. Méndez, and J. A. Aznárez, "Self-consistent optical constants of $MgF_2$, $LaF_3$, and $CeF_3$ films," Opt. Mater. Express **7**, 989–1006 (2017).

159. L. Gao, F. Lemarchand, and M. Lequime, "Exploitation of multiple incidences spectrometric measurements for thin film reverse engineering," Opt. Express **20**, 15734–15751 (2012).

160. K. J. Vahala, "Optical microcavities," Nature **424**, 839–846 (2003).

161. S. M. Spillane, S. M. Spillane, T. J. Kippenberg, T. J. Kippenberg, K. J. Vahala, and K. J. Vahala,

"Ultralow-threshold Raman laser using a spherical dielectric microcavity," Nature **415**, 621–623 (2002).

162.   D. L. Huffaker, L. A. Graham, H. Deng, and D. G. Deppe, "Sub-40 µA continuous-wave lasing in an oxidized vertical-cavity surface-emitting laser with dielectric mirrors," IEEE Photonics Technol. Lett. **8**, 974–976 (1996).

163.   T. Grossmann, S. Klinkhammer, M. Hauser, D. Floess, T. Beck, C. Vannahme, T. Mappes, U. Lemmer, and H. Kalt, "Strongly confined, low-threshold laser modes in organic semiconductor microgoblets," Opt. Express **19**, 10009–10016 (2011).

164.   H.-B. Lin, J. D. Eversole, A. J. Campillo, and J. P. Barton, "Excitation localization principle for spherical microcavities," Opt. Lett. **23**, 1921–1923 (1998).

165.   I. Bica, "Formation of glass microspheres with rotating electrical arc," Mater. Sci. Eng. B **77**, 210–212 (2000).

166.   G. Nunzi Conti, A. Chiasera, L. Ghisa, S. Berneschi, M. Brenci, Y. Dumeige, S. Pelli, S. Sebastiani, P. Feron, M. Ferrari, and G. C. Righini, "Spectroscopic and lasing properties of $Er^{3+}$-doped glass microspheres," J. Non. Cryst. Solids **352**, 2360–2363 (2006).

167.   X. Peng, F. Song, S. Jiang, N. Peyghambarian, M. Kuwata-Gonokami, and L. Xu, "Fiber-taper-coupled L -band $Er^{3+}$-doped tellurite glass microsphere laser," Appl. Phys. Lett. **82**, 1497–1499 (2003).

168.   K. C. Fan, H. Y. Hsu, P. Y. Hung, and W. Wang, "Experimental study of fabricating a microball tip on an optical fibre," J. Opt. A Pure Appl. Opt. **8**, 782–787 (2006).

169.   H. Fujiwara and K. Sasaki, "Upconversion lasing of a thulium-ion-doped fluorozirconate glass microsphere," J. Appl. Phys. **86**, 2385–2388 (1999).

170.   J. Yu, E. Lewis, G. Farrell, and P. Wang, "Compound Glass Microsphere Resonator Devices," Micromachines **9**, 356 (2018).

171.   A. Heptonstall, M. A. Barton, A. Bell, G. Cagnoli, C. A. Cantley, D. R. M. M. Crooks, A. Cumming, A. Grant, G. D. Hammond, G. M. Harry, J. Hough, R. Jones, D. Kelley, R. Kumar, I. W. Martin, N. A. Robertson, S. Rowan, K. A. Strain, K. Tokmakov, and M. van Veggel, "Invited Article: $CO_2$ laser production of fused silica fibers for use in interferometric gravitational wave detector mirror suspensions," Rev. Sci. Instrum. **82**, 011301 (2011).

172.   G. Gouesbet and G. Grehan, *Optical Particle Sizing: Theory and Practice* (Springer Science & Business Media, 1988).

173.   N. Gaber, M. Malak, X. Yuan, K. N. Nguyen, P. Basset, E. Richalot, D. Angelescu, and T. Bourouina, "On the free-space Gaussian beam coupling to droplet optical resonators," Lab Chip **13**, 826–833 (2013).

174.   H. Wan, Z. Lu, J. Wang, Y. Zhou, and J. Wang, "A compact pulse-tunable fiber laser based on pulse-pumped high gain cavity," in *SPIE 9266, High-Power Lasers and Applications VII* (2014), p. 92660H.

175.   D. Eimerl, L. Davis, S. Velsko, E. K. Graham, and A. Zalkin, "Optical, mechanical, and thermal properties of barium borate," J. Appl. Phys. **62**, 1968–1983 (1987).